# Innovative Admixtures for Modifying Viscosity and Volume Change of Cement Composites

*Document status and date:*
Published: 22/12/2021

*Document Version:*
Publisher's PDF, also known as Version of Record (includes final page, issue and volume numbers)

*Please check the document version of this publication:*

• A submitted manuscript is the version of the article upon submission and before peer-review. There can be important differences between the submitted version and the official published version of record. People interested in the research are advised to contact the author for the final version of the publication, or visit the DOI to the publisher's website.
• The final author version and the galley proof are versions of the publication after peer review.
• The final published version features the final layout of the paper including the volume, issue and page numbers.

Link to publication

# Innovative Admixtures for Modifying Viscosity and Volume Change of Cement Composites

DESIGN, PERFORMANCE, AND APPLICATION

Hossein Karimi

# Innovative Admixtures for Modifying Viscosity and Volume Change of Cement Composites

**DESIGN, PERFORMANCE AND APPLICATION**

Hossein Karimi

# Innovative Admixtures for Modifying Viscosity and Volume Change of Cement Composites

### DESIGN, PERFORMANCE, AND APPLICATION

THESIS

ter verkrijging van de graad van doctor

aan de Technische Universiteit Eindhoven,

op gezag van de rector magnificus, prof.dr.ir. F.P.T. Baaijens,

voor een commissie aangewezen door het College voor Promoties,

in het openbaar te verdedigen op woensdag 22 december 2021 om 13:30 uur

door

**Hossein Karimi**

geboren te Teheran, Iran

Dit proefschrift is goedgekeurd door de promotoren en de samenstelling van de promotiecommissie is als volgt:

Voorzitter:       prof.dr.ir. T.A.M. Salet

1$^e$ promotor:    prof.dr.ir. H.J.H. Brouwers

2$^e$ promotor:    prof.dr. Q.L. Yu (Wuhan University)

Leden:           prof.dr. W. Chen (Wuhan University of Technology)

                   prof.dr. N. De Belie (University of Ghent)

                   prof.dr. H. Justnes (Norwegian University of Science and Technology)

                   prof.ir. S.N.M. Wijte

                   dr.ir. R. Cardinaels

*For my family*

*"In a large company, there aren't as many cars in the parking lot on Sunday at 3 p.m. as there are at a developer. It's the developers that bring the creative insight. It's the developers that bring the market knowledge. And it's the developers that bring that entrepreneurial energy."*

— Steve Jobs.

# Preface

It all started when I was four. I saw a physics professor on TV explaining elementary particles and I loved it, though I did not understand a word. I turned to my family and said I was going to obtain a PhD in Physics. I have always been an avid reader and after this decision spent most of my working and spare time dealing with mathematics, physics, and computer science. And now, here I am; Obtaining my PhD in Building Materials; Another mission in life completed!

First and foremost, I would like to thank my supervisor and promotor prof.dr.ir. H.J.H. Brouwers. You provided me with a prodigious opportunity to do my PhD in your research group and supported and motivated me immensely throughout my PhD. You inspired me a lot in both research and professionalism and provided me with all the essential prerequisites to take charge of my PhD independently and practically.

My gratitude also goes to my co-promotor dr. Q.L. Yu. Our scientific discussions about material science are some of my priceless memories that I will take with me in life. I learned a lot from you on this challenging journey as your supervision enhanced the quality of my research and publications.

My sincere appreciation also goes to Sappi Nederland Services Company for sponsoring part of my research, especially Dr. Lixian Xu, Dr. Math Jennekens, Dr. Linda Tufano, and Mr. Rick Claessen. My thanks also go to Mrs. Esther Stapper from Stapper Duurzaam Advies for sponsoring another part of my research. Thank you all for all our priceless meetings, discussions, and contributions on this challenging journey.

I am also grateful to the members of the promotion committee, Prof. dr. H. Justnes from Norwegian University of Science and Technology, Prof. dr. N. De Belie from University of Ghent, Prof. dr. W. Chen from Wuhan University of Technology, Prof. ir. S.N.M. Wijte and dr.ir. R. Cardinaels from the Eindhoven University of Technology for reading my work and providing precious recommendations for its improvement.

My thanks also go to Dr. Katrin Schollbach and Dr. Florent Gauvin for the work we have done together. I am also thankful to our lab technicians and supporting staff, especially Anneke Delsing, Harrie Smulders, Geert-Jan Maas, Wout van Bommel, and Jan Diepens. I wish to extend this note of gratitude to you, Mrs. Léontine Harmsen, for your gigantic contribution to making our office a lovely place to work.

My sincere appreciation also goes to all my colleagues in the Building Materials Research Group for their resourcefulness, trustworthiness and professionalism in the lab, in the office, in the sport center, in conferences, etc. The names, in alphabetical order, include, but are not limited to: Alberto, Anna, Alex, Azee, Bert, Bo, Charles, Chris, Daoru, Ewa, Fan, Felix, Jawad, Gang, Guillaume, Hamid, Helong, Iris, Jonathan, Kate, Katka, Kinga, Marina, Miruna, Parisa, Pei, Peipeng, Perry, Przemek, Qadeer, Rahim, Ricardo, Samuel, Shaohua, Sieger, Tao, Veronica, Winnie, Yuxuan, Yangyueye, Xiaoxiao, Xinglong, Xu, Xuan, Yan, Yuri, Yuxuan, Zahra, Zhengyao, Zixiao, and Zhihan.

Last but not least, I would like to express my sincerest appreciation to my parents (Shahin and Hassan). There is no way for me to express my utmost gratitude and thanks to you two. Through the good times and the bad, you have always been there for me. My thanks are also given to my siblings (Sheida, Shiva, Danial, Shima, and Hesam). I am beyond lucky to have been gifted you and I am so grateful for our bond. Thank you for being such a big part of my life.

<div align="right">

Hossein Karimi

Eindhoven, November 2021

</div>

# Summary

Inferior viscosity and volume change deteriorate concrete and reduce durability. This dissertation aims to tackle these shortcomings by implementing two sustainable strategies. The first strategy is using a mix design method to enhance pumpability and reduce shrinkage. The second strategy is to develop concrete admixtures. Where possible, the link between the first and second strategy is made, and a hybrid strategy comprising an optimum mix design method and a concrete admixture is introduced.

The first strategy is discussed in Chapter two. It investigates the relationship between the modified A&A concrete mix design model and the pumpability and shrinkage of flowing concrete. The outcome of this modified model is compared to ACI 211.9R-18 recommendations and the technical literature. It is established that there is a good correlation between the distribution modulus of the modified A&A model and the pumpability and drying shrinkage of concrete. A smaller than 0.35 distribution modulus results in ideal-for-pumping mixtures. A high distribution modulus results in a high coarse-to-fine aggregate ratio and diminishes the drying shrinkage of concrete.

The second strategy is discussed in chapters three to six. Chapter three starts with reporting the characteristics of the rapidly expansive light-burnt magnesia. The composition, crystal structure, morphology, surface area, pore structure, and the expansive properties of rapidly expansive magnesia are investigated. It is confirmed that the key to producing shrinkage compensating magnesia is controlling and minimizing sintering during calcination. The modified A&A model from Chapter two is used for optimizing concrete mixtures in this chapter.

Chapter four employs surface properties to introduce an accelerated technique for assessing the homogeneity and thermal history of light-burnt magnesia, the subject of the previous chapter. This technique uses the weighted mesopore probability distribution of light-burnt magnesia to identify and quantify homogeneity. The former is determined from the number of peaks present in the distribution and the latter from the location of each peak. These

findings help to prevent unpredicted expansion in concrete incorporating light-burnt magnesia.

Chapter five evaluates the performance of paper pulp as an innovative viscosity modifying admixture for cement composites. The influence of fineness on paper pulp's viscosity modification, hydration kinetics, autogenous shrinkage, and compressive strength is reported. It is shown that the hierarchical structure of paper pulp makes it possible to activate bridging flocculation and swelling mechanisms of paper pulp fibers at different levels to obtain versatile viscosity modifying admixtures.

Chapter six introduces a fresh mindset towards waste baby diapers. In this setting, shredded waste baby diapers are used to modify the viscosity of concrete. A proposed model computes the average concentration of chemicals in combined mixing water of cement composites after adding shredded waste diapers. The model is combined with the relevant standards to present a legal framework about the applicability of waste diapers in different types of concrete. The modified A&A model from Chapter two is used for optimizing concrete mixtures in this chapter.

# Table of contents

# Introduction

## 1.1    Background and motivation

Concrete is mainly held together by a nanostructured material called calcium-silicate-hydrate (C-S-H) [1,2]. Despite the very high strength of C-S-H, inferior rheological behavior and volume change characteristics may damage conventional concrete easily [3,4].

One way to toughen concrete is to design with an optimized particle packing model. Several particle packing models have been introduced to maximize the granular skeleton's packing and design conventional vibrated concrete mixtures [5–7]. Although these proportioning methods give satisfactory results for designing conventional vibrated mixtures with low to medium slump, they do not necessarily result in highly workable cohesive flowing concrete mixtures. The lack of a mix design method that optimizes pumpability, enhances rheological behavior, and reduces shrinkage has existed as a construction industry problem for many years. One motivation of this thesis, therefore, is to introduce a mix design method for pumpable flowing concrete with low volume change.

Another way to toughen concrete is to incorporate admixtures. Extensive multi-phase studies have been carried out on shrinkage reducing admixtures (SRA) such as monoalcohols [8,9], glycols [9–12], polyoxyalkylene glycol alkyl ethers [13], or other non-ionic surfactant structures [14] to control capillary pressure within pores and decrease the volume change in concrete. Shrinkage compensating admixtures (SCA) of K, M, S, and G type [15] and light-burnt magnesium oxide [15] are other categories of materials that have been introduced to produce initial expansion to offset strains caused by shrinkage in concrete. Permeability reducing admixtures (PRA) [16,17] and superabsorbent polymers [18,19] have also shown promising results in terms of volume control and crack mitigation in concrete. There have also been studies on the effect of a combination of two or more types of chemical

admixtures to make crack-free concrete, too [20]. However, along with the growth in the demand for admixtures, there are increasing concerns about their circularity. Since the circular economy is the key to sustainable development, another motivation of this thesis is to introduce sustainable routes to develop concrete admixtures.

*Mixture design method for pumpable low shrinkage flowing concrete*

Flowing concrete is a mixture that retains its cohesiveness at a slump greater than 190 mm [21,22]. It has significant advantages over self-consolidating concrete. Contrary to self-consolidating concrete, flowing concrete does not require reducing the maximum size of the aggregates or modifying the proportion of fine aggregates in the mixture. In addition, as the yield stress and viscosity of flowing concrete are not as low as those of self-consolidating concrete, there is no need to add viscosity modifying admixtures or fines to enhance the viscosity while retaining low yield stress in flowing concrete mixtures. As a result, compared to self-consolidating concrete, flowing concrete is less costly, has less shrinkage, and has less cracking susceptibility. Flowing concrete provides significant benefits over conventional vibrated concrete, too. It is proportioned with normal aggregate sizes, but at the same time, it can flow into highly congested areas. It is significantly more flowable than conventional vibrated concrete and requires far less vibration to consolidate. As a result, compared to conventional vibrated concrete, flowing concrete increases production rates, reduces noise nuisance, lowers labor costs, and increases mold lifetime.

Three major obstacles have hampered this technology from wide adoption. Firstly, compared to conventional vibrated concrete and self-consolidating concrete, the mix-design method and particle-size distribution of flowing concrete remain largely understudied. Secondly, the limited research on flowing concrete is based on maximum density and does not consider the influence of the physics of particles on shrinkage. Thirdly, the limited researches on flowing concrete do not provide information on the pumpability of the mix design method. Providing solutions for these technical obstacles is of paramount importance.

*Rapidly expansive light-burnt magnesia to modify volume change*

Magnesia is rare in nature and is usually produced by the calcination of magnesite. The expansive properties of magnesia are a function of calcination temperature, residence time, particle size, and impurities in the parent solid [23,24]. Research on the application of magnesia in concrete has been mostly restricted to slow-hydrating magnesia for compensating cooling shrinkage of concrete. The acid reactivity of cooling shrinkage

magnesia is typically more than 50 seconds [25], and it needs water curing or thermal curing for activation [26,27].

Rapidly expansive light-burnt magnesia reacts rapidly with water to form an expansive hydration product (brucite) and can be utilized as an SCA in concrete. One of the advantages of magnesia to ettringite-based or calcium hydroxide-based SCAs is the high stability of brucite [28,29]. Unlike magnesia, the hydration product of ettringite-based SCAs is unstable at high temperatures. The hydration product of calcium oxide-based SCAs is unstable in corrosive environments, too. Magnesia requires less water for curing than the ettringite-based SCAs, and its expansion can be adjusted during production. Surprisingly, the impact of rapidly expansive magnesia on shrinkage compensation of concrete is seldom studied, and it is unclear to what extent it can perform as an SCA.

*Homogeneity and thermal history of light-burnt magnesia by surface properties*

Light-burnt magnesia (LBM) is usually produced by calcining magnesite at temperatures lower than 1000 °C. It accounts for one-third of magnesia applications and has high chemical activity. LBM has two major applications in the construction industry. Firstly, it is used as an expansive agent to compensate shrinkage of concrete. Carefully calcined LBM acts as an expansive agent and produces expansion at a rate closely matching the long-term shrinkage of concrete to prevent concrete cracking [16]. Secondly, LBM is used as a primary ingredient to produce Sorel cement. It is now well established that variation in the thermal history of LBM significantly affects the properties of the final application products [30].

Much of the current literature on LBM pays particular attention to the assessment of the average reactivity of LBM. Mo et al. [23] studied the calcination of magnesium oxides and reported the change in porosity and crystal structure of magnesia due to calcination temperature. Harper used iodine number to index reactivity as used by the American magnesia industry [31]. Alegret et al. [32] proposed potentiometry to study the reactivity of magnesia. Hirota et al. [33] characterized sintering of magnesia by crystallite size, particle size, and morphology. Kim et al. [34] studied the transformation of the crystal structure of $MgCO_3$ and $Mg(OH)_2$ to MgO during calcination. Zhu et al. [35] proposed a corrected MgO hydration convention method for reactivity assessment. Chau et al. [36] introduced an accelerated reactivity assessment method based on the time required for acid neutralization of magnesia. Surprisingly, none of the current LBM reactivity analysis methods can provide information on its thermal history.

*Milled paper pulp to modify rheological behavior*

Paper pulp is attracting widespread interest in different fields thanks to its high volume, environmental-friendly origin, and potential economic profits. It has helped the paper industry to maintain its high rank among recycling industries as a combination of recycled and virgin pulp leads to suitable paper quality [37]. Nonetheless, digitization has caused less demand for paper pulp, especially in Europe and North America [38]. This reduction has initiated endeavors to transform the paper industry and find other ways to valorize paper pulp. So far, the valorization methods have been limited to applications such as manufacturing fibrous insulation in buildings [39], producing bitumen thickener in asphalt [39], or producing energy by incineration [39,40].

One way to valorize wood-based pulp is to incorporate it as a reinforcing agent in cement composites. For example, there has been extensive research on applying bamboo pulp [41–44], kraft pulp [45–50], cellulose pulp [51,52], pine and eucalyptus pulp [53–55], pinus pulp [56], sisal pulp [57,58], and waste pulp  [59] in cement composites as a reinforcement. Another way to valorize wood-based pulp is to utilize it as an internal curing agent for cement composites [60,61]. Pulp dosages of up to 15% weight of cementitious materials have been reported for both applications. However, little attention has been paid to the hierarchical and hydrophilic characteristics of the wood-based pulp as a route to make highly effective concrete additives.

*Waste baby diapers to modify rheological behavior*

Baby diapers accounted for more than 74% of the US$ 7.1 billion global superabsorbent polymers (SAPs) market, with a production rate of 2.119 million tons in 2014 [62]. Currently, waste baby diapers account for 2% to 7% of municipal solid waste [63]. Despite their high volume and excellent water absorption, waste baby diapers have been mostly landfilled [63] or incinerated [64]. In Europe, 68% of waste baby diapers are landfilled and 32% incinerated, while for the USA, the numbers are 80% and 20%, respectively [65]. Landfilling causes serious environmental problems such as methane emissions, water pollution, land use, and odor [66,67]. Furthermore, some studies have shown that the biodegradation of baby diapers in landfills is unlikely to happen due to low biological activity in landfills and consumers' tendency to throw waste baby diapers away by wrapping them in plastic [68,69]. Therefore, there is an urgent need to introduce new measures to deal with waste baby diapers.

## 1.2    Scope and objectives

The central question in this dissertation is how to design admixtures with an eye on sustainability and circularity, to tackle shortcomings of cement composites in terms of **rheological behavior** and **volume change**. In particular, this dissertation will examine five main research questions in five separate chapters:

**Mixture design method for pumpable low shrinkage flowing concrete (Chapter 2)**

How does the modified A&A model relate to the pumpability and shrinkage of concrete? How effective is this model in producing **pumpable low shrinkage flowing concrete**?

**Rapidly expansive light-burnt magnesia to modify volume change (Chapter 3)**

How effective is the rapidly expansive **light-burnt magnesia** with less than 10 s acid reactivity in compensating **concrete shrinkage**? What effect does the rapidly expansive light-burnt magnesia have on the shrinkage of concrete designed using the **model discussed in the chapter two**?

**Homogeneity and thermal history of light-burnt magnesia (Chapter 4)**

How effective is the deconvolution of pore size computation by the non-local density functional theory in accelerated assessment of the **homogeneity and thermal history** of light-burnt magnesia, the **subject of the previous chapter**?

**Milled paper pulp to modify rheological behavior (Chapter 5)**

How effective is the milled paper pulp in **modification of viscosity**, hydration kinetics, **shrinkage**, and compressive strength of cement composites?

**Waste baby diapers to modify rheological behavior (Chapter 6)**

How effective are the shredded waste diapers in **viscosity modification** of self-consolidating concrete, designed using the **model discussed in the chapter two**?

## 1.3    Outline of the thesis
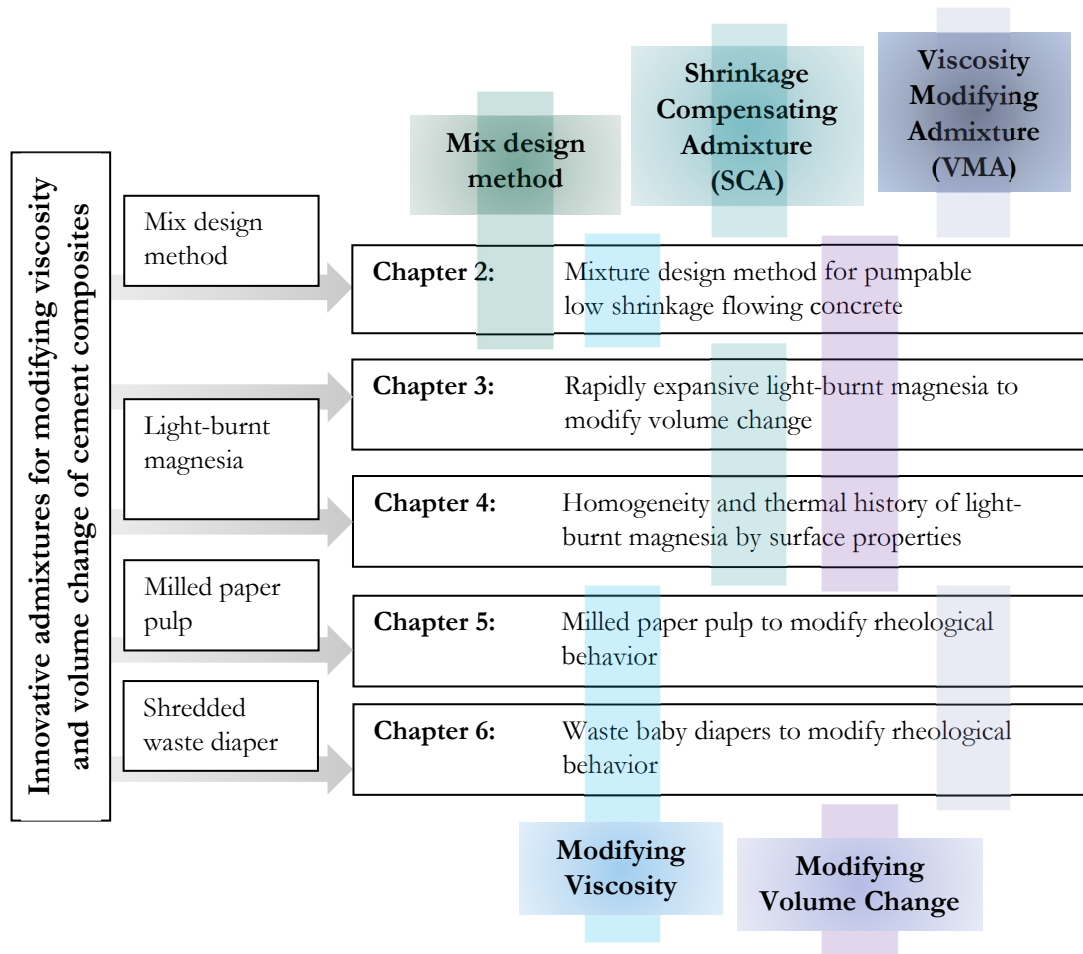


**Figure 1.1:** Brief outline of this dissertation.

The outline of this dissertation, illustrated in Fig. 1.1, can be listed as follows. In **Chapter 2**, the relationship between the modified A&A concrete mix design model and the pumpability and shrinkage of flowing concrete are investigated. The particle packing of the model is compared to ACI 211.9R-18 recommendations and the technical literature. In **Chapter 3**, rapidly expansive magnesia is discussed and its performance to compensate shrinkage of the concrete mixtures is analyzed. The concretes of this chapter are designed by the modified A&A model, discussed in Chapter 2. In **Chapter 4**, surface properties is employed to analyze the changes in the surface of light-burnt magnesia (discussed in Chapter 3) at various temperatures. A model is also introduced to quantify these changes. In **Chapter 5**, the performance of a viscosity modifying admixture based on milled paper pulp is reported. The flow characteristics and shrinkage of cement composites containing milled paper pulp are modeled. In **Chapter 6**, a fresh mindset toward waste baby diapers is presented and they were used as a viscosity modifying admixture in concrete. The concretes of this chapter are

designed by the modified A&A model, discussed in Chapter 2. A model is also introduced to compute the average concentration of chemicals in combined mixing water of a cement composite in the wake of incorporating shredded waste diapers. In **Chapter 7**, the main conclusions from this dissertation and recommendations for future research work are provided.

# Mixture design method for pumpable low shrinkage flowing concrete

*Flowing concrete has substantial advantages over conventional vibrated concrete and self-consolidating concrete. But the widespread adoption of this technology has been hampered by the lack of a well-grounded mix design method. In this chapter, the applicability of the modified A&A model for designing pumpable concretes according to ACI 211.9R-18 is analyzed. An experimental investigation is undertaken to evaluate consistency, compressive strength, and shrinkage of flowing concretes designed with this method. The results show that the modified A&A model can be used to optimize the particle size distribution of concrete to produce pumpable concretes according to the ACI 211.9R-18 [70]. At a distribution modulus of 0.35, the model serves as the recommended boundary limit for ideal-for-pumping mixture design. The distribution modulus of the model controls the combined grading, the ratio of coarse-to-fine aggregates, and the percentage of fine aggregates passing 300 µm and 150 µm. A high distribution modulus results in a high coarse-to-fine aggregate ratio and lowers the drying shrinkage of concrete.*

## 2.1 Introduction

Concrete is the most widely used material worldwide for several primary reasons: (1) outstanding resistance to water and fire, (2) low production and maintenance cost, and (3) the ease with which it can be shaped while casting [71]. Three major concrete types used in the construction industry are conventional vibrated concrete (CVC), flowing concrete (FC), and self-consolidating concrete (SCC) [3]. The main difference between these concrete types is flowability [72]. CVC typically has less than 100 mm slump and high yield stress [73]. As a result, it demands high rapid vibratory impulses to become liquified and consolidated [74]. On the other hand, SCC has very high flowability with almost no yield stress in a way that it only demands the action of gravity to consolidate [75]. Although SCC offers significant

benefits over CVC in terms of labor cost, noise nuisance, and formwork wear and tear, it is more costly [76,77]. Furthermore, SCC requires a superplasticizer, finer aggregate grading, and incorporating fine materials (powders) [78] into the mixture. Some SCC mixtures also require viscosity modifying admixtures (VMAs), although the use of a VMA is not always essential [79,80] and sometimes may cause conflicts with the superplasticizer [81]. These requirements raise the cost and increase concrete shrinkage and cracking susceptibility, making SCC less desirable for applications where low shrinkage is the primary concern (e.g., industrial concrete floors) [82]. These shortcomings have generated considerable interest in another type of concrete, namely flowing concrete (FC).

According to ASTM and ACI, FC is a concrete mixture that retains its cohesiveness at a slump greater than 190 mm [21,22]. European standards use the flow table test [83] for classifying concrete into six classes: F1 to F6 [84]. Though the flow table test [83] of the European standards is different than the slump test of the ASTM [21,22], one might classify FC as a concrete in the range of F3 to F6 [84]. Contrary to SCC, FC does not require reducing the maximum size of the aggregates or modifying the proportion of fine aggregates in the mixture. In addition, as the yield stress and viscosity of FC are not as low as that of SCC, there is no need to add VMAs or fines to improve viscosity while retaining low yield stress in FC mixtures. As a result, FC is less costly compared to SCC, has less shrinkage, and has less cracking susceptibility. FC provides significant benefits over CVC, too. It is proportioned with normal aggregate sizes, but at the same time, it can flow into highly congested areas. It is significantly more flowable than CVC and requires far less vibration to consolidate. As a result, compared to CVC, FC increases production rates, reduces noise nuisance, lowers labor cost, and increases mold lifetime.

There are, however, three major obstacles related to the design and use of FC. Firstly, in comparison to CVC and SCC, the mix-design method and particle-size distribution of FC remain largely understudied. The particle size distribution (PSD) highly affects the rheological and mechanical properties of concrete [85,86]. The PSD determines the particles' void content and the paste's volume needed to fill the voids [87]. In addition, the PSD determines the specific surface area of the particles and the volume of the paste required to coat the aggregates. Several particle packing models have been introduced to maximize the density of the granular skeleton and to design CVC mixtures [5–7]. Although these proportioning methods give satisfactory results for designing low to medium slump CVC mixtures, they cannot create highly workable cohesive FC mixtures without modifications. This shortcoming is mainly due to the fact that the main design criteria in proportioning

CVC and FC mixtures are different: CVC mixtures are designed for high density and low paste volume, while FC mixtures are designed for high flowability and cohesiveness. Note that the high packing density of FC reduces shrinkage thanks to a lower paste volume, too. Surprisingly, a reliable FC mix design method that aims at both high packing density and flowability of concrete remains unreported.

Secondly, the limited research on FC is based on maximum density and does not consider the influence of the physics of the particles on the mixture's flowability. Hendrix and Trejo presented an FC mixture proportioning method based on the paste to aggregate volume ratio [88]. Su and Miao proposed a mix design method for FC mixtures based on packing factor, which is the ratio of the mass of aggregates in the mix to that of a loosely packed state [89]. They suggested that the aggregate packing factor determines the aggregate content and affects the workability of concrete [89]. To date, the research on FC mixture design methods has tended to focus on particle packing rather than flowability. A much more systematic approach that identifies how particle packing interacts with the mixture's flowability remains unreported.

Thirdly, the limited researches on FC do not provide information on the pumpability or shrinkage of the mix design method. In many critical applications, low shrinkage concrete needs to be pumped off. Much of the current literature on the pumpability of concrete pays particular attention to the formation of the lubrication layer and its effect on the pumpability of concrete [90,91]. One of the very few guides to select mixture proportions that lead to the most efficient concrete pumping results is ACI 211.9R-18 [70]. This guide provides numerical guidelines on optimum aggregate grading and fine content that lead to the most efficient pumping results. At the current state-of-the-art, one common way to design a pumpable concrete mixture is to design the concrete mix and then compare the mix-design to ACI 211.9R-18 [70]. It would be more convenient to have a mix design method with ACI 211.9R-18 guidelines [70] at its heart. However, such a method remains unreported.

This chapter aims to provide solutions to these obstacles. First, the main results from the literature regarding the maximum particle packing and flowability of the modified A&A model are presented. Next, the model is adapted to the specific case of concrete and compared and contrasted with the technical recommendations from the American Concrete Institute on pumpability. It is shown that the modified A&A model is highly compatible with the ACI's experimental data. At the distribution modulus of 0.35, this model gives the boundary limit for ideal pumpability. Moreover, the pumpability and application of the

modified A&A model at lower distribution moduli such as $q = 0.3$ and $q = 0.25$ are reported. In the third part, the modified A&A model is used to design FC mixtures. The fresh and hardened properties of the FC mixtures, such as flow diameter, compressive strength, and drying shrinkage are reported. The present research establishes that the modified A&A model is highly compatible with ACI's experimental data on pumpability. Furthermore, using this model for designing the whole concrete mixture (aggregates and powders) at a suitable distribution modulus leads to flowing concrete with low shrinkage.

## 2.2 Modified A&A model

One approach to achieving the maximum particle packing in concrete mixtures is using the modified A&A model as expressed by [87,92]

$$P(d) = \frac{d^q - d^q_{min}}{d^q_{max} - d^q_{min}} \tag{2.1}$$

where $d$ is the particle size, $d_{min}$ the minimum particle size, $d_{max}$ the maximum particle size and $P(d)$ the cumulative fraction of the total solids being smaller than size $d$.

Equation (2.1) has already been used to improve particle packing of cement composites through three approaches. The first approach was pioneered by Brouwers and Radix and used the modified A&A model to design the whole concrete mixture [79,80]. In this approach, all concrete mixture ingredients (i.e., coarse aggregate, fine aggregate, and powders) are proportioned by solving a curve-fitting problem that minimizes the difference between the A&A model and the target function. Several studies have used this approach for proportioning self-consolidating concrete (SCC), ultra-high-performance concrete (UHPC), and earth-moist concrete [79,80,87,92–94]. The second approach uses the modified A&A model to optimize the particle packing of fine aggregates. Several studies have used this approach for proportioning UHPC, earth-moist concrete, roller compacted concrete (RCC) and SCC [95–97]. The third approach uses the modified A&A model to optimize the PSD of the binder system. Several studies have shown that binary and ternary binder systems with A&A distribution had lower water demand and higher packing density [98,99].

Although the modified A&A model provides a dense and optimized packing of all granular ingredients, previous studies have not dealt with the best of these three approaches for designing mixtures. In addition, in reviewing the literature, no data was found on the

association between the highest packing density and the pumpability of the mixture. FC mixtures are required to have high packing density and, at the same time, be cohesive and workable to flow easily into congested areas. The next section compares and contrasts the particle packing of the modified A&A model with the ACI's empirical data.

## 2.3    Verification and validation with the scientific literature

As was pointed out in the previous section, this section compares and contrasts the optimum particle size distribution of the modified A&A model with the technical recommendations on the pumpability of concrete by the American Concrete Institute (i.e., ACI 211.9R-18). The maximum size of coarse aggregates for making FC mixtures was 31.5 mm, and the minimum size of the powder (e.g., cement) was 0.275 μm. In this chapter, the term 'recommended boundary limit' refers to the recommended combined grading for evaluating the pumpability of concrete by ACI 211.9R-18. According to ACI [70], a combined aggregate grading above the recommended boundary limit is ideal for pumping. In this chapter, the term 'computed grading' refers to the computed particle size distribution of the modified A&A model at a specific distribution modulus ($q$). A considerable amount of literature has been published on the modified A&A model [79,80,100–102,92–99]. These studies have used the model at a distribution modulus of 0.35 to 0.2. The paragraphs that follow will compare and contrast these distribution moduli with the ACI's recommendations on pumpability.

Hüsken and Brouwers [93] used the distribution modulus of 0.35 to design zero slump concrete. They utilized the modified A&A model to optimize the whole mixture (aggregates and powder), enhance the mixtures' compressive strength, and improve the cement efficiency of zero slump concrete. Khayat and Libre [96] employed the modified A&A model at the distribution modulus of 0.35 to design roller-compacted concrete. They used the model only to optimize aggregates in their mixture.

Fig. 2.1 highlights the difference between the computed grading at $q = 0.35$ and the recommended boundary limit and is quite revealing in several ways. Firstly, the most crucial aspect of the computed grading is that it is identical to the recommended boundary limit for particles smaller than 2.36 mm. Secondly, it is above the recommended boundary limit for particles larger than 2.36 mm. Taken together, the computed grading at $q = 0.35$ is regarded as ideal for pumping by ACI. That is to say, using the modified A&A model to design the whole concrete mixture (i.e., the first approach in Section 2.2) results in an ideal-for-pumping mixture, according to ACI. In contrast, the mix designs where the model is used

only to optimize fine aggregates or the binder system (i.e., the second and third approaches in Section 2.2) do not necessarily lead to ideal-for-pumping mixtures, according to ACI.
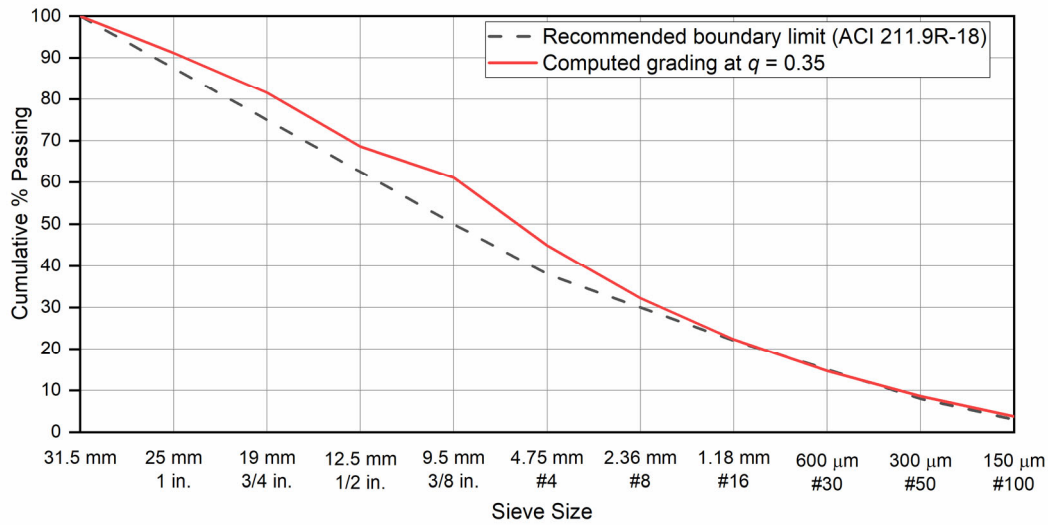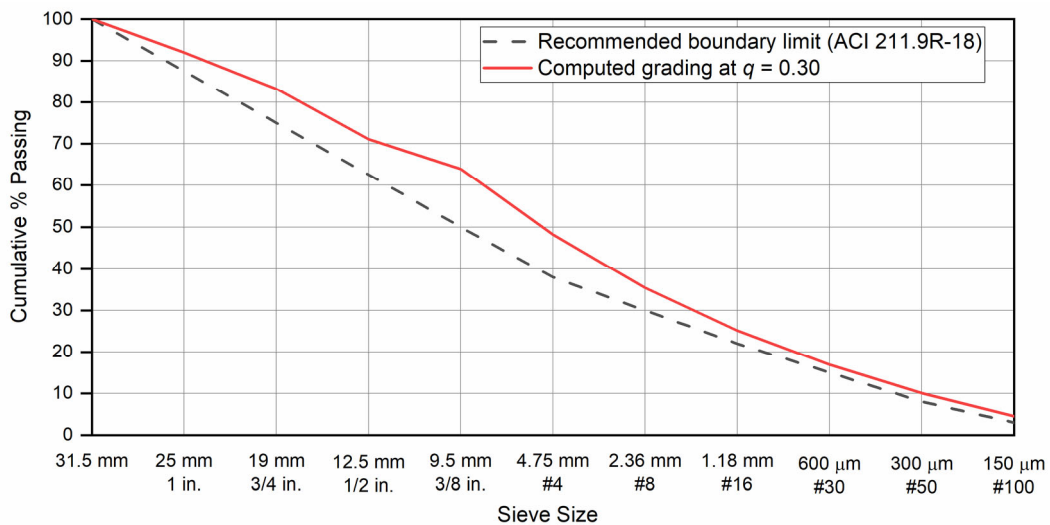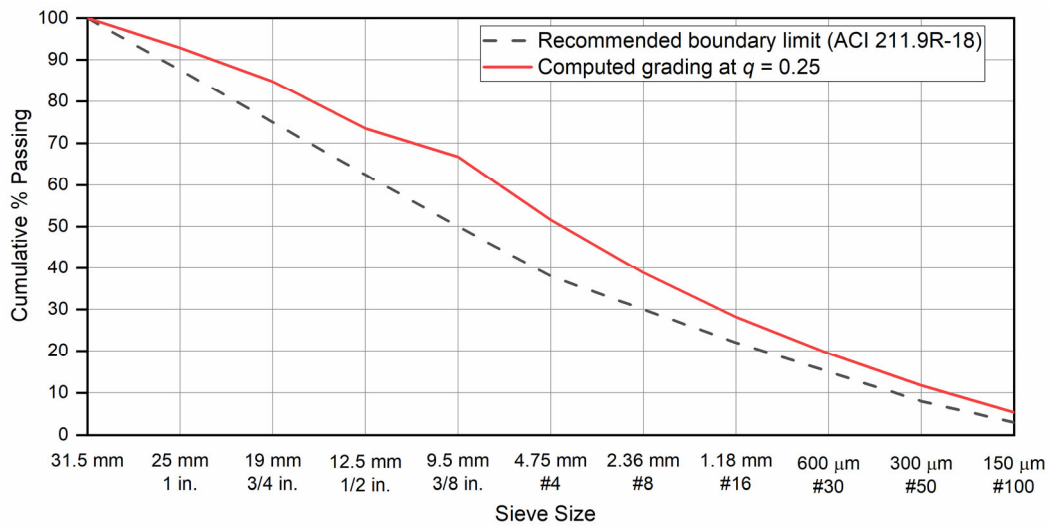


**Figure 2.1:** Computed combined grading of modified A&A model at the distribution modulus of 0.35 (represented by the solid red line) and the recommended combined grading for evaluating pumpability of concrete by ACI 211.9R-18 (represented by the dashed black line).

Hunger used the modified A&A model to design the whole mixture of self-consolidating concrete [92]. Khayat and Mehdipour [95] employed the modified A&A model at a distribution modulus of 0.29 to design self-consolidating concrete. They utilized the model only to optimize aggregates in their mixture. Their findings showed that a distribution modulus of 0.29 fits reasonably well to the ideal PSD of aggregates for proportioning SCC with low binder content. Wang et al. [101] used the modified A&A model at the distribution modulus of 0.29 to design SCC. Their approach was different from Khayat and Mehdipour [95] as they used the modified A&A model to optimize the whole mixture (aggregates and powder). Their results showed that this approach could reduce up to 20% binder content compared to existing SCC mix proportioning methods.

Fig. 2.2 highlights the difference between the computed grading at $q = 0.3$ and the recommended boundary limit. Compared with Fig. 2.1, all fractions of the computed grading are above the recommended boundary limit. That is to say, the distribution modulus of 0.30 is considered ideal for pumping. Based on ACI, using the modified A&A model to design the whole concrete mixture (i.e., the first approach in Section 2.2) at a distribution modulus of 0.3 results in an ideal-for-pumping mixture, too.

The better pumpability at the distribution modulus of 0.3 than a higher distribution modulus (e.g., $q = 0.35$) is partly associated with a lower coarse-to-fine aggregate ratio. ACI 211.9R-18 [70] states that the coarse-to-fine aggregate ratio may be modified to improve pumpability but does not state to which degree. This shortcoming exacerbates when a few sources are available for coarse and fine aggregates and powders. In such situations, it is not apparent the final coarse-to-fine aggregate ratio should be supplied from which source. In contrast to the ACI 211.9R-18 [70], in the modified A&A model, the source of the final coarse to fine aggregate ratio can be chosen by solving a curve-fitting problem that minimizes the difference between the A&A model and the target function [87].



**Figure 2.2:** Computed combined grading of modified A&A model at the distribution modulus of 0.30 (represented by the solid red line) and the recommended combined grading for evaluating pumpability of concrete by ACI 211.9R-18 (represented by the dashed black line).

Mueller et al. [100] used the modified A&A model at a distribution modulus of 0.27 to design SCC. They used the model to optimize the whole mixture (aggregates and powder) and showed that the modified A&A model best describes the PSD of a stable low-powder SCC. Yu et al. [103] developed a cement-based lightweight composite using the modified A&A model at a distribution modulus of 0.25. They used the model to optimize the whole mixture (aggregates and powder) and obtained minor porosity thanks to a more delicate structure, rich in inert fines.

Fig. 2.3 highlights the difference between the computed grading at $q = 0.25$ and the recommended boundary limit. Compared with Fig. 2.1 and Fig. 2.2, all fractions of this

computed grading are further above the recommended boundary limit. That is to say, the distribution modulus of 0.25 provides a finer particle packing and is ideal for pumping.

Distribution moduli smaller than 0.25 have already been used to develop special concrete mixtures. Yu et al. [102] developed ultra-high performance fiber reinforced concrete at a distribution modulus of 0.23. They used the model to optimize the whole mix (aggregates and powder) and reached the maximum compressive strength of about 150 MPa at 28 days. Note that small distribution moduli result in fine mixtures with a low coarse-to-fine ratio. Such mixtures are rich in powders and have higher water demand and shrinkage susceptibility. As a result, they are not suitable for proportioning FC mixtures, although they lead to desirable ultra-high-performance mixtures.



**Figure 2.3:** Computed combined grading of modified A&A model at the distribution modulus of 0.25 (represented by the solid red line) and the recommended combined grading for evaluating pumpability of concrete by ACI 211.9R-18 (represented by the dashed black line).

Based on ACI 211.9R-18 [70], experience has shown that for optimum pumpability, 15 to 30 percent of fine aggregates should be smaller than 300 μm (No. 50 screen), and 5 to 10 percent should be smaller than 150 μm (No. 100 screen). This recommendation needs further clarification. Although the smaller particles lubricate the larger ones, a massive difference exists between a mixture containing 30 percent fine aggregates smaller than 300 μm and one containing only 15 percent. ACI 211.9R-18 [70] also advises blending fine aggregate deficient in either of these two sizes with fine sand, which needs further clarification, too. Adding another sand will not only modify the percentage of fine aggregates smaller than 300 μm but also change the percentage of fine aggregates larger than 300 μm.

What remains unclear in ACI recommendations is how and to what degree these modifications need to be implemented. By contrast, the most prominent finding to emerge from the modified A&A model is the percentage of fine aggregates smaller than 300 μm and how each blended fine aggregate contributes to removing the finer than 300 μm particle deficiency. This point is discussed in more detail below.

Fig. 2.4 compares the ACI's recommended percentage of fine aggregates passing 300 μm (No. 50 screen) [70] with the computed fine aggregates at $q = 0.35$ to $q = 0.20$. What stands out in this figure is the high degree to which the modified A&A model is compatible with the ACI's recommendations. The computed fine aggregates passing 300 μm is about 20 percent at $q = 0.35$ and increases to 25 percent at $q = 0.20$. That is to say, the modified A&A model has a theoretical background which enables it to compute fines at different distribution moduli for various applications. This strength becomes more significant in the recommended percentage of fine aggregates passing 150 μm (No. 100 screen).

Fig. 2.5 compares the ACI's recommended percentage of fine aggregate passing 150 μm (No. 100 screen) [70] with the computed fine aggregate at $q = 0.35$ to $q = 0.20$. The fine aggregate percentage is just above 8 percent at $q = 0.35$ and rises to 11.5 percent at $q = 0.20$. As discussed earlier, a distribution modulus larger than 0.27 is used for proportioning normal concrete, self-consolidating concrete, and roller-compacted concrete. On the other hand, a distribution modulus smaller than 0.27 is used for proportioning special concretes with very fine grading, such as ultra-high-performance concrete.

The findings of this section provided a deeper insight into the pumpability of the modified A&A model. When this model is used to design the whole mixture (aggregates and powders), it is highly compatible with the technical recommendations on the pumpability of concrete by the American Concrete Institute (i.e., ACI 211.9R-18). The modified A&A model at a distribution modulus of 0.35 is the boundary limit for ideal pumpability. A distribution modulus smaller than 0.35 is considered ideal for pumping. The choice of distribution modulus depends on the application for which the concrete mixture is designed. The theoretical background of the modified A&A model makes it possible to optimize pumpability for various applications.
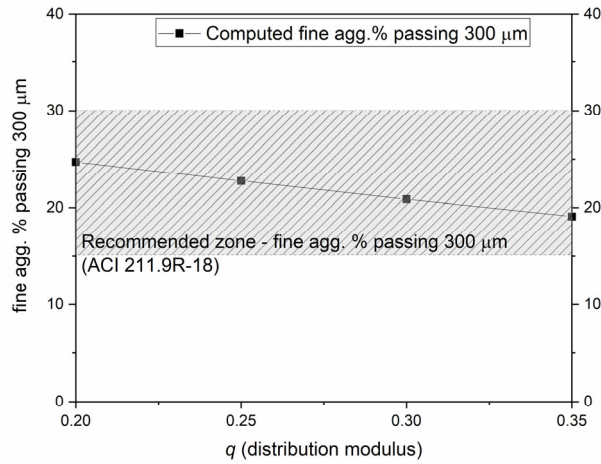
**Figure 2.4:** Recommended percentage of fine aggregate passing 300 μm (No. 50 screen) (represented by the cross-hatched area) and the computed fine aggregate of the modified A&A model at distribution moduli of 0.20 to 0.35.
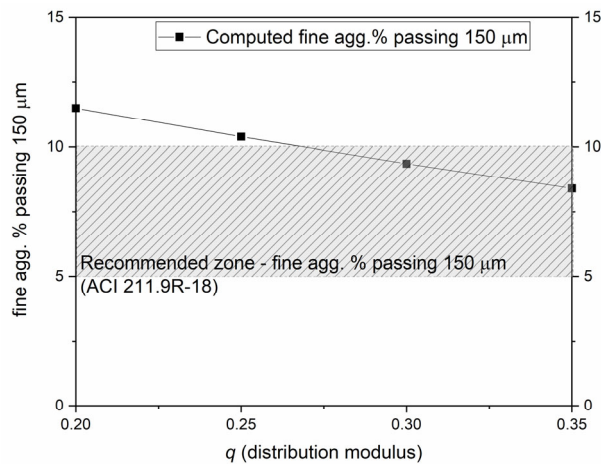


**Figure 2.5:** Recommended percentage of fine aggregate passing 150 μm (No. 100 screen) (represented by the cross-hatched area) and the computed fine aggregate of the modified A&A model at distribution moduli of 0.20 to 0.35.

## 2.4    Verification and validation with experimental results

### 2.4.1    Materials and methods

The current investigation involved the production and analysis of flowing concrete. The cements CEM I 52.5 R and CEM III 42.5 LH/SR provided by ENCI (the Netherlands) [104,105] were utilized to produce concretes. The CEM I 52.5 R was fine Portland cement (Blaine of ca. 527 m²/kg [104]), and the CEM III/B 42.5 LH/SR was a fine binary blend of

slag and Portland clinker (Blaine of ca. 488 m$^2$/kg [105]). The chemical composition of both cement types was determined by X-ray fluorescence (XRF) and is shown in Table 2.1.

**Table 2.1:** Chemical composition of CEM I 52.5 R and CEM III 42.5 LH/SR, measured by XRF (in weight percent).

| Mineral compound | MgO | $Al_2O_3$ | $SiO_2$ | $SO_3$ | CaO | $Fe_2O_3$ | LOI |
|---|---|---|---|---|---|---|---|
| CEM I | 1.6 | 6.2 | 17.7 | 3.0 | 64.7 | 3.5 | 2.5 |
| CEM III | 4.6 | 9.5 | 28.2 | 5.1 | 49.8 | 1.3 | 0.3 |

River gravel with the maximum size of aggregate (MSA) of 31.5 mm and river sand were used to produce concrete. A polycarboxylic ether-based superplasticizer (SP) with a solid content of 12% was used to adjust the flow properties of flowing concretes. The dosage of the SP refers to the weight of the solution in water as a percentage of the weight of cement. The water in the superplasticizer solution was deducted from the mixing water. The powders' particle size distribution (PSD) was measured employing a Malvern Mastersizer 2000, and sieve analysis was used to measure the PSD of the aggregates. The particle-size distribution (PSD) of the solid ingredients of the concretes at a distribution modulus of 0.3 is shown in Fig. 2.6 and Fig. 2.7. The mixtures are explained in more detail in the next section.

A standard pan mixer with planetary motion blades was used for producing flowing concretes. First, cement and sand were blended in a dry state for one minute. Then, about 75% of the mixing water was added while further mixing for 90 s. Afterward, a solution of the superplasticizer and the remaining water was added and mixed for one minute. Finally, the coarse aggregates were added and mixed for another two minutes. Superplasticizer was added at the end of the mixing sequence to prevent possible competing of superplasticizer molecules with calcium sulfate present in the cement to combine with $C_3A$. It ensured that all the superplasticizer molecules were kept ready to make concrete more flowable [106].

The flow table test was used to analyze the fresh properties of flowing concretes according to EN 12350-5 [83]. First, the flow table was cleaned and damped with a moist cloth. Next, the mold was filled with concrete in two layers, where each layer was tamped ten times. After waiting for 30 s, the mod was raised over a period of 1 to 3 s. Then, the flow was checked for segregation and bleeding. The consistency was the average of maximum dimensions of concrete spread, in two directions parallel to the table edges, measured to the nearest 10 mm.
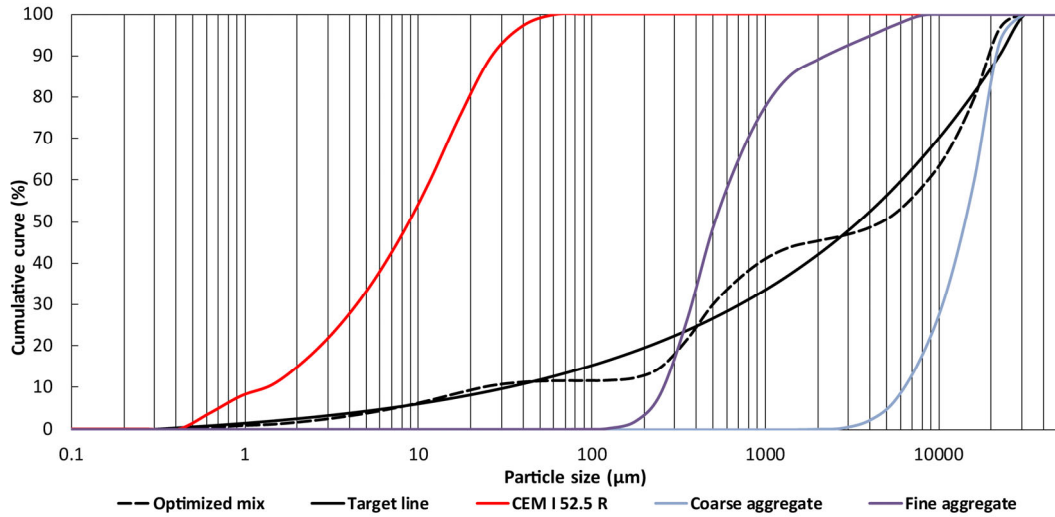
**Figure 2.6:** Particle-size distribution of different ingredients of the flowing concrete containing CEM I. The target line was computed by the modified Andreasen and Andersen model at the distribution modulus of 0.3. The optimized mix is the best fit of the ingredients for the target line.
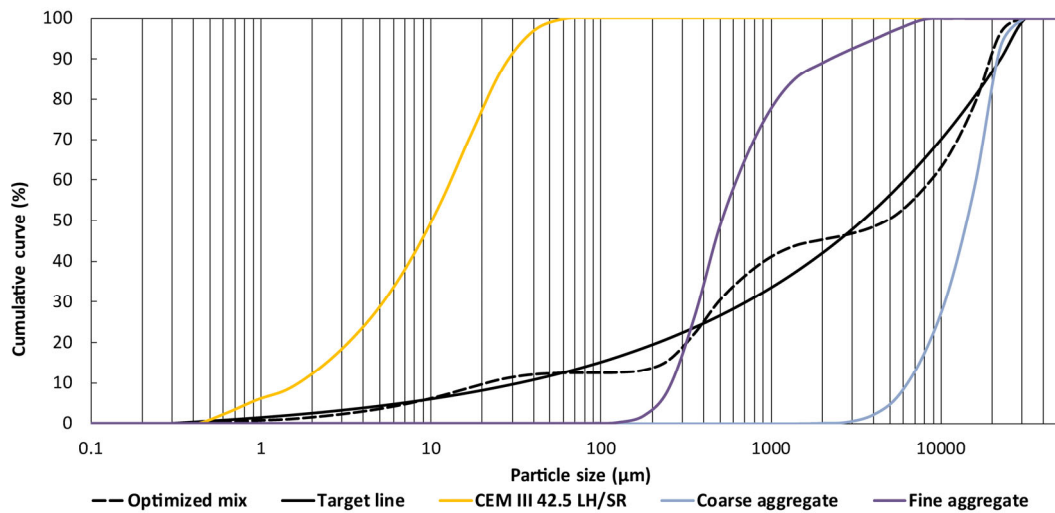


**Figure 2.7:** Particle-size distribution of different ingredients of the flowing concrete containing CEM III. The target line was computed by the modified Andreasen and Andersen model at the distribution modulus of 0.3. The optimized mix is the best fit of the ingredients for the target line.

After mixing, concrete was poured into six cube molds ($150 \times 150 \times 150$ mm$^3$) and covered by a plastic film to prevent moisture loss. The samples were unmolded approximately 24 h after casting and then submerged in water at 20 °C for curing. The compressive strength tests were performed after 28 and 98 days, according to EN 12390-3 [107].

Furthermore, concrete was poured into three prism molds ($100 \times 100 \times 200$ mm$^3$) to measure free drying shrinkage and report their average result. The specimens were unmolded

24 h after casting to install vibrating wire strain gages. The specimens were dried in a climate chamber at 20 °C and 60% relative humidity. The vibrating wire strain gages work with the principle of an electric guitar. They are composed of two end pieces joined by a tube that protects a length of steel wire. An electromagnet is placed in a protective housing located at the center of the tube. The exterior forces applied on the strain gage modify the tension in the wire and the wire's resonant frequency, which is read by the electromagnet.

The vibrating wire readings were drying shrinkage since in concrete having w/c greater than 0.45, the autogenous shrinkage is negligible compared to drying shrinkage [108,109]. This insignificance is thanks to two factors: (1) excess water more than required for full hydration of cement, and (2) large, well-connected capillary pores [108,109].

### 2.4.2   Mixtures

As explained in the previous section, the modified A&A model was used to design FC mixtures. A factorial design was employed at two levels with three factors, including two quantitative factors and a single qualitative factor:

1) Distribution modulus of the modified A&A model ($q = 0.35$, $q = 0.3$),

2) Cement content (300 kg/m$^3$ and 260 kg/m$^3$),

3) Cement type (CEM I 52.5R and CEM III 42.5 LH/SR from ENCI, the Netherlands).

This choice of distribution moduli ($q = 0.35$, $q = 0.3$) was based on the previous tests performed by the authors and the scientific literature discussed in section 2.3. The choice of the cement content was based on the EN 206 [84] where:

1) The minimum cement content for the exposure class of XC 1 (Level 1 carbonation-induced corrosion) is stated as 260 kg/m$^3$.

2) The minimum cement content for the exposure classes of XS 1 and XD 1 (Level 1 chloride-induced corrosion due to seawater and chloride other than seawater), XF 1 (Level 1 freeze/thaw attack), and XA 1 (Level 1 aggressive chemical environments) is stated as 300 kg/m$^3$.

The choice of the cement types was based on their widespread usage in the manufacture of concrete floors in different seasons of the year. The cement CEM I 52.5 R has a rapid hydration rate and is usually used for concreting in winter, while the cement CEM III 42.5 LH/SR has a low hydration rate and is usually used for concreting in summer [104,105]. A higher dosage of superplasticizer was used in samples with 260 kg/m$^3$. The water content in

these samples was only 130 kg/m³ (compared to 150 kg/m³ water in samples with 300 kg/m³ cement), and the higher SP dosage helped to improve flowability.

The coded design consisted of eight formulations, as shown in the table on the left of Fig. 2.8. Each data value was for the response yield averaged over three duplicate measurements. For example, a run using the lower amount of distribution modulus ($q = 0.35$), the lower content of cement (260 kg/m³), and the CEM I was coded as $(- - -)$ or run 1. As shown in Fig. 2.8, these eight formulations can be represented by the vertices of a cube. If the cube center is considered the origin of a three-dimensional coordinate system, then the factors can be identified by the coordinates of these points [110]. Table 2.2 presents the concrete mix compositions.
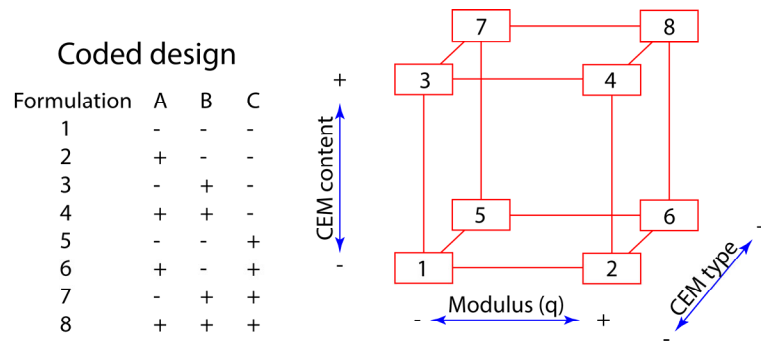


**Figure 2.8:** A $2^3$ factorial experimental design: (Left) Coded design in standard order (Right) Cube plot of numbered runs used to study the influence of three factors.

**Table 2.2:** Concrete mix compositions at the water-cement ratio of 0.50.

| Designation | Distribution modulus ($q$) | Cement type | Cement (kg/m³) | Sand (kg/m³) | Gravel (kg/m³) | Water (kg/m³) | SP (%) |
|---|---|---|---|---|---|---|---|
| C1 | 0.30 | CEM I | 260 | 912.0 | 1142.4 | 130 | 1.9% |
| C2 | 0.35 | CEM I | 260 | 780.0 | 1274.4 | 130 | 1.9% |
| C3 | 0.30 | CEM I | 300 | 843.1 | 1123.3 | 150 | 1.3% |
| C4 | 0.35 | CEM I | 300 | 714.2 | 1252.2 | 150 | 1.3% |
| C5 | 0.30 | CEM III | 260 | 888.6 | 1146.2 | 130 | 1.9% |
| C6 | 0.35 | CEM III | 260 | 756.6 | 1278.2 | 130 | 1.9% |
| C7 | 0.30 | CEM III | 300 | 816.1 | 1127.7 | 150 | 1.3% |
| C8 | 0.35 | CEM III | 300 | 687.2 | 1256.6 | 150 | 1.3% |

Furthermore, a Pareto analysis at a 5% significance level was performed to determine which effects (main and interaction) contribute the most to the consistency and shrinkage response variability. The main effects were: (A) modulus, (B) cement content, and (C) cement type. The interaction terms were AB, AC, and BC.

### 2.4.3   Results

Fig. 2.9a presents the consistency of mixtures, measured by flow table test for the eight combinations of factors at the corners of a cube. No indication of segregation was observed during measurements. The Pareto analysis showed that among the factors, the cement content was the most statistically significant factor to the consistency response variability (adjusted $R^2$ = 98.5% and predicted $R^2$ = 86.3%). The analysis also showed that none of the interaction terms were statistically significant ($\alpha$ = 5%). In other words, both distribution moduli ($q$ = 0.35 and $q$ = 0.30) produced workable cohesive, flowing concrete, and distribution modulus was not a statistically significant factor to the consistency response variability.

Fig. 2.9b shows the influence of distribution modulus on the consistency of mixtures. The average main effect of distribution modulus on flow diameter is +3 cm, which is greater at lower cement content. At 300 kg/m³, both distribution moduli ($q$ = 0.35 and $q$ = 0.30) provided cohesive workable flowing concrete. No indication of segregation and bleeding was found in the samples. Fig. 2.9c displays the influence of the cement content and SP dosage on the consistency of mixtures. The average main effect of cement content is +7 cm which is more than twofold that of the distribution modulus. In similar mixtures, a higher amount of powder is translatable into a higher volume of excess paste. Fig. 2.9d shows the influence of cement type on the consistency of mixtures. The average main effect of cement type is −2 cm, which is greater at higher cement content. This effect is insignificant as it is less than the tolerance of flow diameter test (± 30 mm), according to EN 206-1 [84].

Fig. 2.10a presents the 28-day strength of mixtures for the eight combinations of factors at the corners of a cube. Fig. 2.10b shows the influence of distribution modulus on the 28-day strength of mixtures. The strength of all the CEM I mixtures is above 37 MPa, which is the minimum cube strength for C30/37 compressive strength class in EN 206-1 [84]. The average main effect of the distribution modulus on the 28-day strength is +1.5 MPa, showing the two distribution moduli provide similar strength. Figs. 2.10c-d display the influence of cement content and type on the 28-day strength of mixtures. Mixtures containing CEM III have lower compressive strength due to the lower hydration speed of CEM III [105].
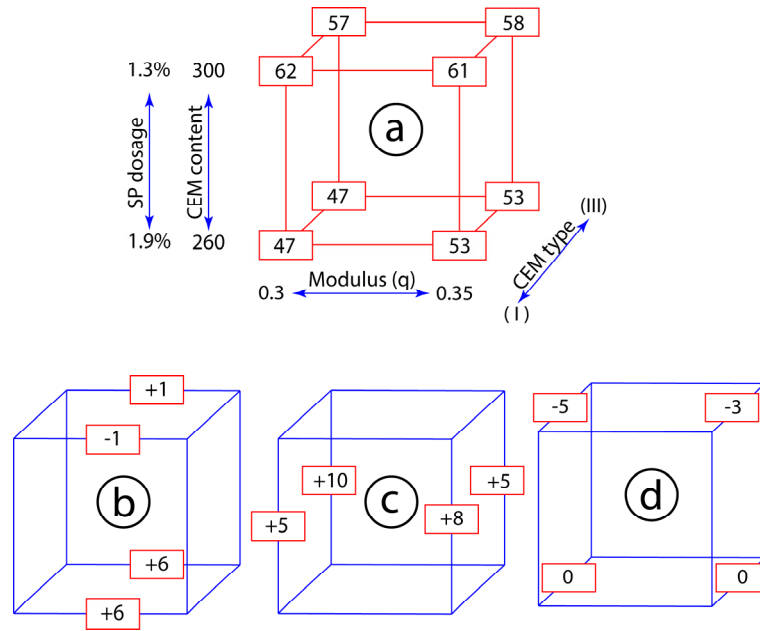
**Figure 2.9:** (Top) Cube plot of the consistency of mixtures (cm), measured by flow table test. (Bottom) The influence of factors on flow diameter: (b) the influence of distribution modulus, (c) the influence of cement content and SP dosage, (d) the influence of cement type.
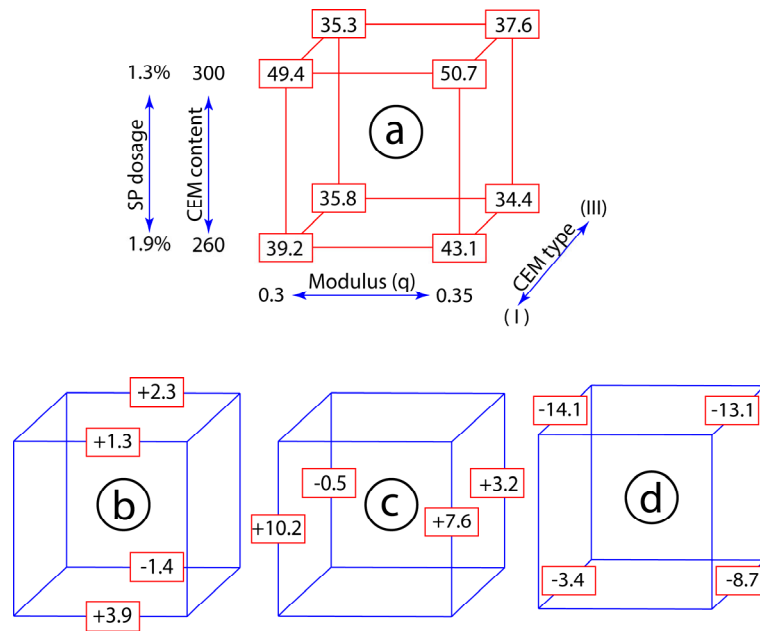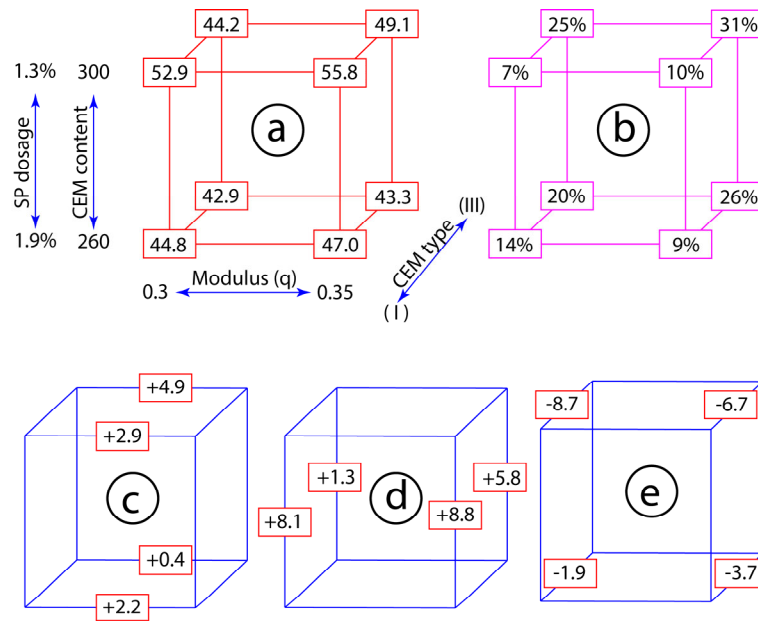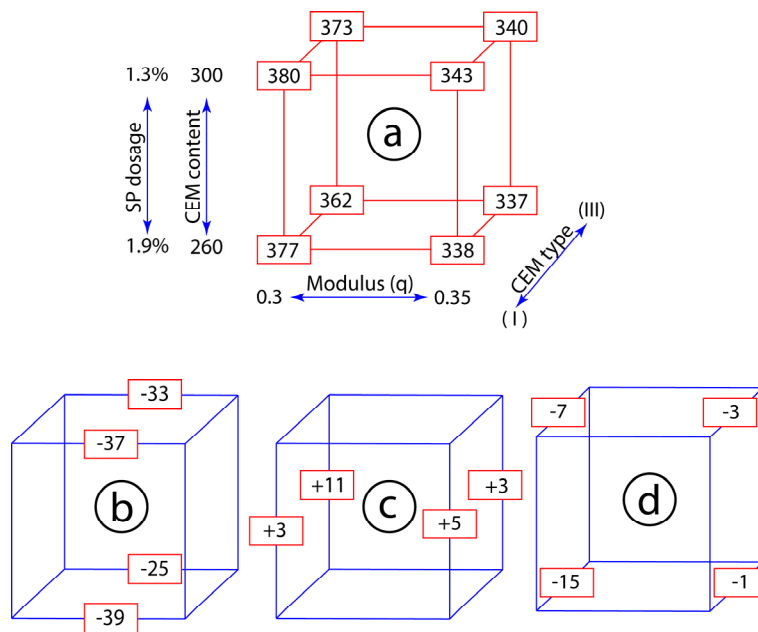


**Figure 2.10:** (Top) Cube plot of 28-day strength (MPa). (Bottom) The influence of factors on 28-day strength: (b) the influence of distribution modulus, (c) the influence of cement content and SP dosage, (d) the influence of cement type.

Fig. 2.11a presents the 98-day strength of mixtures for the eight combinations of factors at the corners of a cube. Compared to the 28-day strength of the mixtures (Fig. 2.10), the increase in 98-day strength is more significant in CEM III mixtures. Rapid strength gain in CEM I mixtures is associated with the high surface area of this type of cement (Blaine of ca. 527 m$^2$/kg [104]). Fig. 2.11c shows the influence of the distribution modulus on the 98-day strength of mixtures. The strength of the mixtures is above 43 MPa, which is considered sufficient for most flowing concrete applications. The average main effect of distribution modulus on the 98-day strength is +2.6 MPa, and the two distribution moduli provide similar adequate strength. Fig. 2.11d demonstrates the influence of cement content on the 98-day strength of mixtures. The average main effect of cement content is +6 MPa, and a higher cement content results in higher strength. Fig. 2.11e shows the influence of cement type on the 28-day strength of mixtures. Mixtures containing CEM III have lower compressive strength due to the lower hydration speed of CEM III [105].

Fig. 2.12a presents the 98-day drying shrinkage of the eight combinations of factors at the corners of a cube. The Pareto analysis showed that among the factors, the distribution modulus was the most statistically significant factor to the 98-day shrinkage response variability (adjusted $R^2 = 96.4\%$ and predicted $R^2 = 67.3\%$). The analysis also showed that none of the interaction terms were statistically insignificant ($\alpha = 5\%$).

The shrinkage values are less than 380 microstrain ($\mu\varepsilon$), showing that the mix design method can make low shrinkage flowing concrete mixtures. Fig. 2.12b illustrates the influence of distribution modulus on the drying shrinkage of mixtures. Its average main effect is +33.5 microstrain and is associated with a higher coarse-to-fine ratio. Fig 2.12c shows the influence of cement content on the drying shrinkage of mixtures. Its average main effect is +5.5 microstrain, which is due to the difference in the water content of the mixtures (see Table 2.2). Fig. 2.12d shows the influence of cement type on the drying shrinkage of mixtures.

The lesser shrinkage in CEM III samples may be attributed to the lower hydration speed in this type of cement [105]. These results are in line with previous studies where 60% volume replacement of cement with slag exhibited 22% and 12% lower drying shrinkage at 30 days and 356 days, respectively [111].

**Figure 2.11:** (Top) Cube plot of 98-day strength (MPa) and the percentage increase in strength compared to the 28-day strength. (Bottom) The influence of factors on 98-day strength: (c) the influence of distribution modulus, (d) the influence of cement content and SP dosage, (e) the influence of cement type.



**Figure 2.12:** (Top) Cube plot of 98-day shrinkage (microstrain, μm/m). (Bottom) The influence of factors on 98-day shrinkage: (b) the influence of distribution modulus, (c) the influence of cement content and SP dosage, (d) the influence of cement type.

## 2.5    Conclusions

In the present chapter, the pumpability of the modified A&A model at a distribution modulus of 0.35 to 0.2 was compared and contrasted with the technical literature and the recommendations of the American Concrete Institute (ACI). A factorial design was used to investigate the consistency, compressive strength, and drying shrinkage of flowing concrete mixtures. Based on the properties assessed and the results obtained, the following conclusions can be drawn:

- The modified A&A model can optimize the particle size distribution of concrete to produce pumpable concretes according to the ACI 211.9R-18 [70]. The distribution modulus of the model controls the combined grading, the ratio of coarse-to-fine aggregates, and the percentage of fine aggregates passing 300 μm and 150 μm.

- When designing concrete with this model, a distribution modulus of 0.35 is the recommended boundary limit for ideal pumpability. A smaller than 0.35 distribution modulus results in ideal-for-pumping mixtures.

- When designing concrete with this model, lowering the distribution modulus pushes the cumulated combined grading further above the recommended boundary limit for ideal pumpability. It also increases the percentage of fine aggregates passing 300 μm and 150 μm while keeping them within the recommended limits by ACI 211.9R-18 [70].

- A good correlation was established between the distribution modulus of the modified A&A model and the drying shrinkage of concrete. A high distribution modulus in the model results in a high coarse-to-fine aggregate ratio and lowers the drying shrinkage of concrete.

# Rapidly expansive light-burnt magnesia to modify volume change

*Expansive magnesia is currently only used to compensate for cooling shrinkage of large concrete monoliths by producing expansion a few months after casting. This chapter explores the applicability of rapidly expansive magnesia (MgO-RE) as a novel shrinkage-compensating admixture (SCA), extending the application of light-burnt magnesia to drying shrinkage of concrete. The composition, microstructure, morphology, adsorption isotherm, and pore structure of MgO-RE are compared to those of cooling shrinkage magnesia (MgO-CS). The expansive performance of MgO-RE in mortar and concrete at two water-cement ratios and four curing conditions is reported. Results showed that compared to MgO-CS, MgO-RE has smaller crystallite size, higher porosity, and lesser sintering oxides. The expansion and shrinkage of concretes containing MgO-RE are comparable to those of concretes containing calcium-hydroxide based SCAs, making MgO-RE a suitable SCA for concrete.*

## 3.1    Introduction

Drying shrinkage and cooling shrinkage often cause cracking in concrete when not properly mitigated [3,4]. Drying shrinkage is the volume change due to chemical and physical moisture loss in concrete during the hardening period [112,113]. In order to offset strains caused by drying shrinkage, shrinkage-compensating admixtures (SCAs) can be added to concrete [16]. Two commonly used types of SCAs are ettringite-based and calcium-hydroxide based SCAs [71,72]. Ettringite-based SCAs contain sulfoaluminates and produce expansive ettringite after hydration [15]. Calcium-hydroxide based SCAs contain calcium oxide, which produces expansion by producing calcium hydroxide after hydration [15,114].

In contrast to drying shrinkage, which initiates almost after concrete hardening, cooling shrinkage occurs up to a few months after hardening [115]. Cooling shrinkage is the contraction in massive concrete structures due to the accumulation and late dissipation of thermal energy, produced during hydration [115]. In order to offset strains caused by cooling shrinkage, magnesia-based expansive admixtures can be added to concrete [116,117]. These can create expansion a few months after casting when cooling shrinkage begins [116,117]. Magnesia is rare in nature and is usually produced by the calcination of magnesite [29]. The expansive properties of magnesia are a function of calcination temperature, residence time, particle size, and impurities in the parent solid [23,24]. Moreover, supplementary cementitious materials, curing temperature and environment influence expansive properties of magnesia in concrete [118]. More information on the application of expansive magnesia is provided in these recent reviews by Mo et. al. [119], Walling and Provis [28], and Du [120]. Research on the application of magnesia in concrete has been mostly restricted to the use of slow-hydrating magnesia for compensating cooling shrinkage of concrete. The acid reactivity of cooling shrinkage magnesia is typically more than 50 seconds [25] and it needs water curing or thermal curing for activation [26,27].

Rapidly expansive magnesia reacts rapidly with water to form an expansive hydration product (brucite) and has the potential of being utilized as an SCA in concrete. One of the advantages of magnesia to currently used ettringite-based or calcium hydroxide-based SCAs is the high stability of brucite [28,29]. Unlike magnesia, the hydration product of ettringite-based SCAs is unstable at high temperatures and the hydration product of calcium oxide based SCAs is unstable in corrosive environments. In addition, magnesia requires a small amount of water for curing compared to the ettringite-based SCAs and its expansion can be adjusted during production. Surprisingly, the impact of rapidly expansive magnesia on shrinkage compensation of concrete is seldom studied and it is unclear to what extent it can perform as an SCA.

This chapter has two aims. Firstly, it compares and contrasts the structure of rapidly expanding magnesia with that of cooling shrinkage magnesia. Secondly, it analyzes the performance of rapidly expansive magnesia in mortars and concrete in different curing conditions. To fulfil the first aim, a sample of cooling shrinkage magnesia and a sample of rapidly expansive magnesia are investigated. The crystal structure and surface characteristics of the two samples are analyzed using X-ray diffraction (XRD), environmental scanning electron microscopy (ESEM), physisorption isotherms, BET surface area, and BJH pore size distribution. To fulfil the second aim, four different curing conditions, two cement types

and two water-cement ratios are analyzed. The present research sheds light on the difference between cooling shrinkage magnesia and rapidly expansive magnesia and provides data on the performance of rapidly expansive magnesia in mortars and concrete in different curing conditions. The findings will contribute to a deeper understanding of the influence of the structure of magnesia in rapid expansion in concrete and offers some important insights into the link between the curing and performance of rapidly expansive magnesia in mortar and concrete.

## 3.2 Materials and methods

### 3.2.1 Materials

The present research involves analyzing two types of light-burnt magnesia: (1) rapidly expansive magnesia (MgO-RE), and (2) cooling shrinkage magnesia (MgO-CS). The magnesia samples were obtained from Magnesia GmbH, Germany. The acid reactivity of the samples was measured based on the time required for 5.00 g of magnesia to neutralize a diluted solution of 100 mL of 1.0 N acetic acid in 300 mL of deionized water at 25±1 °C [29] and is shown in Table 3.1. The acid reactivity of the MgO-CS was 145 s and that of the MgO-RE was 9 seconds. Acid reactivity is a common test for determining the reactivity of caustic-calcine magnesia [29] and is used in Chinese standard DL/T 5296-2013 [25] to classify magnesium oxide expansive admixtures for use in hydraulic concrete. The acid reactivity between 50 s and 500 s is classified as Type I and that between 200 s and 300 s is categorized as Type II expansive magnesia in the Chinese standard [25]. However, this standard does not give information regarding magnesia with acid reactivity smaller than 50 s [25]. The acid reactivity is inversely proportional to the specific surface area of magnesia and directly proportional to the calcination temperature [23].

**Table** 3.1: Acid reactivity time of magnesia samples, measured according to [29].

| Item | MgO-CS | MgO-RE |
|---|---|---|
| Acid reactivity time (s) | 145 | 9 |

CEM I 52.5 R and CEM III 42.5 LH/SR cements provided by ENCI (the Netherlands) [104,105] were utilized to produce mortars and concretes. CEM I 52.5 R was fine Portland cement (Blaine of ca. 527 m$^2$/kg [104]) and CEM III/B 42.5 LH/SR was a fine binary blend of slag and Portland clinker (Blaine of ca. 488 m$^2$/kg [105]). The chemical composition of

both cement types was determined by X-ray fluorescence (XRF) and is shown in Table 3.2. A CEN standard sand was used for making standard mortars [121]. River gravel with the maximum size of aggregate (MSA) of 31.5 mm and river sand were used for producing concrete. A polycarboxylic ether-based superplasticizer (SP) with solid content of 12% was used to adjust the flow properties of flowing concretes. The dosage of the SP refers to the weight of the solution in water as a percentage of the weight of cement. The water in the superplasticizer solution was deducted from the mixing water. The particle size distribution (PSD) of the powders was measured employing a Malvern Mastersizer 2000 and sieve analysis was used to measure the PSD of the aggregates.

**Table 3.2:** Chemical composition of CEM I 52.5 R and CEM III 42.5 LH/SR, measured by XRF (in weight percent).

| Mineral compound | MgO | $Al_2O_3$ | $SiO_2$ | $SO_3$ | CaO | $Fe_2O_3$ | LOI |
|---|---|---|---|---|---|---|---|
| CEM I | 1.6 | 6.2 | 17.7 | 3.0 | 64.7 | 3.5 | 2.5 |
| CEM III | 4.6 | 9.5 | 28.2 | 5.1 | 49.8 | 1.3 | 0.3 |

Table 3.3 and Table 3.4 display the mortar mixture compositions. The name of each mortar specimen consists of four parts:

(1) Cement type (C1: CEM I 52.5 R, and CIII: CEM III 42.5 LH/SR);

(2) Magnesia dosage (M0: without magnesia, and M10: 10% magnesia);

(3) Water-cement ratio (w/c0.6: w/c ratio of 0.6, and w/c0.5: w/c ratio of 0.5);

(4) Curing method:

- NO: exposed to air at the temperature of 20 °C and the relative humidity (RH) of 0.65.

- WA: cured under water for 7 days, then exposed to air at the temperature of 20 °C and RH of 0.65.

- WB: wrapped in wet burlap for 7 days, then exposed to air at the temperature of 20 °C and RH of 0.65.

- PL: wrapped in plastic film for 7 days, then exposed to air at the temperature of 20 °C and RH of 0.65.

Here, similar to Chapter 2, the choice of the cement types was based on their widespread usage in the manufacture of concrete floors in different seasons of the year. The cement CEM I 52.5 R has a rapid hydration rate and is usually used for concreting in winter, while

the cement CEM III 42.5 LH/SR has a low hydration rate and is usually used for concreting in summer [104,105].

The choice of magnesia dosage was based on the previous tests performed by the authors. The choice of the w/c ratios was based on their widespread usage in the manufacture of concrete floors. In addition, two different w/c ratios could also provide information on the influence of different water contents on the expansion of specimens.

The modified Andreasen and Andersen model was utilized to design concrete mixtures (see Chapter 2) [87,92]

$$P(d) = \frac{d^q - d^q_{min}}{d^q_{max} - d^q_{min}} \tag{3.1}$$

where $d$ is the particle size, $d_{min}$ the minimum particle size, $d_{max}$ the maximum particle size and $P(d)$ the cumulative fraction of the total solids being smaller than size $d$.

The maximum size of coarse aggregates for making concrete mixtures was 31.5 mm, and the minimum size of the powder (e.g., cement) was 0.275 μm. The choice of cement content was based on the results of Chapter 2 (i.e., C3 and C7 mixtures in Table 2.2) and also because the minimum cement content for the exposure classes of XS 1 and XD 1 (Level 1 chloride-induced corrosion due to seawater and chloride other than seawater), XF 1 (Level 1 freeze/thaw attack), and XA 1 (Level 1 aggressive chemical environments) in EN 206 [84] is stated as 300 kg/m³. The particle-size distribution (PSD) of the solid ingredients of the concretes at a distribution modulus of 0.3 are shown in Fig. 3.1 and Fig. 3.2.

Table 3.5 presents the concrete mix compositions. The name of each concrete sample consists of three parts:

(1) Cement type (C1: CEM I 52.5R, and CIII: CEM III 42.5 LH/SR);

(2) Magnesia-cement percentage (M0: without magnesia, M5: 5% magnesia, and M10: 10% magnesia);

(3) Curing method: cured under water for seven days, then exposed to air with the relative humidity of 0.65 and temperature of 20 °C.

**Table 3.3:** Mortar mix compositions at the w/c ratio of 0.6.

| Designation | Cement type | Cement (g) | Water (g) | Sand (g) | MgO (g) | Curing (7days) |
|---|---|---|---|---|---|---|
| C1-M0-w/c0.6-NO | CEM I | 450 | 270 | 1231.2 | 0 | Air |
| C1-M0-w/c0.6-WA | CEM I | 450 | 270 | 1231.2 | 0 | Water |
| C1-M0-w/c0.6-WB | CEM I | 450 | 270 | 1231.2 | 0 | Wet burlap |
| C1-M0-w/c0.6-PF | CEM I | 450 | 270 | 1231.2 | 0 | Wrapped in plastic film |
| C1-M10-w/c0.6-NO | CEM I | 450 | 270 | 1193.6 | 45 | Air |
| C1-M10-w/c0.6-WA | CEM I | 450 | 270 | 1193.6 | 45 | Water |
| C1-M10-w/c0.6-WB | CEM I | 450 | 270 | 1193.6 | 45 | Wet burlap |
| C1-M10-w/c0.6-PF | CEM I | 450 | 270 | 1193.6 | 45 | Wrapped in plastic film |
| C3-M0-w/c0.6-NO | CEM III | 450 | 270 | 1187.3 | 0 | Air |
| C3-M0-w/c0.6-WA | CEM III | 450 | 270 | 1187.3 | 0 | Water |
| C3-M0-w/c0.6-WB | CEM III | 450 | 270 | 1187.3 | 0 | Wet burlap |
| C3-M0-w/c0.6-PF | CEM III | 450 | 270 | 1187.3 | 0 | Wrapped in plastic film |
| C3-M10-w/c0.6-NO | CEM III | 450 | 270 | 1145.9 | 45 | Air |
| C3-M10-w/c0.6-WA | CEM III | 450 | 270 | 1145.9 | 45 | Water |
| C3-M10-w/c0.6-WB | CEM III | 450 | 270 | 1145.9 | 45 | Wet burlap |
| C3-M10-w/c0.6-PF | CEM III | 450 | 270 | 1145.9 | 45 | Wrapped in plastic film |

**Table 3.4:** Mortar mix compositions at the w/c ratio of 0.5.

| Designation | Cement type | Cement (g) | Water (g) | Sand (g) | MgO (g) | Curing (7days) |
|---|---|---|---|---|---|---|
| C1-M0-w/c0.5-WB | CEM I | 450 | 225 | 1350 | 0 | Wet burlap |
| C1-M0-w/c0.5-PF | CEM I | 450 | 225 | 1350 | 0 | Wrapped in plastic film |
| C1-M10-w/c0.5-NO | CEM I | 450 | 225 | 1312.4 | 45 | Air |
| C1-M10-w/c0.5-WA | CEM I | 450 | 225 | 1312.4 | 45 | Water |
| C1-M10-w/c0.5-WB | CEM I | 450 | 225 | 1312.4 | 45 | Wet burlap |
| C1-M10-w/c0.5-PF | CEM I | 450 | 225 | 1312.4 | 45 | Wrapped in plastic film |
| C3-M0-w/c0.5-WB | CEM III | 450 | 225 | 1306.1 | 0 | Wet burlap |
| C3-M0-w/c0.5-PF | CEM III | 450 | 225 | 1306.1 | 0 | Wrapped in plastic film |
| C3-M10-w/c0.5-NO | CEM III | 450 | 225 | 1264.7 | 45 | Air |
| C3-M10-w/c0.5-WA | CEM III | 450 | 225 | 1264.7 | 45 | Water |
| C3-M10-w/c0.5-WB | CEM III | 450 | 225 | 1264.7 | 45 | Wet burlap |
| C3-M10-w/c0.5-PF | CEM III | 450 | 225 | 1264.7 | 45 | Wrapped in plastic film |
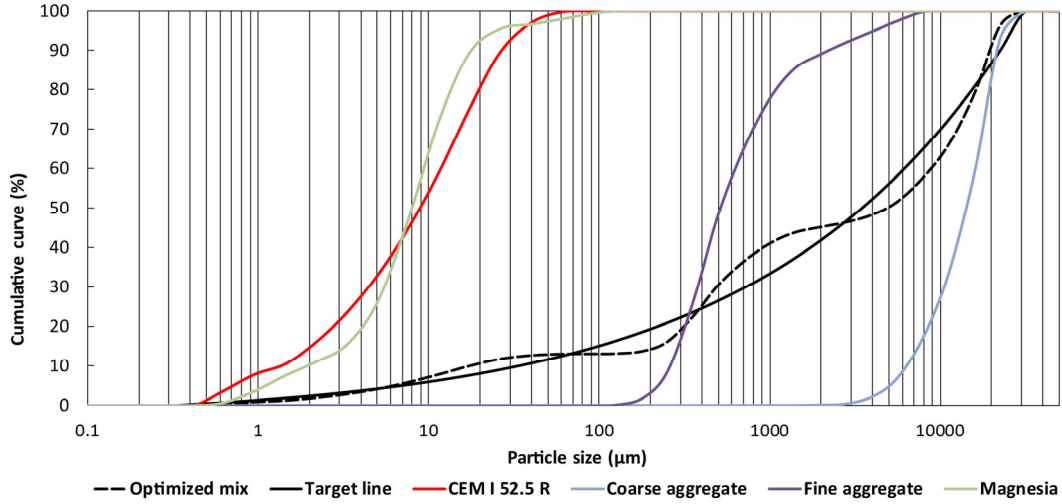
**Figure 3.1:** Particle-size distribution of different ingredients of the concrete mixtures containing CEM I. The modified A&A model (see Eq. 3.1) computed the target line at the distribution modulus $q = 0.3$.
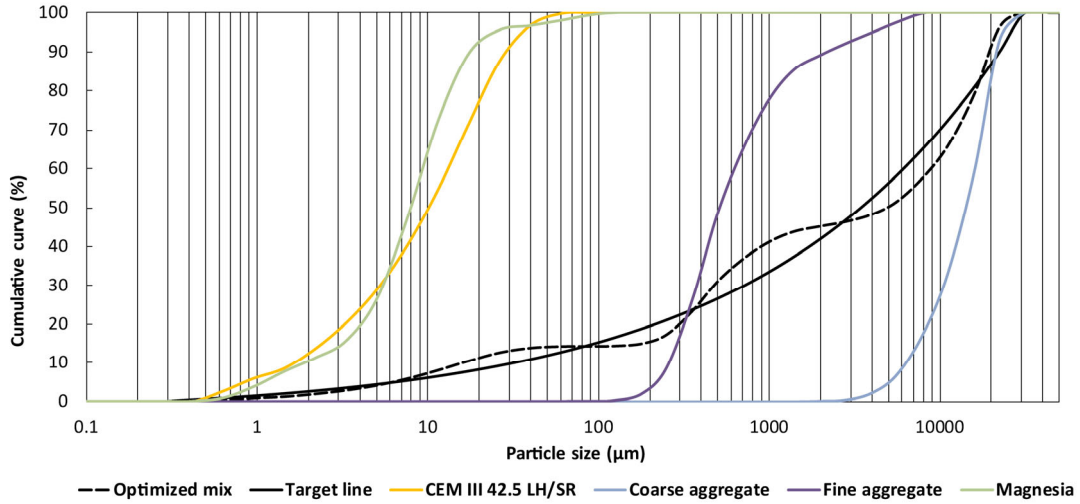


**Figure 3.2:** Particle-size distribution of different ingredients of the concrete mixtures containing CEM III. The modified A&A model (see Eq. 3.1) computed the target line at the distribution modulus $q = 0.3$.

**Table 3.5:** Concrete mix compositions at the water-powder ratio of 0.55.

| Designation | Cement type | Cement (kg/m³) | MgO (kg/m³) | Sand (kg/m³) | Gravel (kg/m³) | Water (kg/m³) | SP (%) |
|---|---|---|---|---|---|---|---|
| C1-M0 | CEM I | 300 | 0 | 822.36 | 1103.96 | 165 | 1.2% |
| C1-M5 | CEM I | 300 | 15 | 802.61 | 1105.09 | 173.25 | 1.2% |
| C1-M10 | CEM I | 300 | 30 | 782.86 | 1106.22 | 181.5 | 1.2% |
| C3-M0 | CEM III | 300 | 0 | 795.38 | 1108.39 | 165 | 1.2% |
| C3-M5 | CEM III | 300 | 15 | 775.41 | 1109.56 | 173.25 | 1.2% |
| C3-M10 | CEM III | 300 | 30 | 755.43 | 1110.73 | 181.5 | 1.2% |

### 3.2.2 Methodology

*Main oxide composition*

Loss on ignition was measured according to ASTM C25 [122]. The residues were blended with a non-wetting agent (LiBr) and flux ($LiBO_4$ and $Li_2BO_7$). The blends were fused at 1050°C in a fluxer (classisse leNeo) and cast in molds to obtain fused beads. The fused beads were analyzed by X-ray Fluorescence (PANalytical Epsilon 3, OMNIAN method) to measure chemical compositions.

*Microstructure*

A D4 ENDEAVOR X-ray Diffractometer from Bruker, equipped with LynxEye detector and Co-Tubes ($K\alpha_1$ 1.70901 Å, $K\alpha_2$ 1.7929 Å), was used to examine the crystalline structure. DIFFRAC.EVA (Bruker) was utilized to identify crystalline phases and Topas (Bruker) was employed to determine crystallite sizes. The Scherrer equation was used to calculate the average crystallite size [123]

$$\text{Size} = \frac{K\lambda}{\Delta\theta \cdot \cos\theta} \tag{3.2}$$

where $\Delta\theta$ is the breadth of a particular peak, $\lambda$ is the wavelength of the X-ray radiation employed and $K$ is a constant.

The morphology of magnesia particles was investigated using a FEI quanta 600 environmental scanning electron microscope. Before the investigation, in order to improve the conductivity of the sample surface, all the samples were sputtered with an approximately 15 nm layer of gold. The micrographs were taken using both secondary and back-scattered electron detectors (MIX mode) at 5 kV with a spot of 3.0.

*Adsorption mechanism and pore structure*

A complete physisorption isotherm was measured for all magnesia samples. The tests were conducted at cryogenic temperature of the boiling point of liquid nitrogen (77 K), using a Micromeritics TriStar II analyzer. The adsorption isotherms were plotted using [124]

$$\frac{V^a}{m^s} = f\left(\frac{p}{p^0}\right) T \tag{3.3}$$

where $V^a$ is the amount of adsorbate, $m^s$ the mass of solid, $p$ the actual adsorbing gas pressure, $p^0$ the saturation pressure of the adsorbing gas at $T$, and $T$ the thermodynamic temperature. The adsorption isotherm was used to calculate the BET surface area.

The characterization of the pore structure of materials by the BJH method involves the application of the Kelvin equation [124]

$$\ln \frac{p}{p^0} = -\left(\frac{2\gamma v^l}{r_K RT}\right) \tag{3.4}$$

where $\gamma$ is the surface tension, $v^l$ the molar volume of the liquid (i.e., the condensed adsorptive), $r_K$ the Kelvin radius, $R$ the gas constant, $T$ the thermodynamic temperature, and $\frac{p}{p^0}$ as introducd previously. The computation procedure for pore size distribution by BJH method can be found in [124].

In this study, the Frenkel-Halsey-Hill (FHH) equation for multilayer analysis was utilized in the Tristar 3020 analysis program for calculating the adsorbed layer remaining on the pore walls in each step of the BJH method, which gives the following formula for nitrogen adsorbed at 77 K [124]

$$t = 0.354 \left(\frac{-5}{\ln \frac{p}{p^0}}\right)^{\frac{1}{3}} \tag{3.5}$$

where $t$ is the thickness of multimolecular layer (nm), and $\frac{p}{p^0}$ as defined previously.

*Expansive properties*

The mortars were prepared using a Hobart mixer. The mixing procedure started with blending cement and magnesia. Next, water and binder were mixed at low speed for 1 min. Then, the mixer was stopped for 90 s, during which the mortar adhering to the mixer bowl was scraped. Finally, the mixing was continued at a high speed for 2 min.

After mixing, the mortar mixtures were cast into three plastic prism molds, $40 \times 40 \times 160$ mm$^3$ and were compacted using a jolting machine. Six hours after casting, the samples were unmolded, and the strain measurement pins were installed on two parallel sides of the

specimens. After measuring the distance between the pins on both sides, the specimens were submerged in water at 20 °C for curing. After 7 days of water curing, the specimens were dried in a climate chamber at 20 °C and 60% relative humidity.

A standard pan mixer with planetary motion blades was used for producing concrete specimens. First, cement, magnesia powder and sand were blended in a dry state for one minute. Then, about 75% of the mixing water was added while further mixing for 90 s. Afterward, a solution of the superplasticizer and the remaining water was added and mixed for one minute. Finally, the coarse aggregates were added and mixed for another two minutes. Superplasticizer was added at the end of the mixing sequence in order to prevent possible competing of superplasticizer molecules with calcium sulfate present in the cement to combine with $C_3A$ and keep all the superplasticizer molecules ready to make concrete more flowable [106].

After mixing, the concrete was poured into three prism molds ($100 \times 100 \times 200$ mm$^3$) to measure free drying shrinkage and report their average result. The specimens were unmolded 6 h after casting and vibrating wire strain gages were installed. Then, the specimens were submerged in water at 20 °C for curing. After 7 days of water curing, the specimens were dried in a climate chamber at 20 °C and 60% relative humidity.

## 3.3 Results and discussion

### 3.3.1 Main oxide composition

The chemical composition and loss on ignition of both samples are listed in Table 3.6. Both samples mainly consist of magnesium oxide (around 90%). The percentage of $SiO_2$ in MgO-RE is smaller than that in MgO-CS. The impurities caused by $Fe_2O_3$, $SiO_2$, and $Al_2O_3$ are known as sintering promoters in magnesia [24]. The loss on ignition (LOI) of MgO-RE is twice as much as that of MgO-CS. This may be attributed to the calcination process and a lower degree of decomposition of MgO-RE [23,24].

**Table 3.6:** Chemical composition of magnesia samples, measured by XRF (in weight percent).

| Item | MgO-CS | MgO-RE |
|---|---|---|
| MgO | 90.7 | 89.8 |
| LOI | 4.6 | 7 |
| $SiO_2$ | 1.3 | 0.2 |
| CaO | 2.4 | 0.9 |
| $Fe_2O_3$ | 0.0 | 0.1 |
| Other | 1.0 | 2.0 |

### 3.3.2 Microstructure

The main crystalline phases of the samples are shown in Fig. 3.3. All the samples mainly consist of periclase. Small concentrations of magnesite, calcite, and quartz are traceable in the samples. These data are consistent with the data measured by the XRF (Table 3.6) where CaO and $SiO_2$ were present.

The periclase peaks of the samples (Fig. 3.3) have different breadths and heights and indicate different crystal grain sizes in the samples. Table 3.7 lists the average crystallite sizes of the magnesia samples. The MgO-RE has smaller crystallite sizes. The average crystallite size of MgO-RE is only 8.1 nm, while that of the MgO-CS is 21.1 nm.
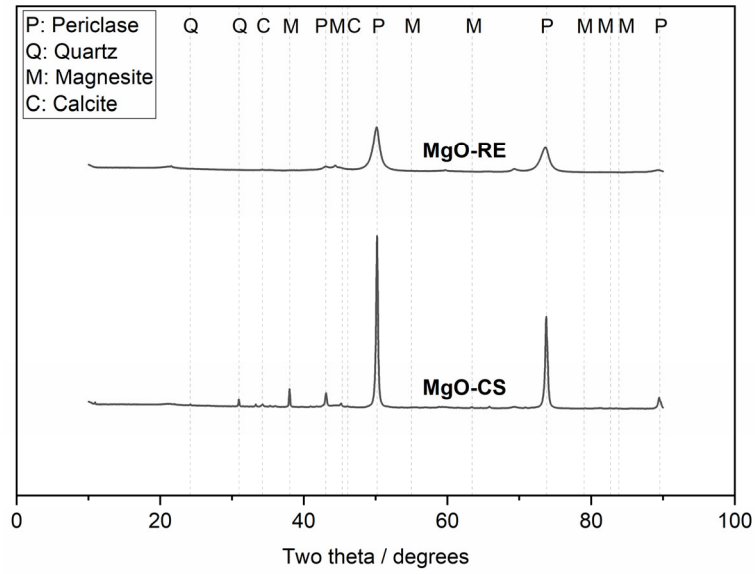
**Figure 3.3:** Mineral crystalline phases in different samples of magnesia, measured by XRD (P: periclase, Q: quartz, M: magnesite, C: calcite).

**Table 3.7:** Average crystallite size of different samples of magnesia.

| Item | MgO-CS | MgO-RE |
|---|---|---|
| Average crystallite size (nm) | 21.1 | 8.1 |
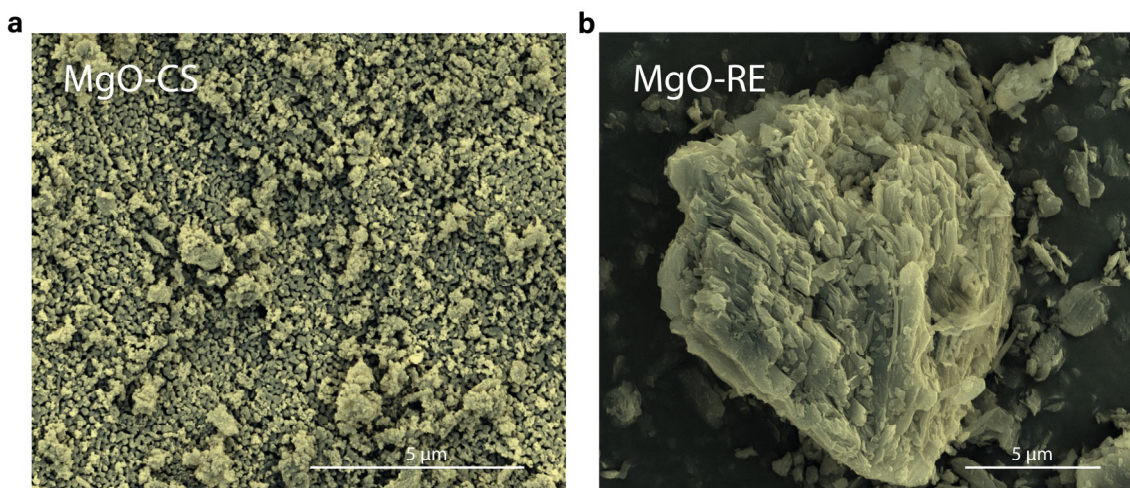


**Figure 3.4:** Morphology and the texture of the particles in the samples of magnesia, obtained by ESEM: (a) MgO-CS; (b) MgO-RE.

Fig. 3.4a-b shows the samples' morphology, taken by an environmental scanning electron microscope (ESEM). The micrographs of MgO-CS present a very high degree of sintering. This observation is in line with their big crystallite sizes in Table 3.7 and greater acid reactivity time in Table 3.1. On the other hand, the micrographs of MgO-RE show a very small degree of sintering. This observation is also in line with the small crystallite sizes in Table 3.7 and the short acid reactivity time in Table 3.1.

### 3.3.3   Adsorption mechanism and pore structure

The physisorption isotherms of the samples are shown in Fig. 3.5a-b. The physisorption isotherm of each sample consists of an adsorption and a desorption isotherm. The adsorption isotherm of MgO-CS consists of three regions: (1) a concave region to the $p/p^0$ axis, in the beginning, (2) a linear region in the middle, and (3) a convex region to the $p/p^0$ axis at the end. The first concave region is a result of high interaction between the adsorbate and the spots on the adsorbent with the highest energies. The more the adsorbates occupy highly energetic spots of the adsorbent, the higher the curve plateaus out. At the beginning of the linear region, a monolayer of adsorbate has already covered the adsorbent. The gradual shift from the first to the second stage of the isotherms indicates the possibility of overlap in the monolayer and multilayer adsorption of adsorbate to the adsorbent. The upsurge at the end of these adsorption isotherms is a result of the bulk condensation of the adsorbate to a liquid [125].

The physisorption isotherm of MgO-RE consists of three regions: (1) a region concave to the $p/p^0$ axis, in the beginning, (2) a linear region in the middle, and (3) an almost flat region at the end. Although the beginning and the middle region of MgO-RE are similar, the flat region is an indication of limited mesopore sizes in the sample [126,127].

Table 3.8 compares and contrasts the data on the BET surface area of the samples. MgO-CS has small surface area (18.2 $m^2/kg$) whereas MgO-RE has large surface area (176.7 $m^2/kg$).

Fig. 3.6a-b represent the pore size distribution of magnesia samples, calculated by BJH algorithms for the nitrogen adsorption at 77K. Most of the pore volume in MgO-CS is in mesopores bigger than 20 nm. By contrast, the pore structure in MgO-RE is almost uniform and most of the pores are smaller than 10 nm.
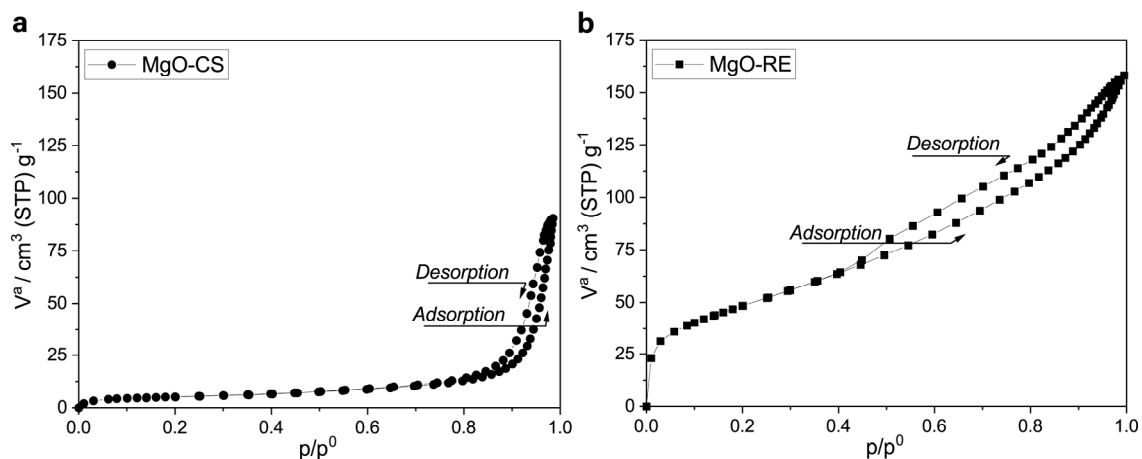
**Figure 3.5:** Experimental adsorption and desorption isotherms of $N_2$ (at 77 K) on the samples of magnesia: (a) MgO-CS, and (b) MgO-RE.
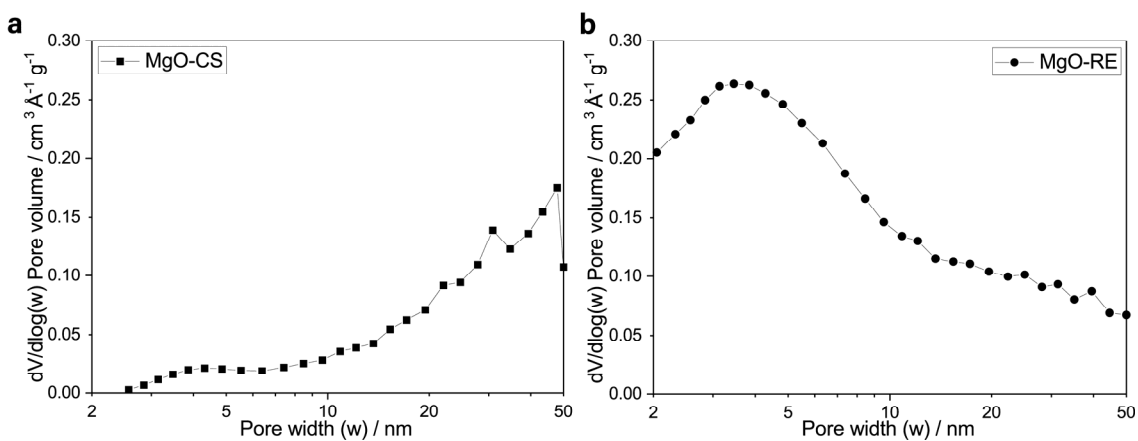


**Figure 3.6:** The BJH pore size distribution obtained for the nitrogen adsorption at 77 K on the samples of magnesia: (a) MgO-CS, and (b) MgO-RE.

**Table 3.8:** BET surface area of magnesia samples.

| Item | MgO-CS | MgO-RE |
|---|---|---|
| BET surface area (m²/kg) | 18.2 | 176.7 |

### 3.3.4 Expansive properties

Fig. 3.7 shows the free shrinkage of mortars containing rapidly expansive magnesia and CEM I at w/c of 0.5 in four curing conditions. Both wet-burlap and water curing conditions (WB and WA samples) resulted in similar expansion in mortars containing MgO-RE. The sample cured in air (NO sample) contracted significantly in the first week. The sample cured in plastic film did not expand nor contracted in the first week. These observations suggest that the water curing, and wet burlap curing provide similarly sufficient curing for the mortars containing MgO-RE to expand in the first week. In contrast, plastic film curing, and air curing are not sufficient for expansion in the samples. There are a number of similarities between Fig. 3.7 and Fig. 3.8. Similar to Fig. 3.7, in mortars containing CEM III, water curing and wet burlap curing provide sufficient curing for expansion in the first week while plastic film curing and air curing do not.

Fig. 3.9 and Fig. 3.10 show the free shrinkage of mortars containing rapidly expansive magnesia at w/c of 0.6 in four curing conditions. The results suggest that the higher water content due to a greater w/c ratio in the samples does not lead to internal curing. Similar to Fig. 3.7 and Fig. 3.8, both plastic film curing and air curing are inadequate. In addition, the higher w/c and larger porosity in the samples slightly increase the samples' expansion. This may be attributed to a more facilitated hydration of magnesia particles by a larger porosity in these samples.
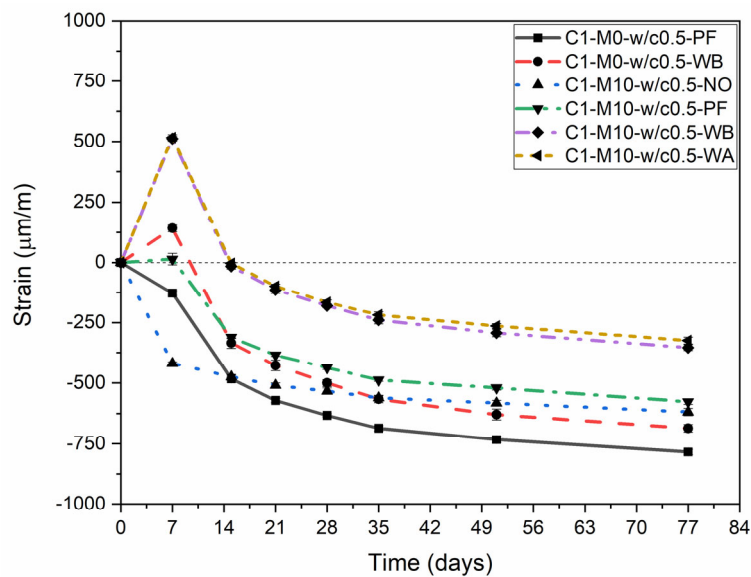


**Figure 3.7:** Free shrinkage of mortars containing rapidly expansive magnesia and CEM I at w/c of 0.5 under various curing conditions.
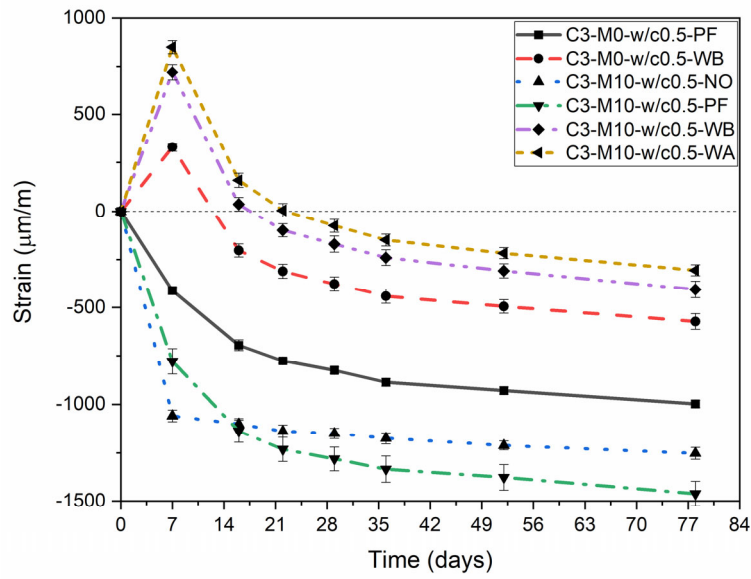
**Figure 3.8:** Free shrinkage of mortars containing rapidly expansive magnesia and CEM III at w/c of 0.5 under various curing conditions.
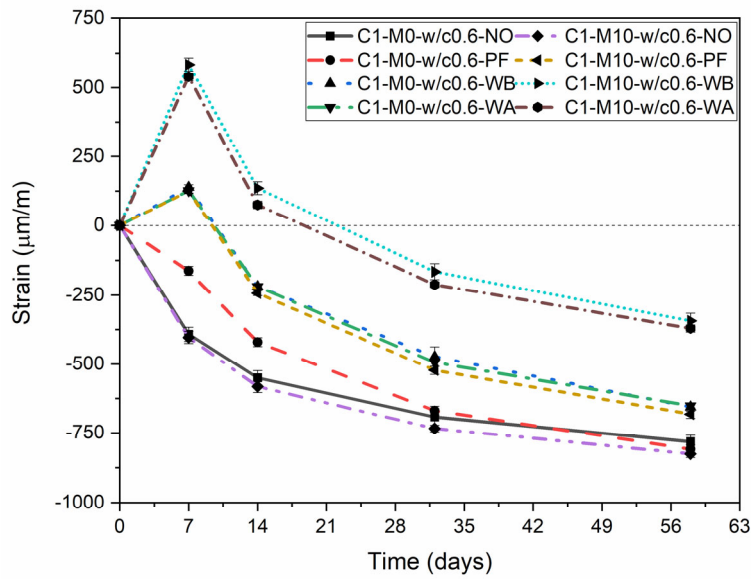


**Figure 3.9:** Free shrinkage of mortars containing rapidly expansive magnesia and CEM I at w/c of 0.6 under various curing conditions.
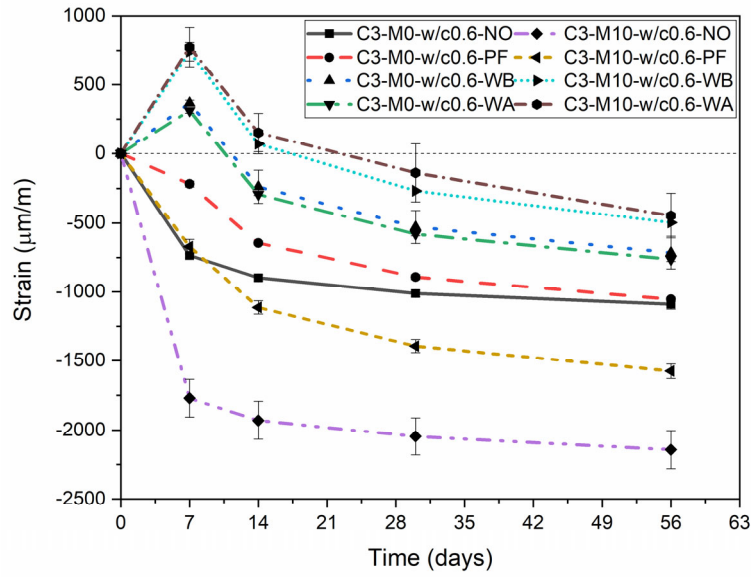
**Figure 3.10:** Free shrinkage of mortars containing rapidly expansive magnesia and CEM III at w/c of 0.6 under various curing conditions.

Fig. 3.11a-b show the linear free shrinkage of concretes containing rapidly expansive magnesia at w/c of 0.55. In order to study the early-age expansion and drying shrinkage in more detail the time in Fig. 3.11c-d is shown in a logarithmic scale. Fig. 3.11c-d show that in concrete samples proportioned with CEM I and CEM III, the expansive influence of MgO-RE starts about seven hours (0.3 day) after starting shrinkage measurements (13 hours after casting). After this period, the samples containing magnesia continue to expand while the reference sample stops expansion. After water curing stops (seven days), the samples start to shrink. The horizontal section of the shrinkage curve of concretes containing CEM I is longer than those containing CEM III. This may be attributed to the slower hydration of CEM III compared to CEM I.

Fig. 3.12a-b show the logarithmic shrinkage of concretes containing rapidly expansive magnesia after seven days. In order to quantify the shrinkage of concrete, commonly a logarithmic model is used [128]

$$e = a + b \cdot \ln(t) \tag{3.6}$$

with $e$ the strain, $a$ the offset from the strain axis, $b$ the slope of the function, and $t$ the time on the horizontal axis. Table 3.9 lists the parameters of logarithmic model for the concrete specimens. All the curves could be well captured by this model ($R^2$ greater than 0.99 for all

except C1-M0 with R$^2$ greater than 0.98). The change in the slope of the fitted models is small and the slopes of the fitted models differ slightly. For example, the slopes of the C3-M0 and C3-M5 are almost equal and only differ 8% from that of the C3-M10 sample. The same trend is observed for CEM I samples, too. Furthermore, the offset from the strain axis depends on the percentage of magnesia in the samples and a higher dosage leads to a higher expansion in the samples.
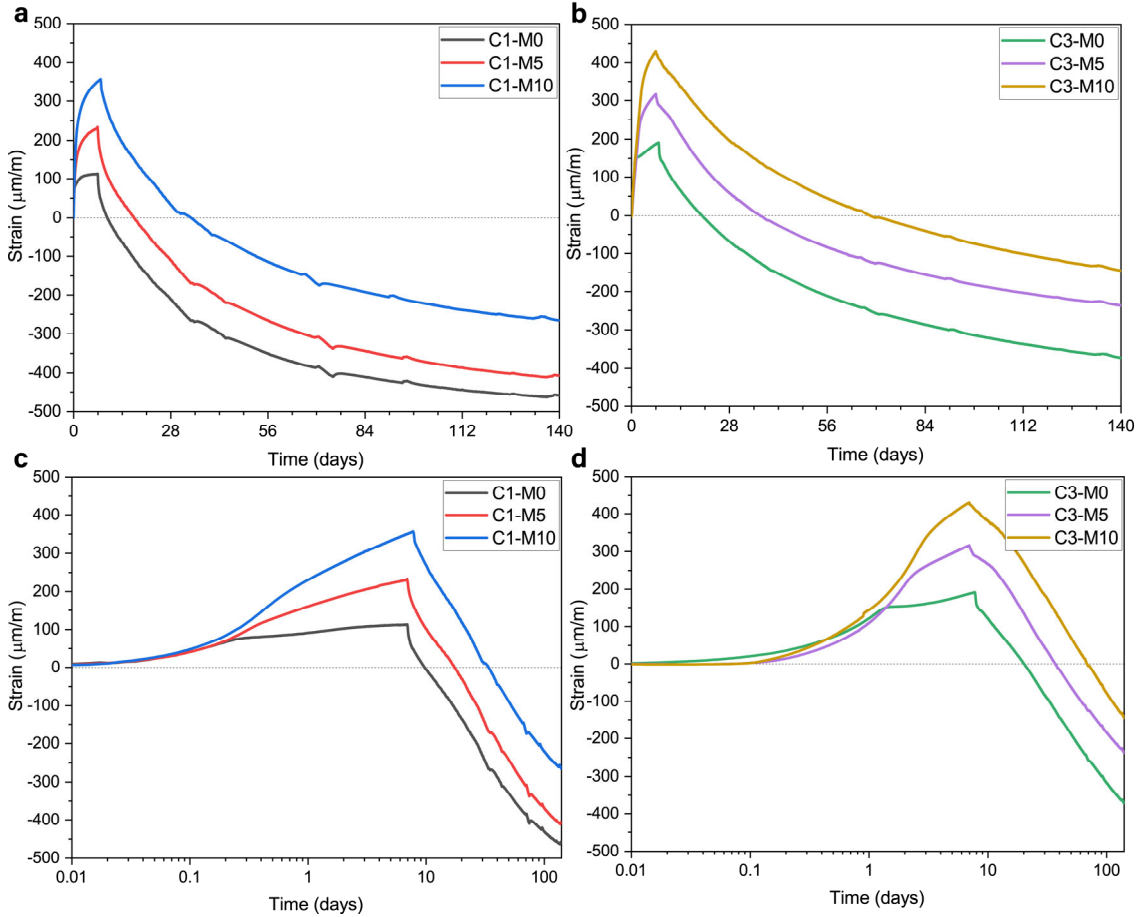


**Figure 3.11:** Free shrinkage of concretes containing rapidly expansive magnesia at w/c of 0.55: (a) linear shrinkage of concrete proportioned with CEM I; (b) linear shrinkage of concrete proportioned with CEM III; (c) logarithmic shrinkage of concrete proportioned with CEM I; (d) logarithmic shrinkage of concrete proportioned with CEM III;
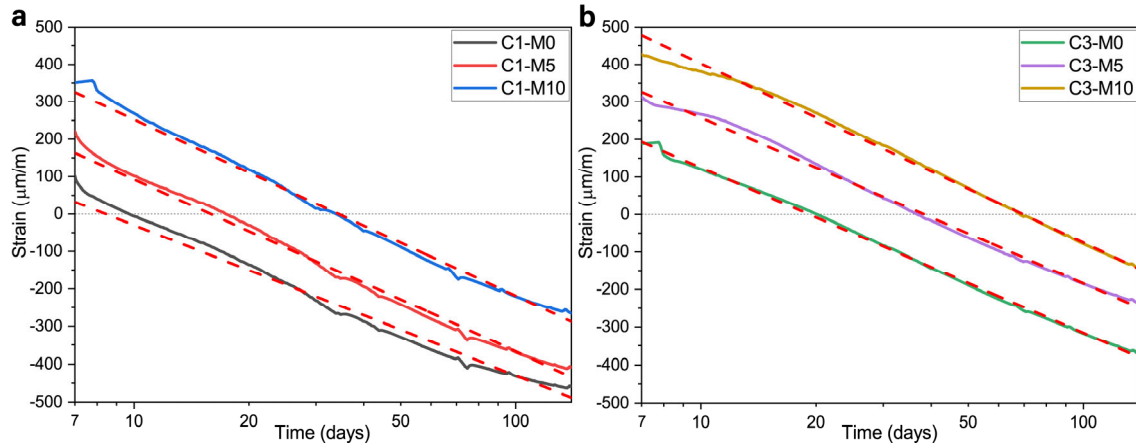
**Figure 3.12:** Logarithmic shrinkage of concretes containing rapidly expansive magnesia after seven days: (a) proportioned with CEM I, and (b) proportioned with CEM III. Dashed lines represent their fits using Eq. 3.6 and the data in Table 3.9.

**Table 3.9:** The parameters of the logarithmic model for the concrete specimens (Eq. 3.6).

| Sample | a | b | $R^2$ |
|---|---|---|---|
| C1-M0 | 369.7 | -173.6 | 0.98 |
| C1-M5 | 550.4 | -199.1 | 0.99 |
| C1-M10 | 723.9 | -204.7 | 0.99 |
| C3-M0 | 565.6 | -191.4 | 0.99 |
| C3-M5 | 700.5 | -192.1 | 0.99 |
| C3-M10 | 880.6 | -207.6 | 0.99 |
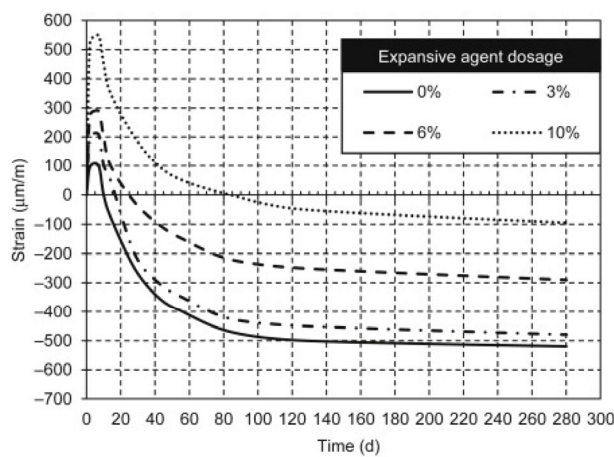


**Figure 3.13:** Free expansion measured using vibrating wire gages for a concrete containing a calcium-oxide based expansive admixture (w/c = 0.72) [129,130].

47

Fig. 3.13 shows the free expansion measured by vibrating wire strain gages in concrete samples containing 10% calcium-oxide based expansive admixture. The expansion of concrete containing 10% rapidly expansive magnesia (see Fig. 3.11) is comparable to that of concrete containing between 6% to 10% CaO-based expansive admixture. It is worth noting that the greater expansive properties of CaO-based admixtures are not due to their superiority over MgO-based admixtures. But it is because this study is the first to investigate the early expansive behavior of magnesia in concrete. The magnesia used in this study was produced for another application and was not "designed" for expansion in concrete. Future investigations on the rapidly expansive magnesia may result in better expansive performance. Our ongoing investigations have shown that certain expansive magnesia produces greater expansion in concrete compared to what was reported in this thesis. The most crucial difference between that highly expansive magnesia and the one used in this thesis is less sintering impurities in the patent solid and better heating conditions to avoid sintering during calcination.

## 3.4    Conclusions

With the purpose of evaluating the performance of rapidly expansive magnesia (MgO-RE) as a shrinkage compensating admixture (SCA), the composition, microstructure, morphology, adsorption isotherm, and pore structure of MgO-RE are compared and contrasted to those of cooling shrinkage magnesia (MgO-CS). The expansive performance of MgO-RE is evaluated in mortar and concrete at two w/c ratios and four curing conditions. The following conclusions can be drawn:

- The expansion and shrinkage of concretes containing MgO-RE are comparable to those of concretes containing expansive calcium-hydroxide based admixtures. The MgO-RE can be regarded as a shrinkage compensating admixture that produces early-age concrete expansion to offset shrinkage.

- MgO-RE has small average crystallite sizes (7.8 nm). It also has a negligible concentration of sintering oxides such as $Fe_2O_3$, $SiO_2$, and $Al_2O_3$ (less than 0.5%). Cooling shrinkage magnesia has large crystallite sizes (21.1 nm) and contains a higher concentration of sintering oxides (higher than 0.5%).

- Water curing and wet burlap provide sufficient curing for expansion in mixtures containing MgO-RE, while plastic film curing and air curing do not. Seven days of water curing is adequate to provide maximum expansion by MgO-RE.

- After seven days of water curing, the shrinkage of concrete samples containing MgO-RE can be well captured with a logarithmic model ($R^2 > 0.98$). The slope of the fitted model in concrete samples containing rapidly expansive magnesia proportioned with CEM I and CEM III is in the same range $-200 \pm 10$.

# Homogeneity and thermal history of light-burnt magnesia by surface properties

*This chapter presents a novel method for homogeneity and thermal history detection in light-burnt magnesia. If inhomogeneity is not detected reliably before application, it causes unpredicted expansion and cracking. The proposed method provides an equation for computing the weighted mesopore probability distribution of light-burnt magnesia (LBM). Then, it deconvolutes the distribution's peaks by Lorentz peak functions to analyze homogeneity. The method's performance is evaluated by examining LBM samples produced by calcining magnesite at four temperatures and walking through several scenarios, including the mixtures of these samples. The results confirmed that the proposed method accurately detects inhomogeneities together with their calcination temperatures and percentages. These findings make it possible to prevent unpredicted expansion in cement composites incorporating expansive magnesia and can be employed to detect inhomogeneities in other porous materials applications.*

## 4.1  Introduction

This chapter presents an accelerated method to analyze the homogeneity and thermal properties of light-burnt magnesia (LBM), the subject of previous chapter (Chapter 3). Magnesia (MgO) is relatively rare in nature and is usually produced by the thermal decomposition of magnesium compounds such as magnesite ($MgCO_3$) [29]. World magnesite mine production was about 28 million metric tons (Mt) in 2020 [131] and the magnesia production industry is projected to grow at a rate of 5% from 2021 to 2031 [132]. Magnesia has a wide variety of applications ranging from manufacturing refractories [133–136], catalysts [137,138], rubber [139], plastic to wastewater treatment [140] and air pollution

control [141]. Existing research recognizes the influence of manufacturing source [142–144], manufacturing method [145–147], manufacturing atmosphere [148], calcination process and sintering [24,31,149–152], calcination kinetics [153], and crystal orientation [154–156] on the properties of magnesia.

Light-burnt magnesia (LBM) is usually produced by calcining magnesite at temperatures lower than 1000 °C. It accounts for one-third of magnesia applications and has high chemical activity [131]. LBM has two major applications in construction industry. Firstly, it is used as an expansive agent to compensate shrinkage of concrete. Carefully calcined LBM acts as an expansive agent and produces expansion at a rate closely matching the long-term shrinkage of concrete to prevent concrete cracking [16]. Secondly, LBM is used as a primary ingredient to produce Sorel cements. More information on the application of LBM in concrete is provided in the recent reviews by Walling and Provis [28], Mo et. al. [119] and Du [120]. It is now well established that variation in the thermal history of LBM, significantly affects the properties of the final application products [30].

Much of the current literature on LBM pays particular attention to the assessment of the average reactivity of LBM. Mo et. al. [23] studied calcination of magnesium oxides and reported the change in porosity and crystal structure of magnesia due to calcination temperature. Harper used iodine number to index reactivity as used by American magnesia industry [31]. Alegret et al. [32] proposed potentiometry to study reactivity of magnesia. Hirota et al. [33] characterized sintering of magnesia by crystallite size, particle size, and morphology. Kim et al. [34] studied the transformation of the crystal structure of $MgCO_3$ and $Mg(OH)_2$ to MgO during calcination. Zhu et al. [35] proposed a corrected MgO hydration convention method for reactivity assessment. Chau et al. [36] introduced an accelerated reactivity assessment method based on the time required for acid neutralization of magnesia. Surprisingly, none of the current LBM reactivity analysis methods can provide information on its thermal history.

The current chapter aims at filling this research gap by studying surface properties to analyze the highly porous structure of LBM formed during calcination. This highly porous structure is thanks to the pseudomorphous calcination of LBM and is identifiable by gas physisorption techniques [157–160]. Here, the nonlocal density functional theory (NLDFT) is used to compute the mesopore size distribution of LBM. NLDFT allows a better explanation of the adsorption and phase transitions in small mesopores, compared to classical Kelvin equation-based methods [124,161]. The proposed method provides an equation that weights this

NLDFT data to compute the weighted mesopore probability distribution and deconvolutes the peaks of the distribution by Lorentz peak functions.

Four LBM samples, calcined at 600 °C, 700 °C, 800 °C, and 900 °C are examined. First, their adsorption mechanisms are studied by analyzing their physisorption isotherms, BET surface areas, C parameters, and alpha-s method. Their pore size distributions are computed by using nonlocal density functional theory (NLDFT). Next, their weighted mesopore probability distributions are computed and curve-fitted by Lorentz peak functions. Then, the weighted mesopore probability distributions of several scenarios, including the mixtures of these LBM samples, are computed. Finally, the distributions are deconvoluted by Lorentz peak functions, and a set of criteria for assessing homogeneity and thermal history of light-burnt magnesia is presented. This study shows how to use surface properties to characterize the thermal history of magnesia which is suitable for the application in the construction field to produce Sorel cements and expansive magnesia.

## 4.2    Experimental

### 4.2.1    Materials

The current investigation involved producing light-burnt magnesia by thermal decomposition of magnesite at 600 °C, 700 °C, 800 °C, and 900 °C. The magnesite was obtained from the company Magnesia (Germany). The calcination was effected in a muffle furnace and the residence time was 24 h to ensure that the influence of residence time on the samples is negligible, and only calcination temperature controls the properties of samples. The calcination temperatures have been indicated in sample designations throughout this chapter. For example, M600 refers to the sample calcined at 600 °C. Fig. 4.1 demonstrates the mineral crystalline phases of the samples, measured by X-ray Diffraction (XRD). The diffraction patterns were obtained using a Bruker ENDEAVOR diffractometer, equipped with a Co-radiation source, divergence slit (0.5°), soller slit (0.04 rad), and Lynxeye detector. The main crystalline phase of the samples is periclase. The main peak of periclase was utilized to compare the crystal grain sizes of the samples, using the Scherrer equation [123]. The periclase crystallites in M700, M800, and M900 were 1.28, 1.68, and 1.93 times as big as those in M600, respectively.

In addition, four mixtures of LBM were prepared to investigate the applicability of the studied methods in characterizing their homogeneity. Table 4.1 shows the composition of these mixtures.

**Table 4.1:** The composition of LBM mixtures (in weight percent).

| Item | M600 | M800 | M900 |
|---|---|---|---|
| M600(50%)+M800(50%) | 50% | 50% | 0 |
| M600(80%)+M800(20%) | 80% | 20% | 0 |
| M600(50%)+M900(50%) | 50% | 0 | 50% |
| M600(80%)+M900(20%) | 80% | 0 | 20% |
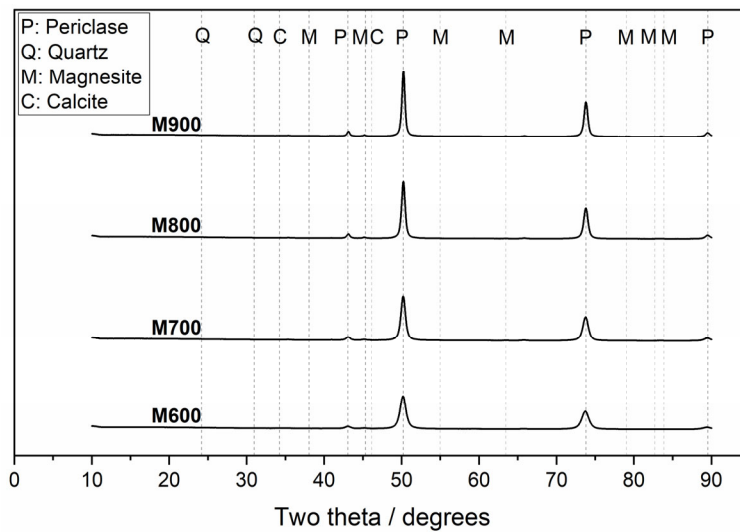


**Figure 4.1:** The mineral crystalline phases of the samples, measured by XRD (P: periclase, Q: quartz, M: magnesite, C: calcite).

## 4.2.2 Methodology

*Adsorption mechanism*

Before measuring physisorption isotherms, possible contaminants on the surface of the samples were removed by a combination of heat (120 °C) and flowing nitrogen gas for four hours. When weighing the samples, a sample quantity that yields at least 10 m² was prepared for good precision. This amount ensured reasonable pressure difference thanks to sufficient gas adsorption by the adsorbent at each step [125].

After sample preparation, adsorption and desorption isotherms were measured at 77 K using a Micromeritics TriStar II analyzer. The adsorption isotherms were plotted using [124]

$$\frac{V^a}{m^s} = f\left(\frac{p}{p^0}\right) T \tag{4.1}$$

with $V^a$ the amount of adsorbate, $m^s$ the mass of solid, $p$ the actual adsorbing gas pressure, $p^0$ the saturation pressure of the adsorbing gas at $T$, and $T$ the thermodynamic temperature [124]. Point B was shown on the measured physisorption isotherms as the point where the adsorption isotherms become linear [162].

In order to obtain the BET surface area, the linear transformed BET equation was used by the formula [124]

$$\frac{p}{V^a(p^0\text{-}p)} = \frac{1}{V_m C} + \frac{C-1}{V_m C}\frac{p}{p^0} \tag{4.2}$$

with $V^a$ the amount of adsorbed gas at the equilibrium pressure $p$, $V_m$ the monolayer capacity, $C$ a constant, and $p$ and $p^0$ as used previously [124]. From Eq. (4.2), a plot of $\frac{p}{V^a(p^0\text{-}p)}$ versus $\frac{p}{p^0}$ was made to obtain a straight line with intercept $\frac{1}{V_m C}$ and slope $\frac{C-1}{V_m C}$ to calculate the values of $V_m$ and $C$. The BET specific surface area then was calculated by [124]

$$a_{BET} = \frac{V_m \sigma L}{m^s V_0} \tag{4.3}$$

with $\sigma$ the mean molecular cross-sectional area (0.163 nm$^2$ for nitrogen molecule), $L$ the Avogadro constant (6.02214 × 10$^{23}$ mol$^{-1}$), $m^s$ the mass of adsorbing sample, $V_0$ the gas molar volume (22414 cm$^3$), and $V_m$ as used previously.

To obtain the surface area by $a_s$ curve, the standard data of a nonporous specimen were obtained from [163]. Next, the $a_s$ of the reference data was obtained from [162]

$$a_s = \frac{V_{ref}^a}{V_{ref}^{0.4}} \tag{4.4}$$

with $V_{ref}^a$ the amount of adsorbate in the standard data, and $V_{ref}^{0.4}$ the amount of adsorbate at the pre-selected relative pressure of 0.4 in the standard data.

Then, the $a_s$ curve of the sample was constructed by specifying at similar relative pressures the value of $\alpha_s$ of the standard data and the value of $V^a$ of the sample. Finally, a plot of $V^a$ versus $a_s$ was made to yield the $a_s$ curve.

The surface area of samples was calculated from the $a_s$ curve by [162]

$$a_{\alpha_s} = \frac{s_{test}}{s_{ref}} \cdot a_{BET}^{ref} \tag{4.5}$$

with $a_{\alpha_s}$ the calculated surface area of samples from the $a_s$ curve, $a_{BET}^{ref}$ the BET surface area of standard data, $s_{test}$ the slope of the $a_s$ plot of the test material, and $s_{ref}$ the slope of the $a_s$ plot of the standard data.

*Pore structure*

A complete mesopore size distribution was computed by the nonlocal density functional theory (NLDFT) method. In the NLDFT method, the pore size distribution was obtained by [124]

$$N_{exp}\left(\frac{p}{p^0}\right) = \int_{w_{min}}^{w_{max}} N_{theo}\left(\frac{p}{p^0}, w\right) f(w) \mathrm{d}w \tag{4.6}$$

with $N_{exp}\left(\frac{p}{p^0}\right)$ the measured number of adsorbed molecules and $N_{theo}$ the kernel of theoretical isotherms in model pores [124]. The computation procedure for pore size distribution by the NLDFT method can be found in Rouquerol et al. [124]. The NLDFT computations were done with a kernel, based on nitrogen adsorption at 77K on graphitic carbon having slit-shaped pores, using the Tristar 3020 analysis program.

## 4.3    Results and discussion

### 4.3.1    Adsorption mechanism

The physisorption isotherms of the samples are displayed in Fig. 4.2. Each graph consists of adsorption and desorption isotherms. All the adsorption isotherms are initially concave, then become linear, and finally convex to the $\frac{p}{p^0}$ axis. All the desorption isotherms do not retrace the adsorption isotherms and create hysteresis loops. The hysteresis loops occur

owing to the intrinsic difference between the curvature of the liquid surface of condensate, from which the desorption occurs, and nucleation on the solid pore walls, from which multilayer adsorption and condensation starts [125]. This curvature hampers evaporation from the liquid surface, and therefore, the desorption isotherm falls behind the adsorption isotherm and leads to a hysteresis loop [125].
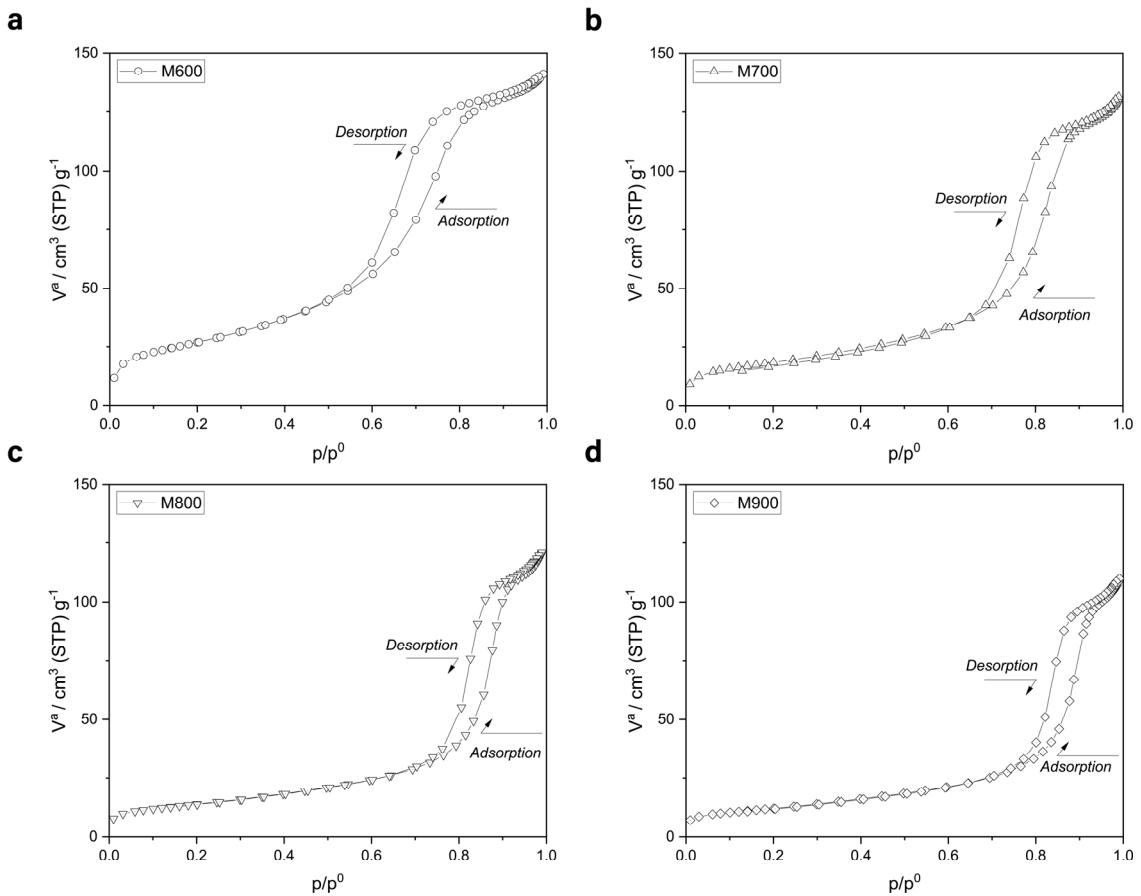


**Figure 4.2:** Experimental adsorption and desorption isotherms of $N_2$ (at 77 K) on the LBM samples: (a) M600; (b) M700; (c) M800, and (d) M900.

According to IUPAC recommendations, the general form of physisorption isotherms classifies adsorbents into six types [126]. Based on the measured physisorption data, all the four magnesia preparations belong to a Type IV-a class. Type IV isotherms initiate similar to Type II isotherms but have a characteristic plateau at higher relative pressures. They are a characteristic of mesoporous materials [124].

Fig. 4.3 illustrates the constitutive parts of Eq. (4.2) for calculating the BET surface area. The selected range of linearity of the BET plot was within the relative pressures of 0.05 to

0.2, according to [162]. All the preparations were well captured by the linear transformed BET model ($R^2 > 0.99$). As mentioned earlier, the y-intercept and the slope of the lines in Fig. 4.3 were used to calculate the monolayer capacity and C parameter from Eq. (4.2) and Eq. (4.3).
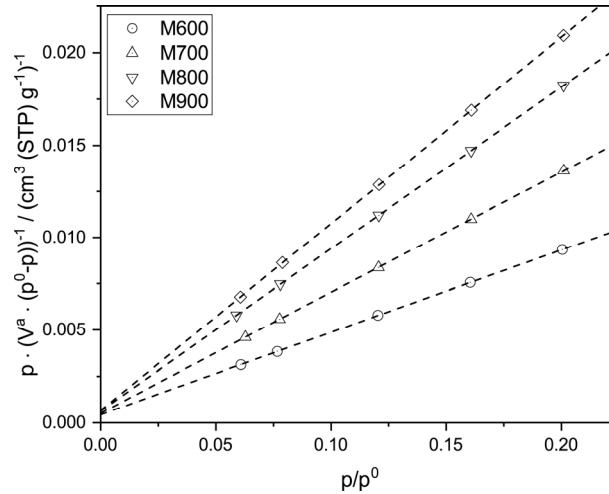


**Figure 4.3:** BET plots of the LBM samples. The dashed lines represent the linear regression of the data.

Table 4.2 compares and contrasts the BET surface area ($a_{BET}$) and *C* parameter of the samples. The BET surface area decreases with increasing calcination temperature. The parameter *C* provides useful information about the shape of the isotherm in the BET range. If the parameter *C* is less than 2, the competition between the gas-solid affinity and gas-gas affinity makes the BET method inapplicable [126]. On the other hand, a parameter C higher than 150 indicates high energy sites on the surface of micropores [126]. The beginning of the linear section of the adsorption isotherm indicates the monolayer completion and is usually referred to as Point B [126]. A parameter C of at least 80 indicates a rather explicit Point B [124,126]. The C parameter of M900 is just over 150, but as shown in Fig. 4.4, the monolayer capacity and Point B were in substantial agreement. The parameter *C* of the samples remains in the range of 80 to 150, Point B is demonstrable as a single point, and the value of monolayer capacity ($V_m$) is validated.

**Table 4.2:** BET surface area and C parameter of magnesia samples.

| Item | M600 | M700 | M800 | M900 |
|------|------|------|------|------|
| BET surface area ($a_{BET}$) [m²g⁻¹] | 97.0 | 66.2 | 49.3 | 42.9 |
| C parameter | 103.9 | 130 | 140 | 152 |

The first half of the adsorption isotherms of Fig. 4.2 are illustrated in Fig. 4.4. High energy sites on the surface of the samples cause the initial steep rise in the isotherms. This steep rise diminishes as the high-energy sites are covered. As predicted from the value of parameter *C*, the monolayer capacities of the samples ($V_m$), represented by horizontal dashed lines, are in substantial agreement with point B of the samples.
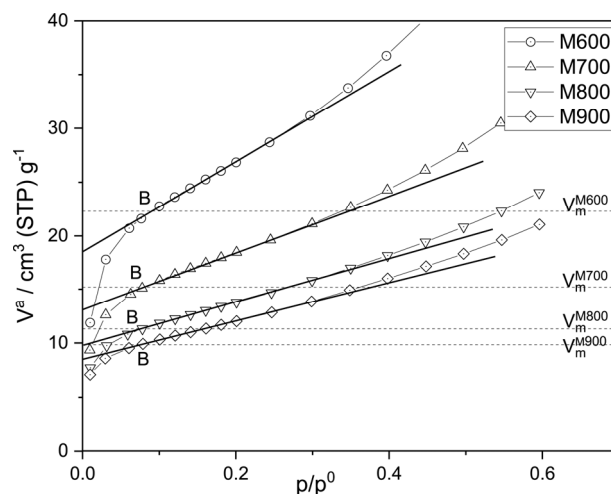


**Figure 4.4:** Monolayer capacity (represented by dashed lines) and the Point B (represented by a point at the start of the linear section of adsorption isotherms) of the LBM samples.

Fig. 4.5 shows the $\alpha_s$ plots of the samples. Inspection of these plots is instructive as there is a linear section in all the curves their back-extrapolation gives near-zero intercept ($R^2 > 0.999$ for the first eight points of each preparation). Zero intercept in $\alpha_s$ curves is an indication of a non-microporous sample. The upward deviation from the linear section in the curves is due to capillary condensation [124]. The calculated surface area of the samples ($a_{\alpha s}$) was determined by incorporating the slopes of these linear sections into Eq. (4.5). The results of this calculation are listed in Table 4.3.
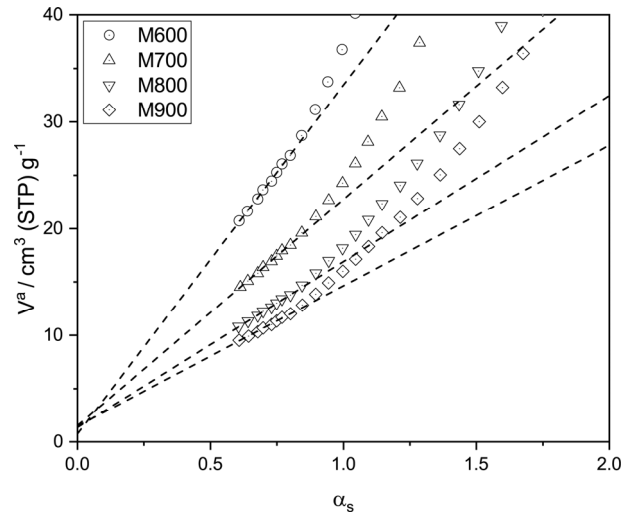
**Figure 4.5:** $\propto_s$ plots of the LBM samples. The dashed lines represent the back-extrapolation of the linear sections.

The $\propto_s$ curves give an independent evaluation of the total available surface area in a mesoporous material or the external area in a microporous material [124]. Table 4.3 compares and contrasts the surface area ($a_{\propto S}$), calculated from the physisorption isotherms and $\alpha_s$ plots, with the BET surface area. The small difference between the values of $a_{\propto S}$ and $a_{BET}$ in the samples suggests that almost all the surface area in the samples is external and that the adsorption mechanism is mainly governed by mesopores.

**Table 4.3:** Comparison of the calculated surface area from α_s plots with the BET surface area.

| Item | M600 | M700 | M800 | M900 |
|---|---|---|---|---|
| Surface area from $\alpha_s$ plots ($a_{\propto S}$) [m²g⁻¹] | 94.2 | 61.1 | 44.8 | 37.9 |
| BET surface area ($a_{BET}$) [m²g⁻¹] | 97.0 | 66.2 | 49.3 | 42.9 |

## 4.3.2 Pore structure

As outlined earlier in the Introduction, the nonlocal density functional theory (NLDFT) is implemented to compute the mesopore size distribution of LBM samples. The mesopore size distribution is [164]

$$I(w_i) = \delta V_i \tag{4.7}$$

with $\delta V_i$ the i-th mesopore volume increment, and $I(w_i)$ the mesopore size distribution. As can be seen in Fig. 4.6, on the whole, all the samples are highly mesoporous. This is explained by the pseudomorphous calcination of magnesite, in which magnesia retains the external shape and volume of magnesite [165,166] and is consistent with the studied adsorption mechanisms in the previous section. It is also apparent that the distributions shift to the right at higher calcination temperatures, and their peaks become smaller. The change in the pore structure of the samples at higher calcination temperatures is due to shrinkage and sintering [165,166] and is in line with the previously discussed change in the physisorption isotherms and surface area.

The cumulative mesopore size distribution of the samples is expressed by the sum of the mesopore volume increments in the form [164]

$$C(w_i) = \sum \delta V_i \tag{4.8}$$

with $C(w_i)$ the cumulative mesopore size distribution and $\delta V_i$ as used previously. As illustrated by Fig. 4.7, the pore structure alteration caused by shrinkage and sintering causes the total mesopore volume to decrease at higher calcination temperatures. It is also evident that the median mesopore width of the distribution shifts to the right at higher calcination temperatures.

In order to use the shift of the distributions in Fig. 4.6 and Fig. 4.7 to characterize the homogeneity of the samples, inspecting the probability density functions (PDFs) is constructive. The mesopore probability distribution of the samples is [164]

$$P(w_i) = V_{tot,m}^{-1} \cdot \frac{\delta V_i}{\delta w_i} \tag{4.9}$$

with $V_{tot,m}$ the total mesopore volume, $\delta w_i$ the i-th pore width increment, $P(w_i)$ the mesopore probability distribution (probability density function), and $\delta V_i$ as used previously.
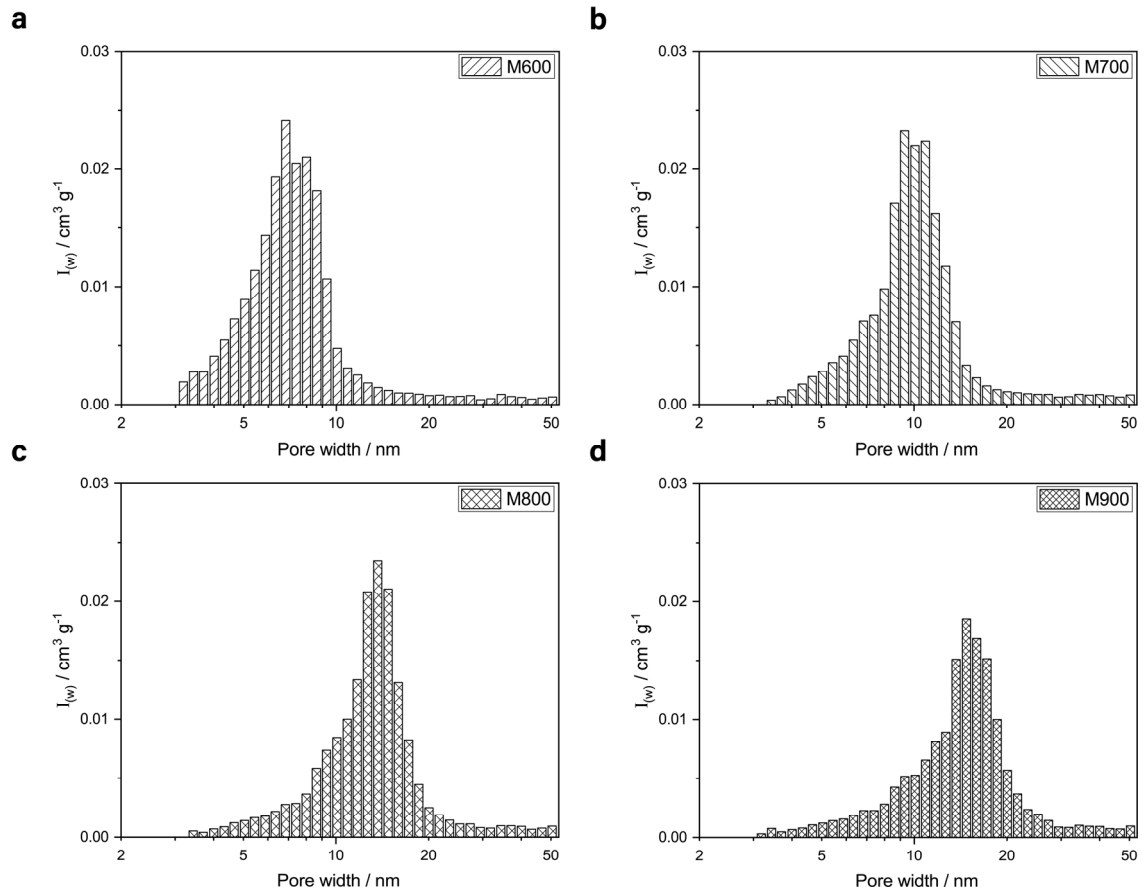
**Figure 4.6:** Mesopore size distributions of the LBM samples, computed by Eq. 4.7: (a) M600; (b) M700; (c) M800, and (d) M900.
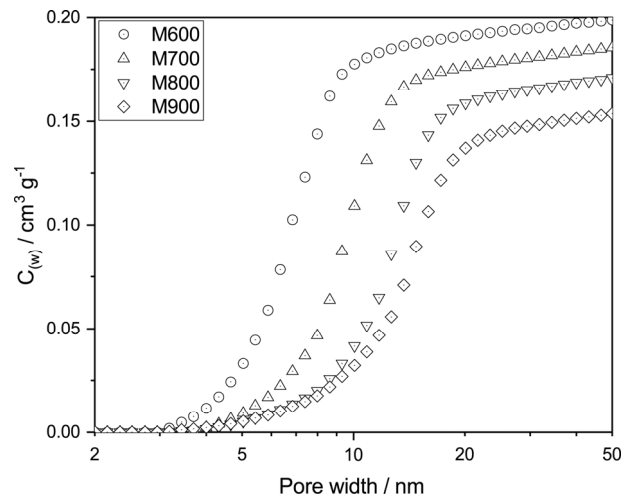


**Figure 4.7:** Cumulative mesopore size distributions of the LBM samples, computed by Eq. 4.8.
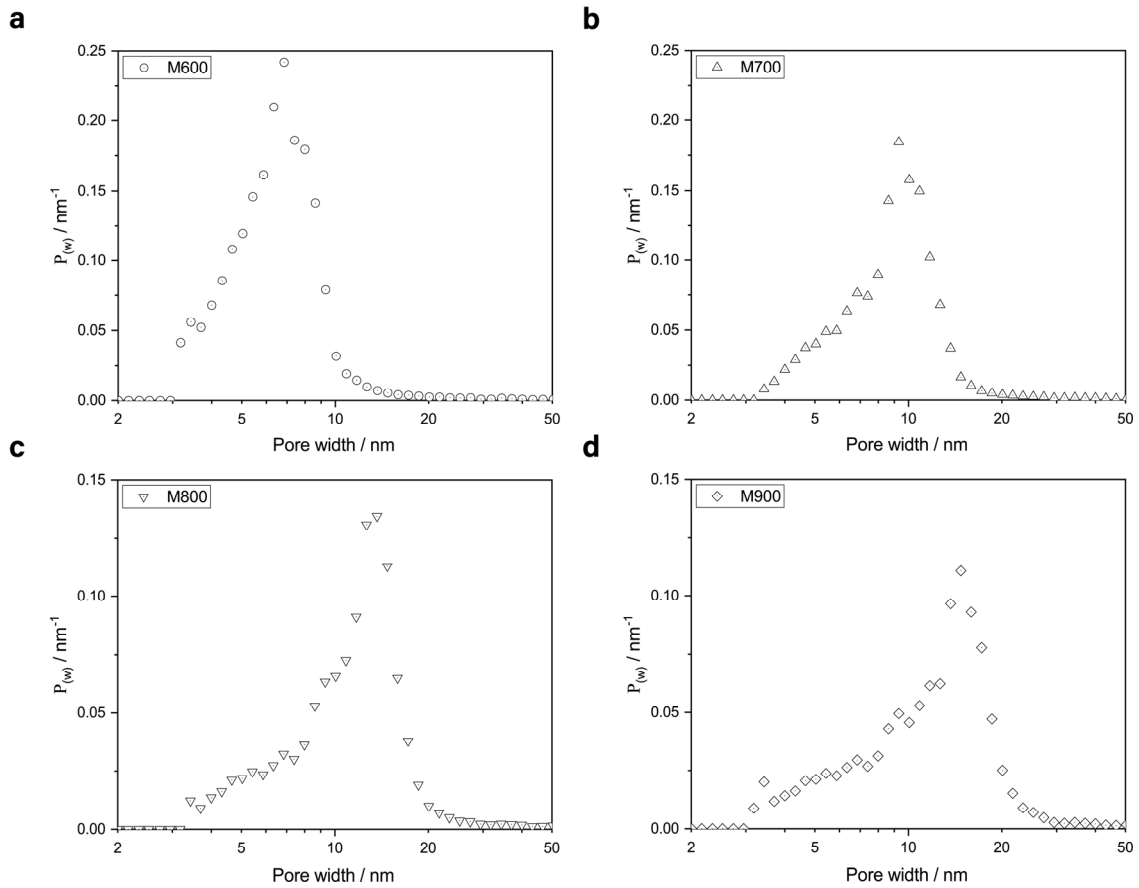
**Figure 4.8:** Mesopore probability distributions of the LBM samples, computed by Eq. 4.9: (a) M600; (b) M700; (c) M800, and (d) M900.

The mesopore probability distribution of the samples is reported in Fig. 4.8. The shift in the distribution peaks at different calcination temperatures can be used to form a hypothesis that, similar to the phase quantification in X-ray powder diffraction, convolution-based profile fitting can be utilized to analyze the homogeneity of the samples. Unlike XRD profiles, there is only one peak in the mesopore probability distributions of the samples. Furthermore, the peaks shorten at higher calcination temperatures and make convolution-based profile fitting less accurate. To overcome this issue, the distributions need to be weighted with a weighting factor. This weighting factor should give higher weights to distributions of higher calcination temperatures. As distribution peaks of the higher calcination temperatures occur at wider pore widths, this study proposes to choose a factor of the pore width ($\ln 10 \cdot w_i$) as the weighting factor.

The weighted mesopore probability distribution is [164]

$$L(w_i) = 2.3 \, P(w_i) \cdot w_i \tag{4.10}$$

or

$$L(w_i) = 2.3 \, V_{tot,m}^{-1} \cdot \frac{\delta V_i}{\delta w_i} \cdot w_i \tag{4.11}$$

with $L(w_i)$ the weighted mesopore probability distribution, $w_i$, $P(w)$, $V_{tot,m}$, and $\delta V_i$ as defined previously. Since $2.3 \frac{\delta V_i}{\delta w_i} \cdot w_i$ in Eq. (4.11) is replaceable with $\frac{\delta V_i}{\delta \log(w_i)}$ the proposed equation for weighted mesopore probability distribution, in simplified terms, is

$$L(w_i) = V_{tot,m}^{-1} \cdot \frac{\delta V_i}{\delta \log(w_i)} \tag{4.12}$$

As illustrated by Fig. 4.9, the weighted mesopore probability distributions' peak heights are almost equal (~4). This facilitates identifying hidden peaks by deconvolution in inhomogeneous samples. The dashed lines represent the best Lorentz fit to the data. The Lorentz peak function usually is written

$$y = y_0 + \frac{2A}{\pi} \cdot \frac{W}{[4(x - x_c)^2 + W^2]} \tag{4.13}$$

with $y_0$ the offset from the y-axis, $A$ the area of the function, $W$ the full width at half maximum (FWHM), and $x_c$ the center of the function. All the distributions could be well captured by this function (adjusted $R^2$ greater than 0.99).

The Lorentz peak functions' parameters, namely center, FWHM, and area, are compared and contrasted in Fig. 4.10. On the whole, all the parameters increase with the increase in the calcination temperature. For example, the centers of the functions in M600 and M700 are at 7.3 nm and 10.3 nm, respectively, and move to 13.7 nm and 15.4 nm in M800 and M900. The same trend holds true for the area of the functions at different temperatures, as well. Later in this chapter, the center of these Lorentz fits is used to indicate the calcination temperature of fractions in inhomogeneous samples, and the area of the Lorentz fits is employed to calculate the weight percentages of these fractions.
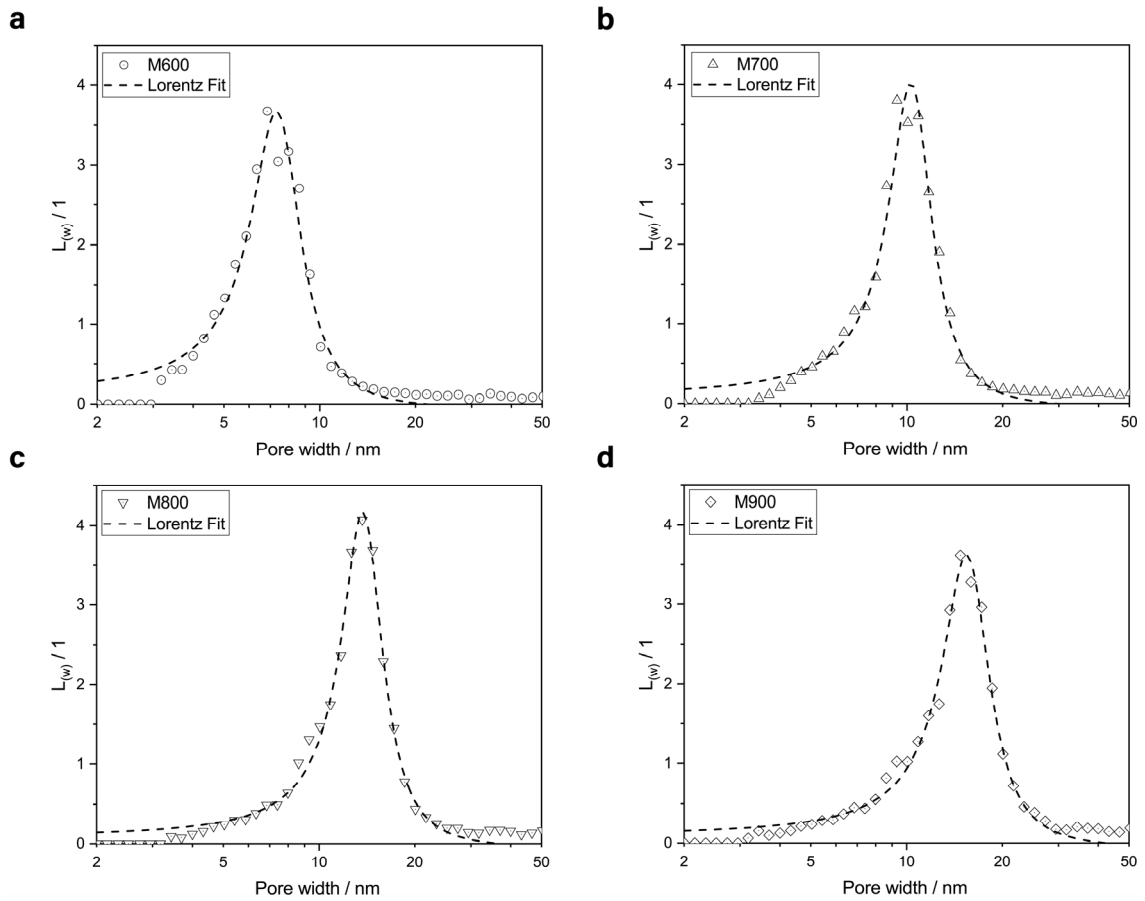
**Figure 4.9:** Weighted mesopore probability distributions of the LBM samples (demonstrated by symbols) and their Lorentz fits (demonstrated by dashed lines), computed by Eq. 4.12: (a) M600; (b) M700; (c) M800, and (d) M900.
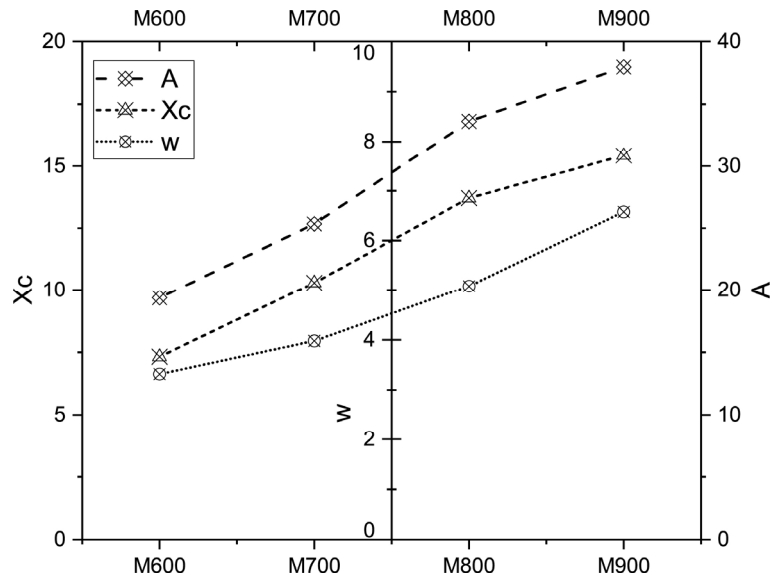


**Figure 4.10:** Parameters of the Lorentz peak functions, taken from Fig. 4.9. (A: the area of the function, W: the full width at half maximum (FWHM), and Xc: the center of the function).

To verify the methodology, Fig. 4.11 shows the weighted mesopore probability distribution of the LBM mixtures. The percentage of LBM fractions has been indicated in the mixture designations. For example, M600(50%)+M900(50%) is a mixture consisting of 50% M600 and 50% M900. The dashed and dotted lines represent the best Lorentz fits to the data. All the distributions were well captured by the cumulative fits (adjusted $R^2$ greater than 0.94).

The centers of the Lorentz fits of Fig. 4.11 are demonstrated in Fig. 4.12. The horizontal dashed lines represent the centers of the Lorentz peak functions used for deconvoluting the weighted mesopore probability distributions of unmixed magnesia preparations in Fig. 4.9. It is evident that the centers of cumulative Lorentz fits are almost identical to those of pure LBMs. For example, the centers of the Lorentz fits in both M600(50%)+M900(50%) and M600(80%)+M900(20%) compare well with the centers of pure M600 (7.3 nm) and M900 (15.4 nm). As another example, the centers of the Lorentz fits in both M600(50%)+M800(50%) and M600(80%)+M800(20%) compare well with the centers of pure M600 (7.3 nm) and M800 (13.7 nm), as well. These results provide evidence that deconvoluting the weighted mesopore probability distribution of light-burnt magnesia by Lorentz peak functions is a robust method to analyze homogeneity.

The percentage of each fraction in LBM mixtures is

$$\text{Fraction i (\%)} = \frac{\dfrac{A^{cumulative}_{Fraction\ i}}{A^{pure}_{Fraction\ i}}}{\sum_{j=1}^{N} \dfrac{A^{cumulative}_{Fraction\ j}}{A^{pure}_{Fraction\ j}}} \tag{4.14}$$

where $A^{cumulative}_{Fraction\ i}$ is the area of the i-th Lorentz fit in the cumulative fit (captured from Fig. 4.11) and $A^{pure}_{Fraction\ i}$ the area of the i-th Lorentz fit in its pure form (captured from Fig. 4.10).

Table 4.4 lists the computed percentage of each fraction in LBM mixtures. It is evident that the predicted percentages are in excellent agreement with real values. In addition, these results confirm that the proposed method quantifies the homogeneity of LBM.
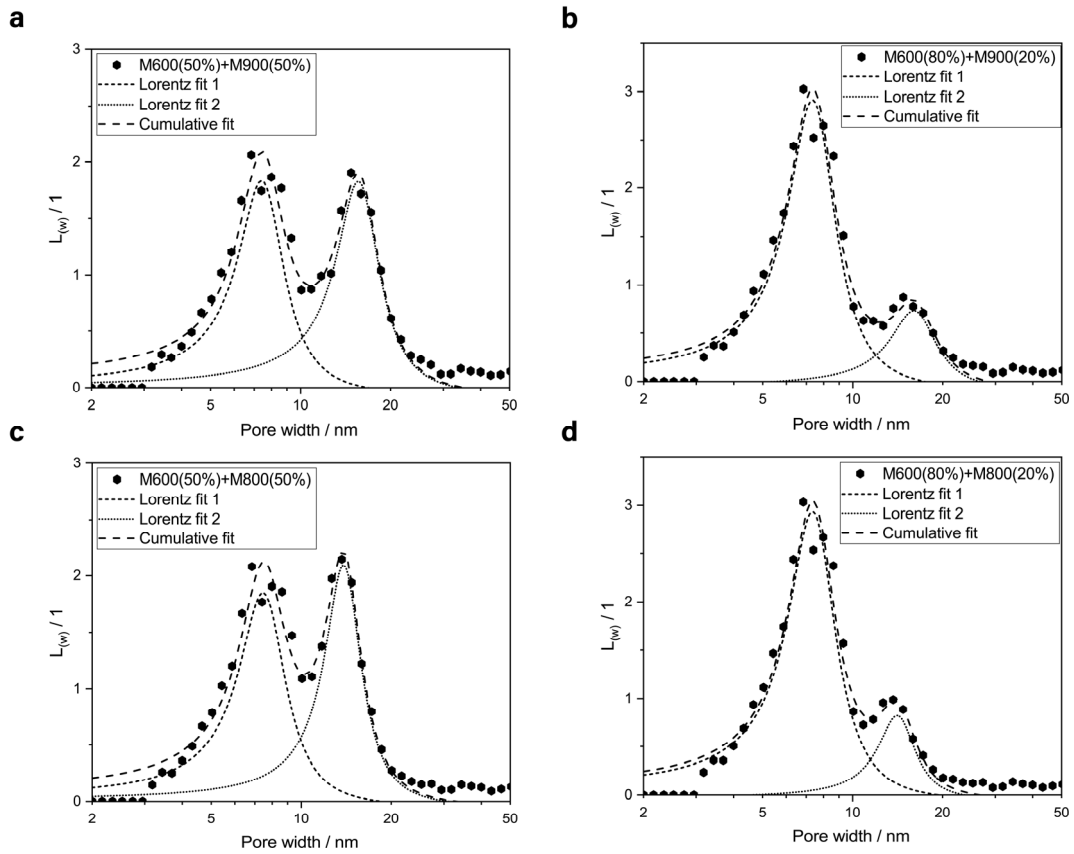
**Figure 4.11:** Weighted mesopore probability distributions of magnesia mixtures and their Lorentz fits: (a) M600(50%)+M900(50%); (b) M600(80%)+M900(20%); (c) M600(50%)+M800(50%), and (d) M600(80%)+M800(20%).
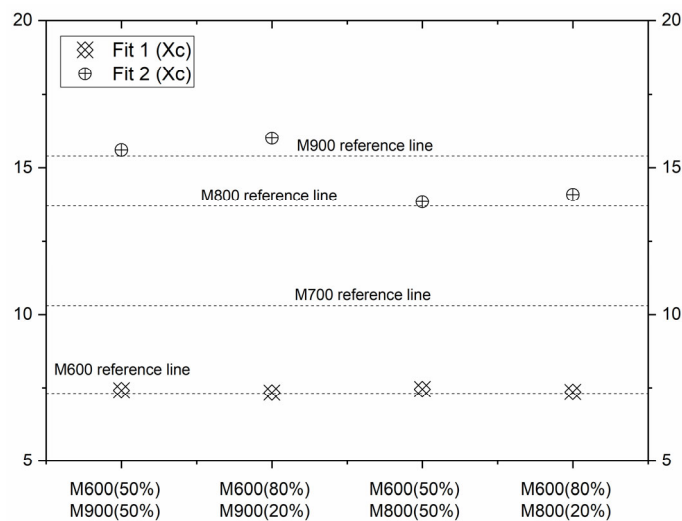


**Figure 4.12:** Center of the Lorentz peak functions used for deconvoluting weighted mesopore probability distributions of magnesia mixtures in Fig. 4.11. Horizontal dashed lines represent the centers of the Lorentz peak functions used for deconvoluting the weighted mesopore probability distributions of unmixed magnesia preparations in Fig. 4.9.

**Table 4.4:** Computed composition of magnesia mixtures versus actual composition.

| Mixture | M600(50%) M900(50%) | M600(80%) M900(20%) | M600(50%) M800(50%) | M600(80%) M800(20%) |
|---|---|---|---|---|
| Computed composition (fraction 1) | 49.9% | 77.5% | 51.5% | 81.6% |
| Computed composition (fraction 2) | 50.1% | 22.5% | 48.5% | 18.4% |

The mixtures of M600 and M700 were not studied in this thesis since the inhomogeneity caused by a large temperature gap (say M600 and M900 or M600 and M800) is more critical than one caused by a small temperature gap (say M600 and M700). When the temperature gap is short, the peaks of the weighted mesopore probability distribution are close. This may not affect the accuracy of the deconvolution method at high inhomogeneity dosages (say 50% M600 plus 50% M700). However, it may reduce its accuracy at lower inhomogeneity concentrations (say 80% M600 plus 20% M700), see also Table 4.4.

This study indicates the benefits of deconvoluting the weighted mesopore probability distribution by Lorentz peak functions to analyze the homogeneity of light-burnt magnesia. The proposed method is a cost-effective detection tool that avoids cracking in concrete structures by detecting inhomogeneities in light-burnt magnesia. As the pseudomorphous structure of calcined magnesia provides the foundation of this method, the proposed method can be applied to a wide range of pseudomorphous materials to detect inhomogeneities, as well.

However, some limitations are worth noting. This study only analyzed the light-burnt magnesia produced by calcining magnesite. The magnesia produced by calcining other magnesium compounds such as brucite has a different pore structure [34]. Furthermore, the presence of some gases, such as water vapor, may significantly influence the structure of calcination products [160]. In addition, the presence of impurities in the parent solid may promote sintering [24]. Further research may therefore include the influence of parent solid, impurities in the parent solid, and the calcination atmosphere to provide calibration curves for the method presented here.

## 4.4    Conclusions

In this chapter, a new technique for identifying and quantifying the homogeneity and heat treatment history of light-burnt magnesia (LBM) produced from the calcination of magnesite is reported. The method provides equations (i.e., Eqs. 4.12 and 4.14) for computing the weighted mesopore probability distribution of LBM and analyzing the peaks present in the distribution to examine homogeneity. The properties of each peak are calculated by deconvoluting the distribution by Lorentz peak functions and reiterating peak deconvolution using the Levenberg Marquardt algorithm. Based on the results obtained, the following conclusions can be drawn:

- The proposed method identifies and quantifies the homogeneity and heat treatment history of light-burnt magnesia produced from the calcination of magnesite.
- The method identifies homogeneity by giving the number of fractions from the number of peaks in the weighted mesopore probability distribution.
- The method identifies the calcination temperature of each fraction from the center of the Lorentz fit of that fraction in the weighted mesopore probability distribution.
- The method provides the possibility to derive the composition of LBM mixtures using the area of their Lorentz fits in the weighted mesopore probability distribution.

# Milled paper pulp to modify rheological behavior

*In this chapter, the performance of paper pulp as an innovative viscosity modifying admixture (VMA) for cement composites is reported. Two different levels of fineness were obtained by mechanical milling of the same source of paper pulp. Their effects on viscosity modification, hydration kinetics, autogenous shrinkage, and compressive strength of cement grouts were measured, and their structural integrity at high pH was assessed. A new parameter was proposed to quantify nonlinearity induced by VMAs. Results showed that the hierarchical structure of paper pulp makes it possible to activate bridging flocculation and swelling mechanisms of hydrophile paper pulp fibers at different levels to produce versatile VMAs. The coarser milled paper pulp fibers mainly influence the plastic viscosity. By contrast, the milled paper pulp consisting of ultra-fine fibers significantly modifies both plastic viscosity and dynamic yield stress, induced more nonlinearity in the mixtures, and increases compressive strength of mortars at low dosages.*

## 5.1 Introduction

Paper pulp is attracting widespread interest in different fields thanks to its high volume, environmental-friendly origin, and potential economic profits. It has helped the paper industry to maintain its high rank among recycling industries as a combination of recycled and virgin pulp leads to suitable paper quality [37]. Nonetheless, digitization has caused less demand for paper pulp, especially in Europe and North America [38]. This reduction has resulted in initiating endeavors to transform the paper industry and find other ways to valorize paper pulp. So far, the valorization methods have been limited to applications such as manufacturing fibrous insulation in buildings [39], producing bitumen thickener in asphalt [39], or producing energy by incineration [39,40]. In a quest for a desirable industry for

valorization, the cement and concrete industry would be a right candidate, because of both enormous volume produced worldwide annually (4.1 and 25 billion tons for cement and concrete, respectively [167,168]) and the big admixture market (estimated to be $38 billion by 2024 [169]).

**Table 5.1:** An overview of the research on applying wood-based pulp in cement composites.

| Authors | Recipe | | Properties tested | |
| | Binder | Fibril types | Pulp % | Application |
| --- | --- | --- | --- | --- |
| Correia et al. 2018 [41] | OPC* | Bamboo pulp + CNF‡ | 8% | Reinforcement of extruded cement paste |
| Campello et al. 2016 [42] | OPC* | Bamboo pulp | 6% | Reinforcement of cementitious composites |
| Khorami et al. 2016 [45] | OPC* | Waste kraft pulp | 8% | Asbestos replacement in fiber cement board |
| Shokrieh et al. 2015 [51] | OPC* + Bentonite | PVA† + Cellulose pulp | 3% to 7.5% | Reinforcement of cement composite sheets |
| Ballesteros et al. 2015 [53] | OPC* | Pine and eucalyptus pulp | 5% | Reinforcement in cementitious matrices |
| Claramunt et al. 2015 [52] | OPC* | Conventional pulp + Nanofibrillated pulp | 8% | Reinforcement in cement mortars |
| Hosseinpourpia et al. 2014 [59] | OPC* | Waste sulfite pulp | 5% to 15% | Reinforcement in cementitious composites |
| Tonoli et al. 2013 [46] | OPC* | Isocyanate-treated eucalyptus kraft pulp | 5% | Reinforcement in cement composites |
| Khorami & Ganjian 2013 [47] | OPC* | Kraft pulp | 1-14 % | Flexural improvement of cement composites |
| Mármol et al. 2013 [56] | OPC* + Gypsum | Softwood pulp (Pinus) | 9% | Reinforcement in cementitious composites |
| Jongvisuttisun et. al. 2012 [60] | OPC* | Eucalyptus pulp | 7.5% to 15% | Internal curing |
| Mezencevova et al. 2012 [61] | OPC* | Thermomechanical pulp (TMP) | 5% | Internal curing |
| Tonoli et al. 2010 [54] | OPC* | Eucalyptus pulp | 5% | Reinforcement of cementitious materials |
| Tonoli et al. 2010 [55] | OPC* | Eucalyptus and pine kraft pulp | 10% | Reinforcement of cement composites |
| Mohr et al. 2007 [48] | OPC* + Pozzolans | Kraft pulp | 4% | Reinforced cement-based materials |
| El-Ashkar et al. 2007 [49] | OPC* | Kraft pulp | 1.2% and 2% | Reinforced cement mortars |
| Tonoli et al. 2007 [57] | OPC* | Sisal pulp | 4.7% | Reinforced cement composites |
| Rodrigues et al. 2006 [43] | OPC* + Pozzolan | Bamboo pulp | 8% | Reinforced cement composites |
| Mohr et al. 2006 [50] | OPC* | Kraft pulp | 4% | Reinforced cement composite |
| Savastano Jr. et al. 2003 [58] | OPC* and BFS✷ | Sisal pulp | 8% | Reinforced cement |
| Coutts et al. 1994 [44] | OPC* | Bamboo pulp | 10% | Reinforced cement composite |

* Ordinary Portland Cement; ‡ Cellulose Nano Fiber; ✷ Blast Furnace Slag; † Polyvinyl alcohol.

Currently, as detailed in Table 5.1, one way to valorize wood-based pulp is to incorporate it as a reinforcing agent in cement composites. For example, there has been extensive research on applying bamboo pulp [41–44], kraft pulp [45–50], cellulose pulp [51,52], pine and

eucalyptus pulp [53–55], pinus pulp [56], sisal pulp [57,58], and waste pulp [59] in cement composites as a reinforcement. Another way to valorize wood-based pulp is to utilize it as an internal curing agent for cement composites [60,61]. Pulp dosages of up to 15% weight of cementitious materials have been reported for both applications. However, little attention has been paid to hierarchical and hydrophilic characteristics of the wood-based pulp as a route to make highly effective concrete additives.

As shown in Fig. 5.1, the paper pulp has a hierarchical structure [170] in which macro fibers consist of microfibers where the latter are also made up of nanofibers. Such a hierarchical structure and hydrophilic properties can be used to form a hypothesis that different levels of fineness of the same source of paper pulp would be obtained by mechanical milling, resulting in exposing and spreading hydrophilic fibers at different levels of the hierarchy to produce various highly effective versatile VMAs. VMAs are usually water-soluble natural, semi-synthetic, or synthetic admixtures used to adjust the rheological behavior of cement composites [171]. Their application includes a wide variety of uses such as self-consolidating concrete [75], under-water concrete [172], Ultra-high performance concrete (UHPC) [173–175], cement asphalt mixtures [176], pumpable concrete and shotcrete [177,178], oil-well concrete [179] and 3D printing concrete [180]. Different VMAs have various effects on the rheological behavior of cement composites. Hence, characterizing the added value of a new source of VMA is of vital importance.



(a): Cell wall
(b): Macro fiber
(c): Microfiber
(d): Nanofiber
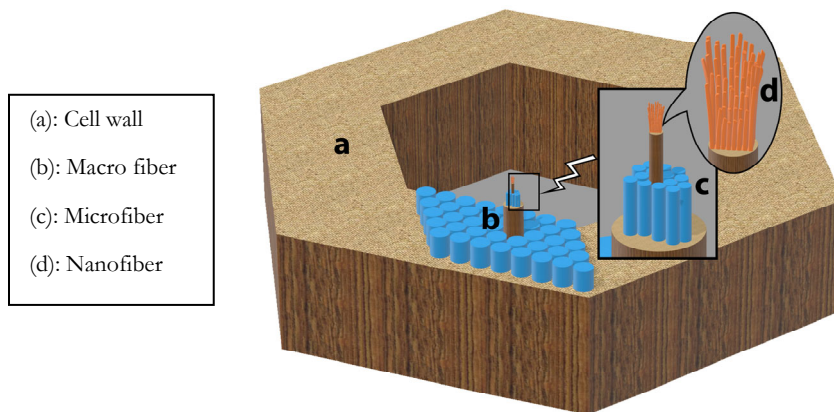
**Figure 5.1:** The schematic hierarchical arrangement of fibers in paper pulp.

This chapter examines milled paper pulp as an innovative viscosity modifying admixture for cement composites. Milled paper pulp differs from most polymeric VMAs in that in the first place, it is not water-soluble. In the second place, it has two pivotal geometric parameters, namely the diameter and length of fibers. Insolubility in water makes the size and

morphology of milled paper pulp significantly influential on the rheological adjustment performance. These characteristics would be used to manufacture versatile VMAs with different levels of viscosity-modifying properties. Besides, in addition to the rheological behavior, several substantial hardened properties of cement composites such as hydration kinetics, shrinkage, and strength rely strongly on water. Consequently, the hydrophile milled paper pulp might also affect these hardened characteristics. Furthermore, cement composites have a highly alkaline environment that might affect the structural integrity of milled paper pulp at an early age.

This chapter aims at filling these research gaps by a methodological approach that begins with manufacturing and characterizing milled paper pulp at two different fineness. Next, the influence of fineness of paper pulp on the rheological properties of cement composites is characterized by different rheological models and compared to those of two commercially available VMAs, namely diutan gum and MasterMatrix. Then, the effects of the fineness of milled paper pulp on the hydration kinetics and autogenous shrinkage of cement composites are studied. Additionally, the stability of milled paper pulp at high pH is evaluated by calcium hydroxide treatment. Finally, Welch's ANOVA and Games-Howell post hoc tests are utilized to investigate the influences of milled paper pulp fineness on the compressive and flexural strengths of cement mortars.

## 5.2    Experimental

### 5.2.1    Materials

The current investigation involved analyzing the influences of fineness of paper pulp on the fresh and hardened properties of cement grouts. Milled paper pulp was manufactured at two different fineness by mechanical milling of the same source of paper pulp at different energy levels at Sappi (the Netherlands) and is referred to as low-energy milled paper pulp (LPP) and high-energy milled paper pulp (HPP) in this study. In order to characterize the fiber length characteristics after processing, according to ISO 16065:2 [181], a Lorentzen & Wettre Online Fiber Tester device was utilized. This device reports fiber size distribution by classifying it into three types of course, fine, and ultra-fine fibers, based on the range of their dimensions, as illustrated in Fig. 5.2 and listed below:

- Coarse fibers: (length > 200 μm);
- Fine fibers: (length > 100 μm) OR (length < 100 μm AND width + 0.35 · length > 50)

- Ultra-fine fibers: (length < 100 µm AND width + 0.35 · length < 50)
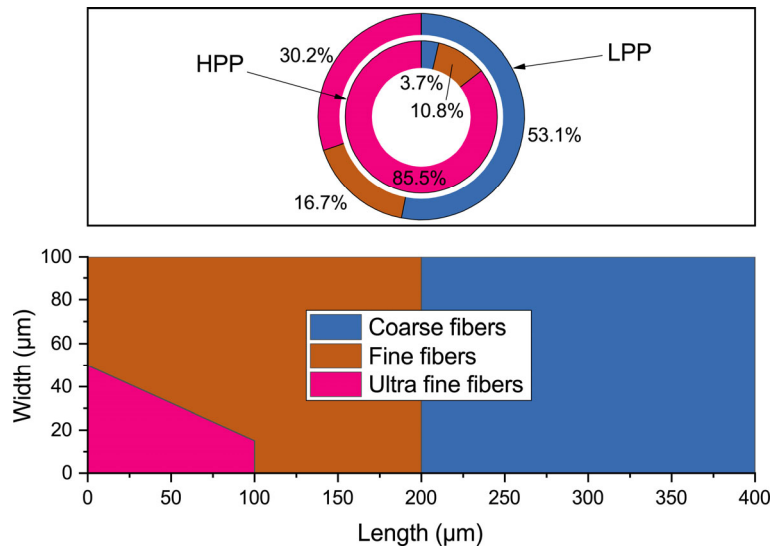


**Figure 5.2:** Fiber length characteristics of LPP and HPP after processing: (below) the definition of ultra-fine, fine, and coarse fibers in Lorentzen & Wettre Online Fiber Tester device analysis; (above) Average weight percentages of different fiber dimensions in LPP and HPP, measured and classified by the same device.

The data in Fig. 5.2 suggest that more than half of the low-energy milled paper pulp (LPP) consisted of coarse fibers, whereas around 85% of the high-energy milled paper pulp was made up of ultra-fine fibers. Mid-range fine fibers constituted 10.8% and 16.7% of LPP and HPP, respectively. It should be pointed out that LPP and HPP were prepared as aqueous suspensions at concentrations of 3% and 1%, respectively. As a consequence, the amount of free water was compensated in all mixture calculations.
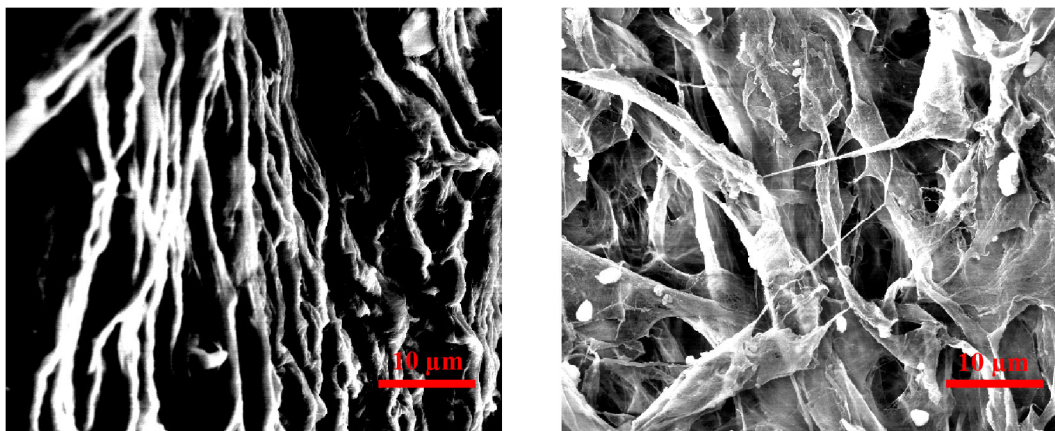


**Figure 5.3:** The micrographs of milled paper pulp at different fineness: (left) LPP; (right) HPP.

Fig. 5.3 highlights the size and morphology differences between LPP and HPP in the vicinity of cement particles. Both of the samples were freeze-dried and scanned by a Phenom Pharos Desktop SEM from Thermo Fisher Scientific at a scale close to the median particle size of the cement utilized in this study (14 μm). The LPP consisted of fibrils of micro-size containing integrated filaments. Conversely, in HPP, microfibers were opened and flattened because of high mechanical energy, and nanofibers were exposed and spread in planes. These SEM observations are in line with the data obtained from the L&W Fiber Tester analysis in Fig. 5.2, as both observations confirmed higher percentages of ultra-fines in HPP. The cement CEM I 52.5 R, provided by ENCI (the Netherlands), was used to compare and contrast the viscosity modifying performance of LPP and HPP in cement grouts. The CEM I 52.5 R is an ordinary Portland cement with a high specific surface area (Blaine of ca. 527 $m^2$/kg [104]) and early strength (30 MPa at one day [104]). It is appropriate for applications like shotcreting and grouting. The chemical composition of CEM I 52.5 R, identified by X-Ray Fluorescence and its particle size distribution, measured by Malvern Mastersizer 2000 particle size analyzer are detailed in Fig. 5.4.
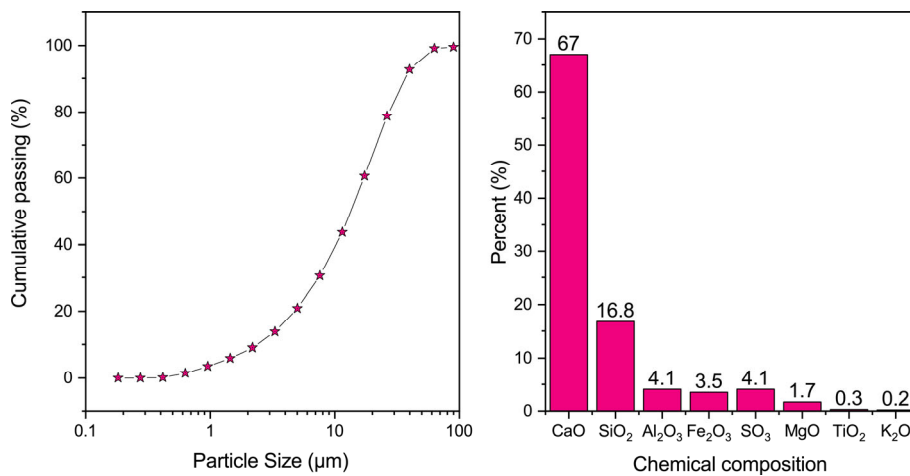


**Figure 5.4:** Physical and chemical properties of the cement CEM I 52.5R: (left) Cumulative particle size distribution; (right) chemical composition (in weight percent).

A polycarboxylic ether-based superplasticizer (SP) with a solid content of 35% was utilized to disperse cement particles. The dosage of SP was calculated as the ratio of the weight of its solids to that of the binder. Neat cement grout, with no VMA, was prepared and used as the reference mixture (REF) in the study. Two commercially available high-performance VMAs, diutan gum and MasterMatrix DSC 100 (MM), were used to investigate the rheology adjustment performance of LPP and HPP. The MasterMatrix DSC 100, manufactured by

BASF, was an aqueous solution of a high-molecular-weight synthetic copolymer with a recommended dosage between 0.1 % to 1.0 % by weight of the binder, by the manufacturer.

## 5.2.2 Methodology

*Effects of milled paper pulp fineness on rheological behavior*

A high shear mixing procedure was used to prepare all the cement grouts to not only study grouts but also provide a paste with comparable rheological properties to that of concrete from which aggregates had been removed [182]. The mixing procedure started with mixing cement with water, SP, and VMA in a double-wall mixing bowl connected to a bath thermostat at 800 rpm for 1 min at 23 °C. Then, the mixer was stopped and scraped with a spatula for 30 s. Next, the mixer was started at 2000 rpm, and the materials were mixed for another 2 min. After stopping the mixer and scraping the bowl for 30 s, the mixing was continued at the same angular velocity for 1 min. Finally, cement grouts were placed in the rheometer, and ten minutes after the cement came into contact with water, the rheometer was started to study the flow behavior. The rheometer was an Anton Paar 501 device equipped with a Peltier plate temperature control system to keep the temperature steady at 23 °C in all the experiments. A concentric cylinder geometry consisting of a serrated bob and cup was used to avoid wall slip. All the samples were preconditioned for one minute with a shear rate of 50 s$^{-1}$ before starting the measurements. Subsequently, a shear rate sweep was performed that consisted of six one-minute steps at shear rates of 100 s$^{-1}$, 80 s$^{-1}$, 60 s$^{-1}$, 40 s$^{-1}$, 20 s$^{-1}$ and 10 s$^{-1}$, respectively. In view of the fact that cement grouts showed thixotropic behavior, the shear stresses at the end of each one-minute step were recorded and used in rheological models. The recipes of the grout mixtures are shown in Table 5.2.

As mentioned before, the superplasticizer (SP), HPP, and LPP were aqueous suspensions at the concentrations of 35%, 3%, and 1%, respectively. For the reason that the amount of free water was compensated in all the mixtures, the dosages shown in Table 5.2 present the dosage of their solids. In other words, LPP and HPP at their maximum dosage of 0.12% in Table 5.2, were aqueous suspensions at the dosages of 4% and 12% of cement weight, respectively. These dosages were selected based on both our previous studies [183] and technical literature [179,184]. Another reason for opting for these dosages was to test similar dosages of LPP and HPP with those of diutan gum and the maximum recommended dosage of MasterMatrix.

**Table 5.2:** Recipe of cement grouts modified with different viscosity modifying admixtures, namely MasterMatrix, diutan gum, LPP, and HPP. The dosages of SP, diutan gum, LPP, and HPP are shown as the ratio of the weight of solids to that of the cement. The dosage of MasterMatrix is demonstrated as the weight of the liquid synthetic copolymer to that of the cement.

| Mix | w/c | SP dosage (%) | MasterMatrix dosage (%) | Diutan gum dosage (%) | LPP dosage (%) | HPP dosage (%) |
|---|---|---|---|---|---|---|
| REF | 0.4 | 0.175% | 0 | 0 | 0 | 0 |
| MM5 | 0.4 | 0.175% | 0.5% | 0 | 0 | 0 |
| MM10 | 0.4 | 0.175% | 1.0% | 0 | 0 | 0 |
| D4 | 0.4 | 0.175% | 0 | 0.04% | 0 | 0 |
| D8 | 0.4 | 0.175% | 0 | 0.08% | 0 | 0 |
| D12 | 0.4 | 0.175% | 0 | 0.12% | 0 | 0 |
| LPP4 | 0.4 | 0.175% | 0 | 0 | 0.04% | 0 |
| LPP8 | 0.4 | 0.175% | 0 | 0 | 0.08% | 0 |
| LPP12 | 0.4 | 0.175% | 0 | 0 | 0.12% | 0 |
| HPP4 | 0.4 | 0.175% | 0 | 0 | 0 | 0.04% |
| HPP8 | 0.4 | 0.175% | 0 | 0 | 0 | 0.08% |
| HPP12 | 0.4 | 0.175% | 0 | 0 | 0 | 0.12% |

In order to quantify viscosity-modifying performances of VMAs, the Bingham model (BM) and Herschel-Bulkley model (HBM) were used. The Bingham model is expressed as [86]

$$\sigma = \sigma_D + \eta_B \dot{\gamma} \tag{5.1}$$

with $\sigma$ the shear stress, $\sigma_D$ the dynamic yield stress, $\eta_B$ the plastic viscosity, and $\dot{\gamma}$ the shear rate. This model is widely used to describe the rheological behavior of cementitious materials [185] and can be employed to characterize the viscosity modifying influence of VMAs.

The Herschel-Bulkley model is a combination of the Bingham and power-law models and has the form [86]

$$\sigma = \sigma_0 + K \dot{\gamma}^n \tag{5.2}$$

with $\sigma_0$ the yield stress of this model, $K$ the consistency factor, $n$ the flow index, and $\sigma$ and $\dot{\gamma}$ as used previously.

*Effects of milled paper pulp fineness on hydration kinetics*

The hydration kinetics of the cement grouts were measured using a TAM Air isothermal calorimeter, according to ASTM C1679 [186]. First, all the samples were mixed externally

and were transferred into glass ampoules and sealed. Then, they were loaded into the calorimeter to measure the heat flow for seven days, with a set temperature of 20 °C. The hydration kinetics results were evaluated by comparing the graphs of normalized thermal power as a function of time, according to ASTM C1679 [186]. The mixtures REF, D8, LPP8, HPP8, and MM10 of Table 5.2, were utilized in hydration kinetics studies, with the mere difference that superplasticizer dosages in all the samples were raised from 0.175% to 0.28% (i.e., the dosage of the aqueous solution of superplasticizer was raised from 0.5 to 0.8) to ease inserting grouts into the ampoules.

*Effects of milled paper pulp fineness on shrinkage*

The autogenous shrinkage of cement grouts was measured according to ASTM C1698 [187] to investigate the water stabilization performance of the studied additives and possible influences on volume change of the cement composites. This standard test method utilizes a dilatometer bench to measure the length change of corrugated tubes, filled with grouts under constant temperature. Three replicate samples were made, and the measurements started after the final setting time of the grouts. The final setting time was determined, according to ASTM C191 [188]. The corrugated plastic tubes had a length of 420 ± 5 mm and an outer diameter of 29 ± 0.5 mm. All the samples and measurement devices were stored in a climate chamber with a temperature of 23 ± 1 °C. Similar mixtures as those used in hydration kinetics studies were utilized for autogenous shrinkage experiments.

*Simulated aging of milled paper pulp*

In order to simulate the highly alkaline environment of the binder, a saturated solution of calcium hydroxide ($Ca(OH)_2$) with a pH of 12.4 was prepared. Then, HPP and LPP were added to the solution and stored for 20 days. Next, the samples were dried in a freeze dryer (Alpha 1 – 4 LD plus from Christ) using the following settings:

- Ice condenser = -57 °C
- vacuum < 1 bar
- $t = 48$ h

Finally, a Perkin Elmer Frontier Fourier Transform Infrared Spectrometer (FTIR) equipped with a GladiATR diffuse reflectance (ATR) module was used to record the spectra of the freeze-dried samples before and after simulated aging. Eight scans were acquired with optical retardation of 0.25 cm and a resolution of 4 cm$^{-1}$ from the wavelength of 400 to 4000 cm$^{-1}$.

It should be noticed that in ATR mode, the absolute value of the area of a peak cannot be used for quantitative analysis as this method only characterizes the surface of the sample. However, a significant reduction of a peak can indicate a structural change.

*Effects of milled paper pulp fineness on compressive and flexural strengths*

Early-age flexural and compressive strengths were assessed to evaluate the possible crack-bridging and reinforcement by the fibers. All the standard mortar samples (water:cement:sand = 1:2:6) were prepared using a Hobart mixer, according to EN 196-1:2016 [44]. Cement, water, SP, and VMA were mixed at low speed (140 ± 5 rpm) for one minute. Next, the mixer was switched to high speed (285 ± 10 rpm), and mixing was continued for another 30 s. The mixer was stopped, and its walls were scraped for 30 s. Finally, after mixing for another 60 s at high speed (285 ± 10 rpm), the mortars were poured in prism specimens, $40 \times 40 \times 160$ mm$^3$. The specimens were unmolded 24 h after casting and were cured in water at about 21 °C before the tests. Tap water was used for curing to keep conditions as similar as possible to concrete in practice. The flexural and compressive strengths of the specimens were measured using 50 N/s and 2400 N/s as the test speeds, respectively. One-way Welch's Analysis of Variance (ANOVA) was used to evaluate the effect of VMAs on the mechanical properties of mortars. The analysis was evaluated at 5% significance level ($\alpha$), considering the equality of all means as the null hypothesis (Ho) and the non-equality of all means as the alternative hypothesis (Ha). Furthermore, Games-Howell post hoc tests were used to compare the mean differences between pairs of VMAs at different ages.

## 5.3    Results analysis

### 5.3.1    Effects of milled paper pulp fineness on rheological behavior

As mentioned previously, the flow behavior of the grouts was characterized by two rheological models, namely the Bingham model and the Herschel-Bulkley model. The rheological data and Bingham fits of the grouts are demonstrated in Fig. 5.5. In general, all the viscosity-modifying admixtures increase the shear stress at similar shear rates, compared to the reference. The more the dosage of the VMA, the higher the value of the shear stress. Furthermore, the range of shear stress of the grouts containing MasterMatrix and LPP is comparable to each other ($\sigma < 40$). Similarly, although the shear stress in grouts incorporating HPP or diutan gum is several times higher than that in grouts having LPP and

MasterMatrix (MM) at similar shear rates, the range of shear stress of the former grouts is comparable to each other ($\sigma < 250$).
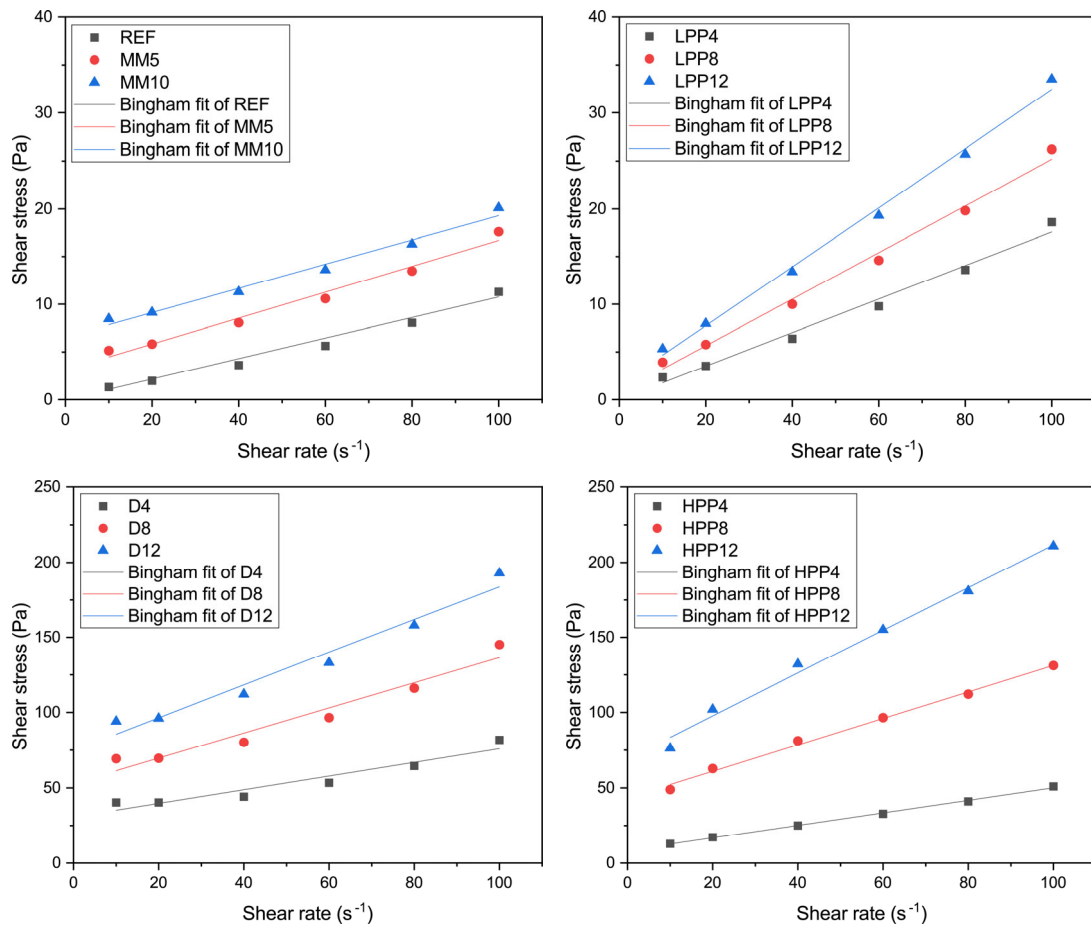


**Figure 5.5:** Rheological data and Bingham fits of grouts with different viscosity-modifying admixtures (REF: reference; MM: MasterMatrix; D: diutan gum; LPP: Low-energy milled paper pulp, and HPP: High-energy milled paper pulp).
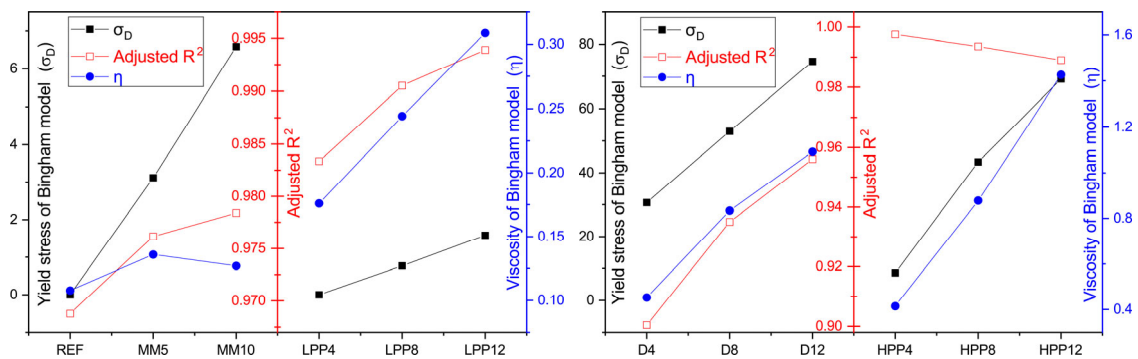


**Figure 5.6:** The Bingham model parameters of grouts with different viscosity-modifying admixtures (REF: reference; MM: MasterMatrix; D: diutan gum; LPP: Low-energy milled paper pulp, and HPP: High-energy milled paper pulp).

In order to quantify these differences and similarities, the parameters of the Bingham model, namely dynamic yield stress and plastic viscosity, together with adjusted $R^2$ of the fittings, are compared and contrasted in Fig. 5.6. As the range of the parameters of LPP and HPP grouts is close to those of MasterMatrix and diutan gum grouts, respectively, the rheological parameters of LPP grouts are paired with those of MM grouts. In contrast, the rheological parameters of HPP grouts are paired with those of the diutan gum grouts.

The values of the adjusted $R^2$ of the Bingham models for REF, LPP, and MM are more than 0.97, which show a strong correlation. Adding LPP to cement grouts, increases the dynamic yield stress and plastic viscosity. The values of the plastic viscosity of LPP grouts at the dosages of 0.08% and 0.12% are higher than those of the MM mixtures at half maximum (0.5%) and maximum (1%) dosages, respectively. Besides, LPP increases the yield stress less than the synthetic copolymer (MM).

Furthermore, the finer milled paper pulp (HPP) increases both yield stress and plastic viscosity more than LPP. The effect of HPP on rheological behavior is comparable to that of diutan gum. However, HPP increases the plastic viscosity more than diutan gum and enhances the yield stress less than diutan gum at similar dosages. It should also be noted that the value of adjusted $R^2$ falls to 0.9 in the Bingham fittings of the diutan gum grouts, which can be interpreted as an indicator of nonlinear behavior. In order to elucidate these nonlinearities, the Herschel-Bulkley fits of the rheological data are demonstrated in Fig. 5.7. All the flow curves could be well-described by this model (Adjusted $R^2 > 0.99$). The parameters of the Herschel-Bulkley fits of the grouts, namely yield stress, flow index, and consistency factor are compared and contrasted in Fig. 5.8.

Adding MasterMatrix (MM) or LPP increases the HB yield stress. However, MM increases the HB yield stress at half its maximum dosage (0.5%), more than LPP at the maximum dosage used in this study (0.12%). Although both *K* and *n* parameters of the HB model are nothing more than fitting parameters [189], both MM and LPP keep the flow index at the range of 1.2 to 1.6. Fig. 5.8 also demonstrates that diutan gum increases the HB yield stress more than HPP at similar dosages. Furthermore, adding HPP changes the sign of the flow index, making the curvature negative.
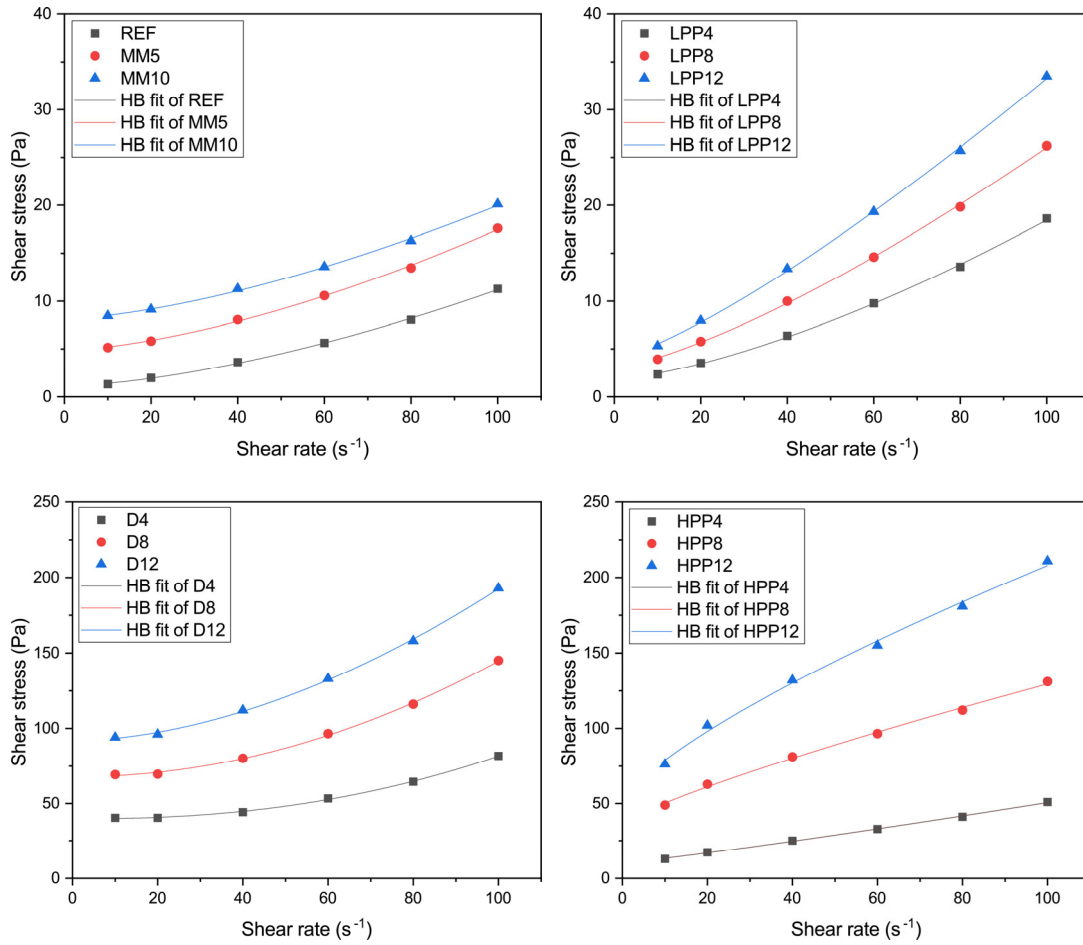
**Figure 5.7:** Rheological data and Herschel-Bulkley fits of grouts with different viscosity-modifying admixtures (REF: reference; MM: MasterMatrix; D: diutan gum; LPP: Low-energy milled paper pulp, and HPP: High-energy milled paper pulp).
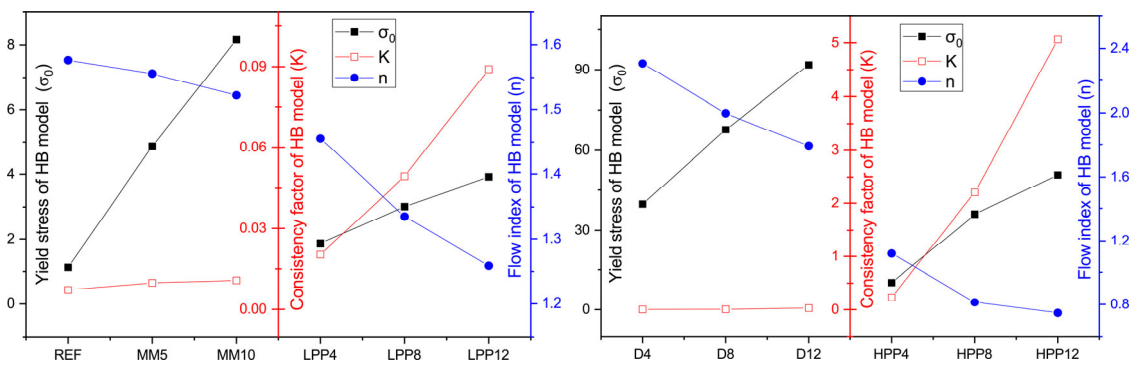


**Figure 5.8:** Herschel-Bulkley model parameters of grouts with different viscosity-modifying admixtures (REF: reference; MM: MasterMatrix; D: diutan gum; LPP: Low-energy milled paper pulp, and HPP: High-energy milled paper pulp).

### 5.3.2 Effects of milled paper pulp fineness on hydration kinetics

A comparison of the effects of milled paper pulp fineness (LPP and HPP) with two commercially-available VMAs on hydration kinetics is illustrated by the isothermal hydration profiles in Fig. 5.9.
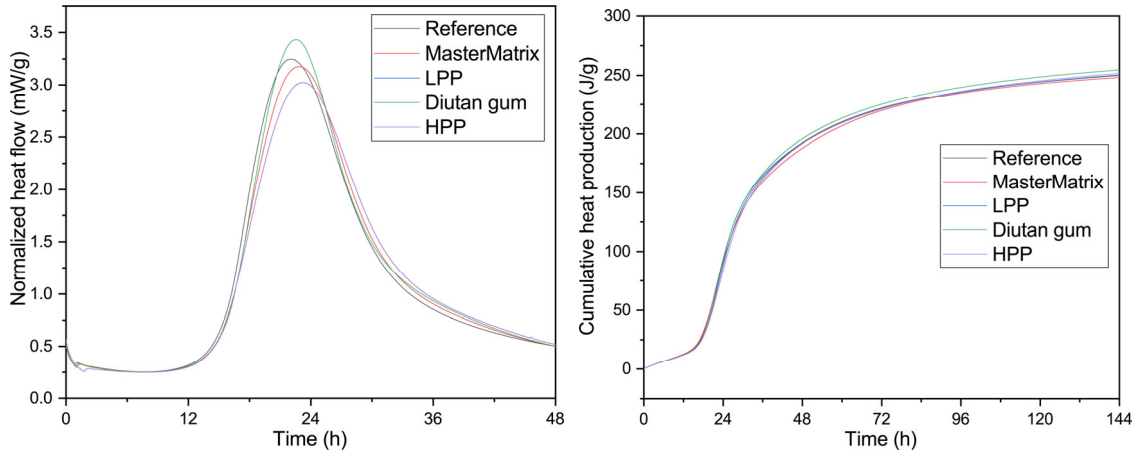


**Figure 5.9:** Isothermal hydration profiles of HPP, LPP, and commercially-available VMAs: (left) heat flow; (right) cumulative heat release.

An isothermal hydration profile is a useful tool to compare the rate of hydration over time and can be used to calculate the thermal indicator of setting time, which is the hydration time to reach a thermal power of 50% of the maximum value of the main peak [186]. Studies have shown that some wood-based pulps may deteriorate hydration kinetics due to water-soluble sugars [190,191]. The effect of MasterMatrix, diutan gum, LPP, and HPP on both thermal indicator of setting time and hydration kinetics are insignificant. This negligible influence may be attributed to the very low dosages of the admixtures needed for modifying the rheological properties. The cumulative hydration heat curves also display a very similar degree of hydration heat for all VMAs in six days.

The peak of all isothermal hydration profiles occurs at around 24h. This retarding behavior is due to the PCE superplasticizer, incorporated in all the mixtures. The mixture having diutan gum has a slightly higher hydration peak. This result confirms the findings by Ciobanu et al. [192], that diutan gum increases the calcium hydroxide content and hydration degree and can be attributed to the low charge density of diutan gum and its tendency to adsorb out of mixing water and onto cement hydration products [193]. These studies [192,193] have also shown that these characteristics lead to lower early-age compressive strength in mixtures containing diutan gum and are discussed in Section 5.4.

### 5.3.3   Effects of milled paper pulp fineness on shrinkage

The effects of the fineness of milled paper pulp (HPP and LPP) on the autogenous shrinkage of the mixtures are compared with those of the commercially-available VMAs in Fig. 5.10. As the rate of autogenous shrinkage is higher at an early age, time is shown in logarithmic scale.
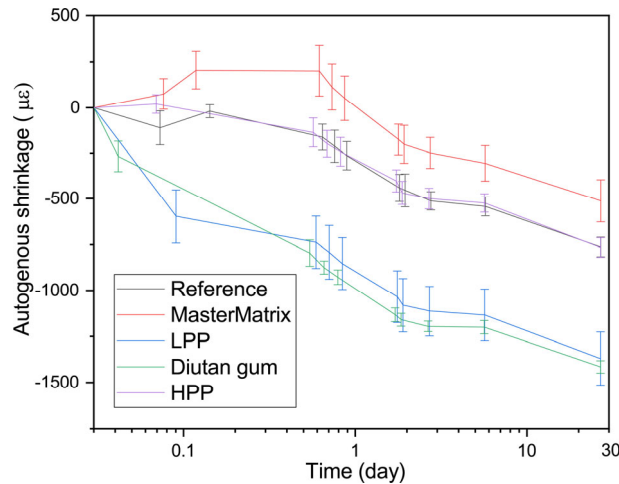


**Figure 5.10:** Autogenous shrinkage of cement grouts with different VMAs.

Diutan gum increases the autogenous shrinkage of cement grout and doubles it after 28 days. The influence of LPP on autogenous shrinkage is similar to that of diutan gum, both increasing its value. By contrast, HPP does not affect the autogenous shrinkage of mixtures, and its value of shrinkage remains similar to that of the reference. The different influence of HPP and LPP on shrinkage may be attributed to the morphology and size differences in LPP and HPP, as previously shown in Fig. 5.2 and Fig. 5.3.

### 5.3.4   Simulated aging of milled paper pulp

Paper pulp consists of cellulose, which has glucose units linked by an ether bond named β-glycosidic linkage. Different parts of the structure can be characterized by FT-IR, as shown in Fig. 5.11, where four different parts of cellulose can be distinguished. The primary and secondary alcohols of the glucose units are shown in red color. The alkenyl bonds forming the cyclic structure of the glucose (and a part of the secondary alcohols in the equatorial position) are shown in green color. The ether bond in the glucose unit and the β-glycosidic linkage between two glucose units are shown by blue and purple color, respectively.

Moreover, as cellulose is a hygroscopic material, bonded water can also be attached to the alcohol groups. Table 5.3 sums up the corresponding bonds as characterized by FT-IR.
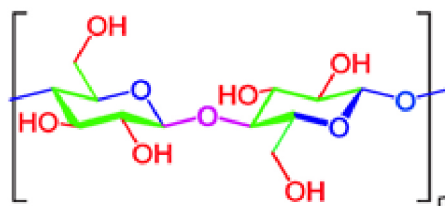


**Figure 5.11:** Cellulose structure. The chemical functions are highlighted [194].

**Table 5.3:** Chemical bonds of cellulose and their respective wavelength in FT-IR spectrometry [195].

| Function | Description | Wavelength ($cm^{-1}$) |
|---|---|---|
| -OH | Primary and secondary alcohols | 3600-3200 |
| -O- | Ether bonds (glucose) | 1205-1050 (several) |
| -CH$_2$- | Alkenyl bonds | 2900; 1370 |
| -O- | β-glycosidic linkage | 900 |
| H-O-H | Bonded water | 1640 |

The FT-IR analyses of LPP and HPP, before and after simulated aging in an alkaline solution, are shown in Fig 5.12 and Fig 5.13, respectively. Table 5.4 shows a summary of the results by assigning characteristic peaks to their corresponding function for each sample. Before and after simulated aging, the spectra of LPP are quite similar, with the presence of cellulose characteristic bonds such as $\nu_{OH}$, $\nu_{CH}$, and $\nu_{C-O-C}$. Nevertheless, some structural changes are noticeable with the disappearance of peaks at 1250 $cm^{-1}$ and 800 $cm^{-1}$, which correspond to benzoate ether and C-C bonds, respectively. As these bonds are not present in the cellulose, it indicates the presence of impurities at the surface of the LPP, which are removed after simulated aging. With HPP, the first observation is the presence of water after aging, with broad bands at 1634 and 3320 $cm^{-1}$ due to the storage conditions. The two spectra are comparable except the significant reduction of the peak at 873 $cm^{-1}$, indicating some fragmentation of the β-glycosidic bond in the cellulose. On the whole, both HPP and LPP show good stability in a highly alkaline environment for a long duration (here, 20 days), and the cellulose structure remains undamaged.
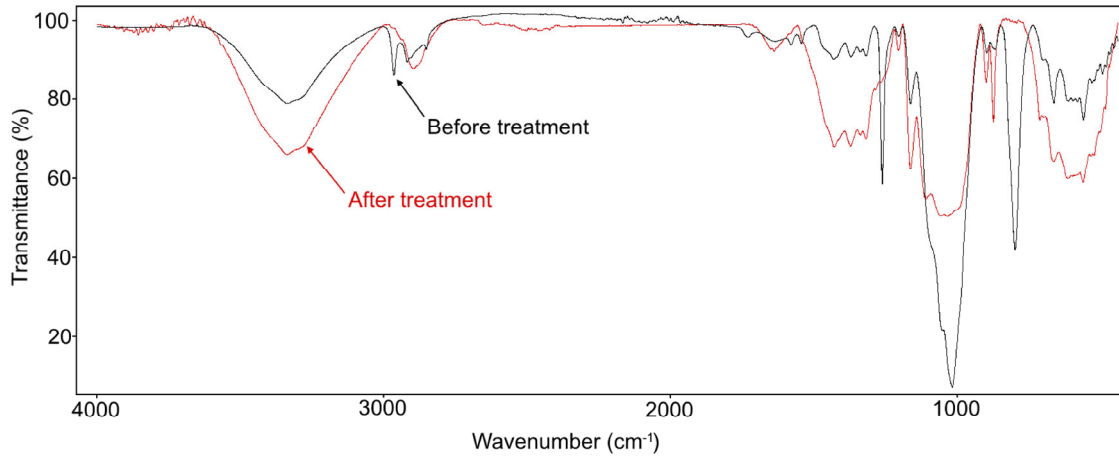
**Figure 5.12:** FT-IR spectra of LPP before (in black) and after (in red) simulated aging.
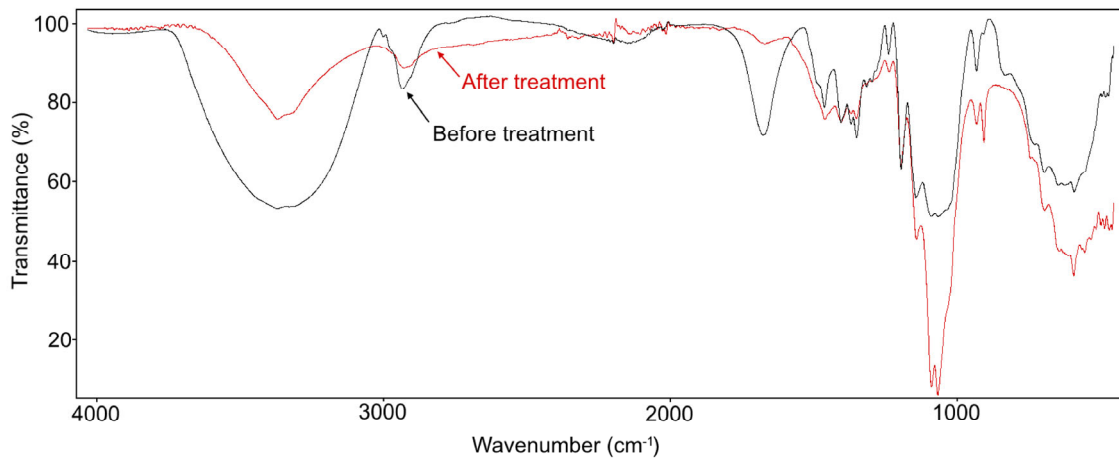


**Figure 5.13:** FT-IR spectra of HPP before (in black) and after (in red) simulated aging.

**Table 5.4:** Main FTIR absorption band assignments.

| Wavenumber (cm⁻¹) | LPP before | LPP after | HPP before | HPP after |
|---|---|---|---|---|
| $\nu_{OH}$* | 3333 | 3339 | 3335 | 3334 |
| $\nu_{CH}$* | 2962-2915 | 2920-2851 | 2900 | 2896 |
| $H_2O$ absorbed | - | 1636 | - | 1645 |
| $\delta_{CH2}$‡ | 1429 | 1428 | 1428 | 1424 |
| $\delta_{CH}$‡, $\nu_{COO}$* | 1369 | 1370 | 1370 | 1375 |
| $\nu_{C\text{-}O}$*, $\delta_{OH}$‡ | 1161 | 1161 | 1160 | 1161 |
| $\nu_{C\text{-}O}$* | 1048-1015 | 1033 | 1053-1034 | 1060-1031 |
| $\nu_{C\text{–}O\text{–}C}$* | 894-872 | 897-872 | 896-875 | 899 |

* ν: bending vibration; ‡ δ: stretching vibration.

### 5.3.5 Effects of milled paper pulp fineness on compressive and flexural strengths

The influences of different VMAs on the average compressive strengths of mortars at 1, 7, and 28 days are demonstrated in Fig. 5.14. As mentioned previously, in order to elaborate on these influences, Welch's analysis of variance is applied. Welch's tests of the VMAs' influence on the 1-day, 7-day, and 28-day compressive strengths of mortars are listed in Table 5.5.
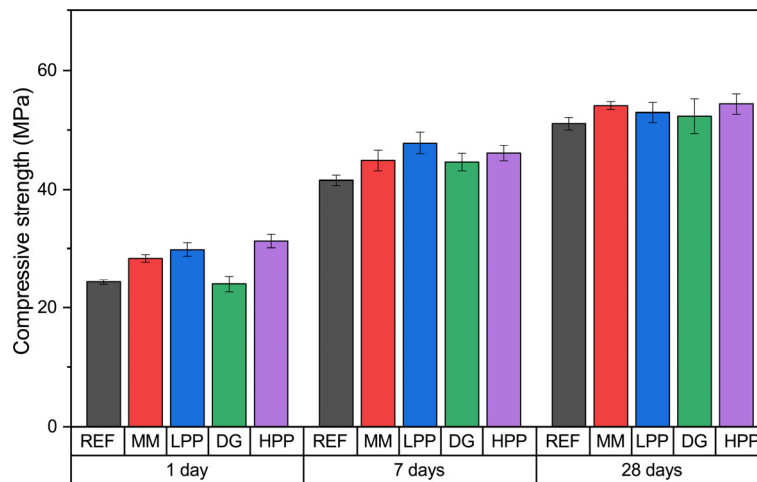


**Figure 5.14:** Influence of different VMAs on the average compressive strengths of mortars at 1, 7, and 28 days. Error bars show the standard deviation. (REF: reference; MM: MasterMatrix; D: diutan gum; LPP: Low-energy milled paper pulp, and LPP: High-energy milled paper pulp).

The standard deviations of the strengths of the mortars have significant differences, which show that the choice of Welch's ANOVA over Fisher's ANOVA is reasonable. Welch's tests of the mean compressive strengths at all ages have p-values less than 0.05. This fact reveals that the differences in the average 1-day, 7-day, and 28-day compressive strengths of some mortars are significant. The high predicted $R^2$ (87.64%) in Welch's tests of the 1-day compressive strengths shows that the model generates robust predictions for new observations. Although the predicted $R^2$ of 7-day strengths is 56.32%, which shows a fairly strong correlation, it falls to 6.79% for 28-day average strengths, which reveals that at this age, the model generates imprecise predictions for new observations and should not be used to make generalizations beyond the sample data. This low predicted $R^2$ can be attributed to a small sample size (N = 6).

**Table 5.5:** Welch's analysis of variance (ANOVA) of the effect of VMAs on the 1-day, 7-day, and 28-day compressive strengths of the mortars (CI: confidence interval for group means; DF Den: degrees of freedom for the denominator; DF Num: degrees of freedom for the numerator; N: sample size; R-sq(adj): adjusted $R^2$; R-sq(pred): predicted $R^2$; and StDev: standard deviation).

**Welch's Test (1-day compressive strengths)**

| Source | DF Num | DF Den | F-Value | P-Value |
|---|---|---|---|---|
| Factors (VMAs) | 4 | 11.8218 | 85.70 | 0.000 |

**Model Summary**

| R-sq. | R-sq.(adj.) | R-sq.(pred.) |
|---|---|---|
| 91.42% | 90.05% | 87.64% |

**Means**

| Factor | N | Mean | StDev | 95% CI |
|---|---|---|---|---|
| LPP | 6 | 29.832 | 1.113 | (28.663, 31.000) |
| HPP | 6 | 31.257 | 1.125 | (30.076, 32.437) |
| REF | 6 | 24.293 | 0.411 | (23.862, 24.724) |
| MM | 6 | 28.350 | 0.632 | (27.687, 29.013) |
| D | 6 | 23.957 | 1.335 | (22.555, 25.358) |

**Welch's Test (7-day compressive strengths)**

| Source | DF Num | DF Den | F-Value | P-Value |
|---|---|---|---|---|
| Factors (VMAs) | 4 | 12.1869 | 19.45 | 0.000 |

**Model Summary**

| R-sq. | R-sq.(adj.) | R-sq.(pred.) |
|---|---|---|
| 69.66% | 64.81% | 56.32% |

**Means**

| Factor | N | Mean | StDev | 95% CI |
|---|---|---|---|---|
| LPP | 6 | 47.790 | 1.858 | (45.840, 49.740) |
| HPP | 6 | 46.038 | 1.316 | (44.657, 47.420) |
| REF | 6 | 41.520 | 0.862 | (40.616, 42.424) |
| MM | 6 | 44.807 | 1.726 | (42.995, 46.618) |
| D | 6 | 44.538 | 1.474 | (42.991, 46.086) |

**Welch's Test (28-day compressive strengths)**

| Source | DF Num | DF Den | F-Value | P-Value |
|---|---|---|---|---|
| Factors (VMAs) | 4 | 11.7796 | 8.21 | 0.002 |

**Model Summary**

| R-sq. | R-sq.(adj.) | R-sq.(pred.) |
|---|---|---|
| 35.27% | 24.92% | 6.79% |

**Means**

| Factor | N | Mean | StDev | 95% CI |
|---|---|---|---|---|

| | | | | |
|---|---|---|---|---|
| LPP | 6 | 52.897 | 1.665 | (51.150, 54.643) |
| HPP | 6 | 54.305 | 1.678 | (52.544, 56.066) |
| REF | 6 | 51.057 | 1.038 | (49.967, 52.146) |
| MM | 6 | 54.013 | 0.648 | (53.333, 54.693) |
| D | 6 | 52.29 | 2.88 | (49.27, 55.31) |

Games-Howell post-hoc test results are shown in Fig. 5.15. All of the confidence intervals of the pairs having the reference, do not contain zero, which means significant differences. The pairwise comparisons also show that both HPP and LPP result in mortars with significant differences in average compressive strengths.

In order to elucidate these differences, Games-Howell groupings at 95% confidence at different ages are reported in Table 5.6. The average compressive strengths of VMAs, which are not grouped, are significantly different. HPP and LPP are grouped at all ages. This group has significantly different 1-day compressive mean strength than the group of the reference mortar and diutan gum. On the other hand, HPP, MM, and diutan gum constitute a group at seven days, which has significantly different average strength with the reference. These differences fade at 28 days as three groups reduce to two groups.

The average flexural strengths of mortars at 1, 7, and 28 days are demonstrated in Fig. 5.16. As shown in Table 5.6, the p-values of Welch's ANOVA of these results at all ages have values more than 0.05, the null hypotheses cannot be rejected, and there is no evidence in the data to conclude that the average flexural strengths are significantly different.
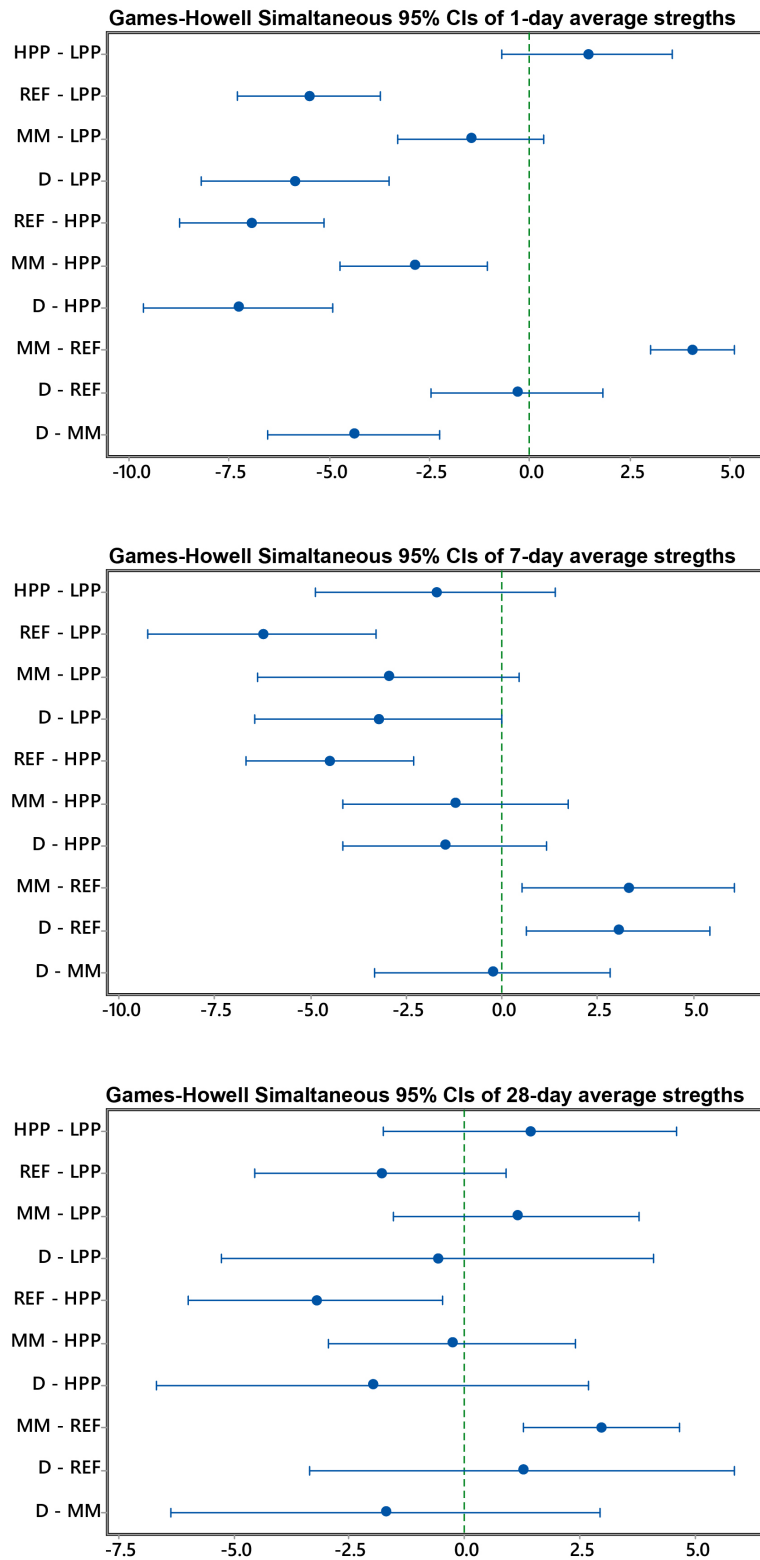
**Figure 5.15:** Games-Howell simultaneous tests at 95% confidence intervals for differences of average 1-day, 7-day, and 28-day compressive strengths of mortars. The Intervals that do not contain zero have significantly different means.

**Table 5.6:** Games-Howell grouping information of the 1-day, 7-day, and 28-day compressive strengths of mortars at 95% confidence. Means that do not share a letter are significantly different.

**Games-Howell Pairwise comparison (1-day compressive strengths)**

| Factor | N | Mean | Grouping | | |
|--------|---|--------|---|---|---|
| HPP | 6 | 31.257 | A | | |
| LPP | 6 | 29.832 | A | B | |
| MM | 6 | 28.350 | | B | |
| REF | 6 | 24.293 | | | C |
| D | 6 | 23.957 | | | C |

**Games-Howell Pairwise comparison (7-day compressive strengths)**

| Factor | N | Mean | Grouping | | |
|--------|---|--------|---|---|---|
| LPP | 6 | 47.790 | A | | |
| HPP | 6 | 46.038 | A | B | |
| MM | 6 | 44.807 | A | B | |
| D | 6 | 44.538 | | B | |
| REF | 6 | 41.520 | | | C |

**Games-Howell Pairwise comparison (28-day compressive strengths)**

| Factor | N | Mean | Grouping | |
|--------|---|--------|---|---|
| HPP | 6 | 54.305 | A | |
| MM | 6 | 54.013 | A | |
| LPP | 6 | 52.897 | A | B |
| D | 6 | 52.29 | A | B |
| REF | 6 | 51.057 | | B |
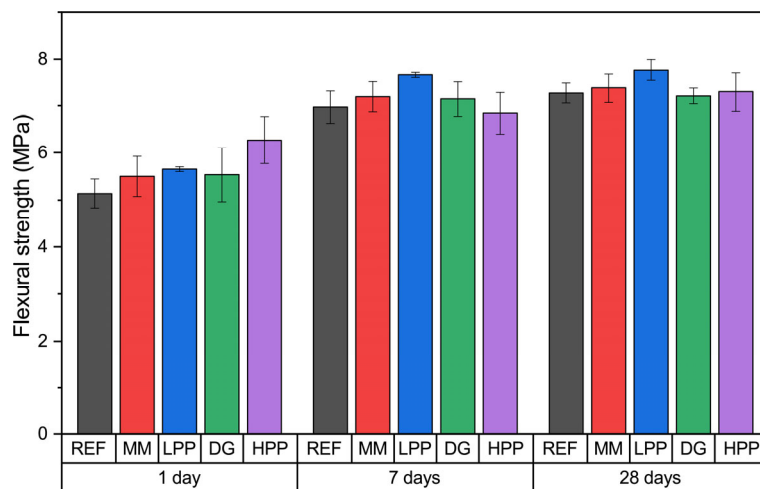


**Figure 5.16:** Influence of different VMAs on the average flexural strengths of mortars at 1, 7, and 28 days. Error bars show the standard deviation. (REF: reference; MM: MasterMatrix; D: diutan gum; LPP: Low-energy milled paper pulp, and HPP: High-energy milled paper pulp).

**Table 5.7:** Welch's analysis of variance (ANOVA) of the effect of VMAs on the 1-day, 7-day, and 28-day flexural strengths of the mortars (DF Den: degrees of freedom for the denominator; DF Num: degrees of freedom for the numerator).

**Welch's Test (1-day flexural strengths)**

| Source | DF Num | DF Den | F-Value | P-Value |
|---|---|---|---|---|
| Factors (VMAs) | 4 | 4.11667 | 2.26 | 0.221 |

**Welch's Test (7-day flexural strengths)**

| Source | DF Num | DF Den | F-Value | P-Value |
|---|---|---|---|---|
| Factors (VMAs) | 4 | 4.15687 | 5.65 | 0.057 |

**Welch's Test (28-day flexural strengths)**

| Source | DF Num | DF Den | F-Value | P-Value |
|---|---|---|---|---|
| Factors (VMAs) | 4 | 4.90180 | 2.24 | 0.203 |

## 5.4  Discussion

The present study starts with rheological behavior analysis to assess the performance of milled paper pulp at two levels of fineness (LPP and HPP) and compares and contrasts their rheological data with those of two commercially available VMAs (MasterMatrix and diutan gum). Several rheological models have been introduced in the literature to interpret the rheological properties of cementitious materials, namely Bingham, Herschel-Bulkley, Casson, Eyring, Robertson-Stiff, De Kee, and Vom Berg models [185]. Among these, the Bingham model is more than just a fitting equation and reveals the physical differences of cement grouts. For example, plastic viscosity shows the stickiness of the material, while the critical stresses required to break the structure of cement grouts are shown by the yield stress. VMAs increase both the yield stress value and the plastic viscosity value of cement grouts [171,196]. If a graph of yield stress axis and plastic viscosity axis is made, the influence of VMAs on the rheological behavior of cement grouts can be compared [75], as shown in Fig. 5.17.

Such a graph is used in Fig. 5.18 to compare and contrast data on the influence of different levels of fineness of paper pulp on the rheological properties of cement grouts. This Figure highlights the significantly different influences of LPP and MasterMatrix on the flow parameters of cement grouts. While MasterMatrix affects the yield stress significantly, LPP mainly affects the plastic viscosity. Besides, the plastic viscosity-yield stress ratio of the HPP grouts are higher than that of diutan gum grouts at similar dosages. These insights on the performance of VMAs provide a basis for understanding the mechanism of action of paper

pulp on the rheological properties of cement composites and may be used in choosing VMAs for different applications.
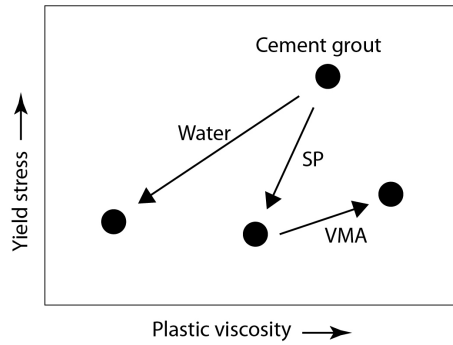


**Figure 5.17:** Effect of adding water, superplasticizer (SP), or VMA on the Bingham yield stress and plastic viscosity of cement grout [75].
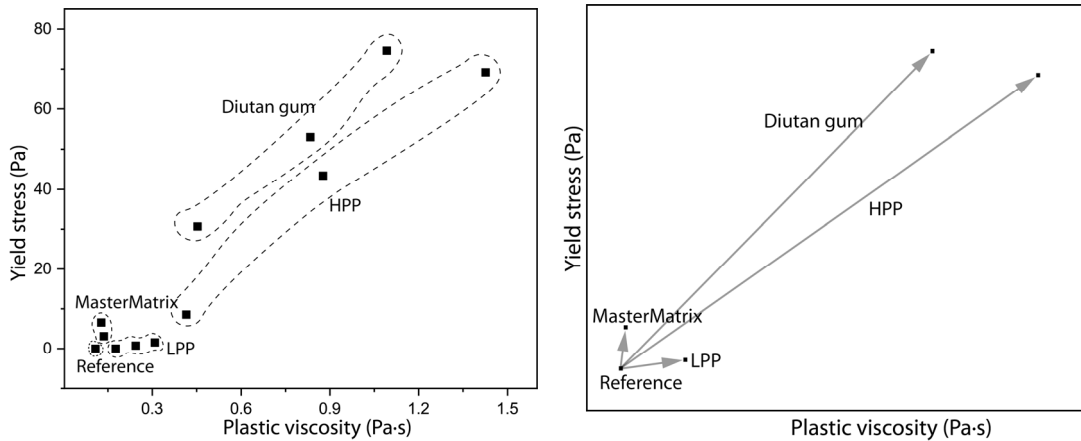


**Figure 5.18:** Effect of different VMAs on the Bingham yield stress and plastic viscosity of cement pastes at the maximum dosage studied in this paper.

Furthermore, Fig. 5.18 shows that the influence of HPP on the flow parameters of cement grouts is a few times more significant than that of LPP at similar dosages. This difference can be attributed to the changes caused by milling to the mechanism of action of paper pulp. As previously shown in Fig. 5.2, while ultrafine fibers make up around 30% of LPP, their percentage rises to around 85% in HPP.

Besides, Fig. 5.18 demonstrates that diutan gum increases yield stress a little more than HPP and enhances plastic viscosity slightly less than HPP. The high values of yield stress and plastic viscosity in diutan gum can be attributed to the working mechanism of diutan gum in the presence of polycarboxylate ether-based superplasticizers, which is based on its high molecular weight and water immobilization [81,193].

Fig. 5.19 shows an SEM picture of LPP diluted in water and deposited on a silicon wafer. Item 1 shows long fibers, while Item 2 shows a stack of ultrafine fibers. The fibers are able to hold cement particles together and modify the rheological behavior of cement grouts by bridging flocculation. The magnitude of this physical mode of action can be modified by incorporating 3rd generation superplasticizers (polycarboxylic ether (PCE) based SPs) in the mixture, as these SPs cause cement particles to repel each other through a combination of electrostatic repulsion and steric hindrance [197–200] or just through steric hindrance [200–202]. Furthermore, as paper pulp fibers are hydrophilic, they can absorb and retain water resulting in a higher concentration of the matrix and a higher value of viscosity. Mechanical milling affects both bridging flocculation and swelling mechanisms of fibers and changes the performance of LPP to that of HPP as a VMA.
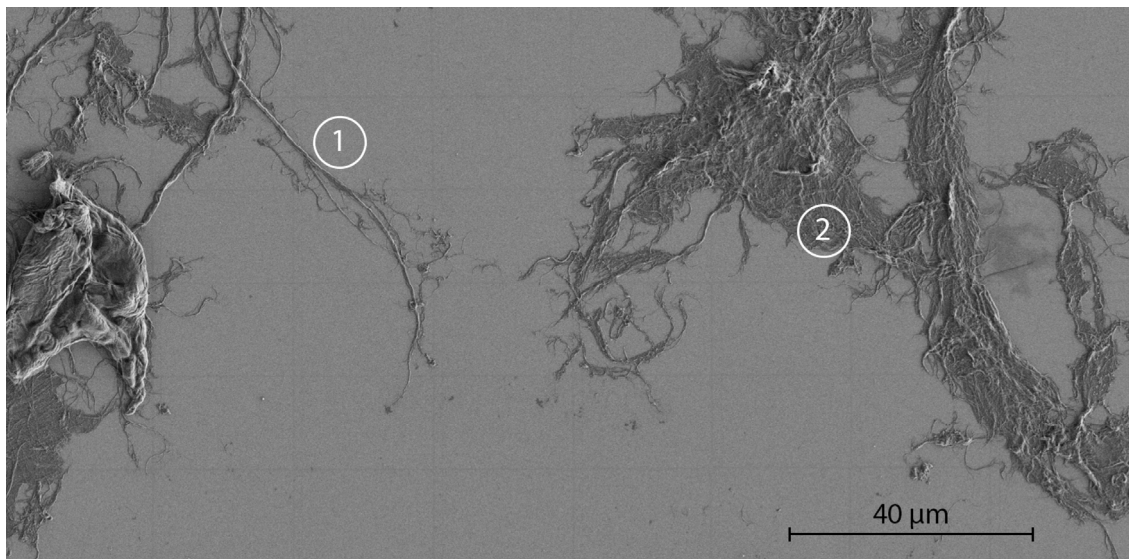


**Figure 5.19:** SEM picture of LPP in water with ET detector; 1-long fibers, 2-small fibers (Courtesy of Sappi®).

The dynamic yield stress is calculated by extrapolating rheological data. Hence, although the linear Bingham model provides a basis to compare and contrast different VMAs based on yield stress and plastic viscosity, the value of the extrapolated dynamic yield stress diverges from its true value as nonlinearity in the rheological data rises. In these cases, the Herschel-Bulkley model gives a more realistic yield stress value as it fits nonlinear data better. However, as this model does not give information on the viscosity of the cement grouts, comparing different VMAs with this model is difficult. In order to take this nonlinearity into account, a few researchers proposed to use a second-order polynomial model as follows [203,204]

$$\sigma = \sigma_D + \eta_B \dot{\gamma} + c\dot{\gamma}^2 \tag{5.3}$$

with $c$ the c-parameter, and $\sigma_D$, $\sigma$, $\dot{\gamma}$, and $\eta_B$ as used previously. The modified Bingham properties are then calculated by suppressing the second-order term, which is significantly low [205]. However, if the second-order term is insignificant, there is no reason to be suppressed. If not, it might be erroneous to use the modified Bingham model this way, as it cannot differentiate between a material with modified Bingham properties ($\sigma_D$, $\eta_B$, $c$) of say ($a,b,c$) with another material with modified Bingham properties of ($a,b,c'$). Hence, this study proposes to apply the modified Bingham model, but instead of suppressing the c-parameter, utilize it to show the deviation from the Bingham model or in other words to show the nonlinearity. The c-parameter of the grouts are shown in Fig. 5.20. The adjusted $R^2$ of the model in all computations were more than 0.99, which shows a strong correlation.
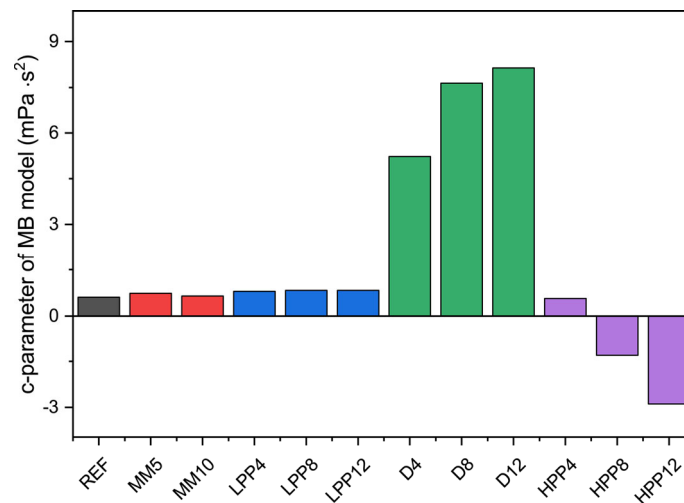


**Figure 5.20:** c-parameter of the Modified Bingham model (Eq. 5.3).

As illustrated in Fig. 5.21, the c-parameter of the grouts containing MM and LPP remains similar to that of the reference at all dosages used in this study, while both HPP and diutan gum change this parameter dramatically. Diutan gum increases the c-parameter, which indicates that the true dynamic yield stress of the diutan gum grouts is higher than what presented by the Bingham model. On the other hand, HPP reduces the c-parameter and changes its sign, which indicates that the true dynamic yield stress of the HPP grouts is lower than what obtained from the Bingham model. The higher the dosage, the higher the effect.
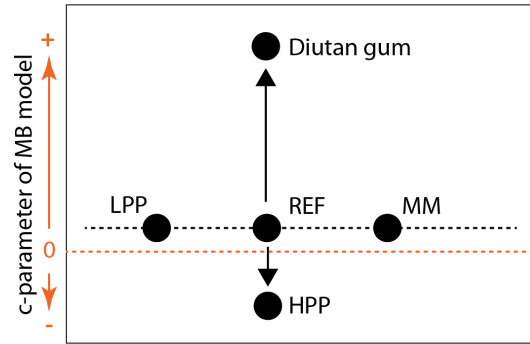
**Figure 5.21:** c-parameter change by adding different VMAs.

In order to assess the influence of LPP and HPP on the fluidity of mortars, flow spread tests by mini-slump cone, at five different dosages, were performed. The ratio of water:cement:sand in the mortars were kept constant at 1:2:6, similar to EN 196-1 [121]. The flow spread tests were used to calculate the relative slump flow parameter, $\Gamma$, [206,207] as follows

$$\Gamma = (\frac{d_1+d_2}{2d_0})^2 - 1 \tag{5.4}$$

with $\Gamma$ the relative slump flow, $d_1$ the diameter in the direction where it appears to be longest, $d_2$ the diameter perpendicular to the first measurement (cm), and $d_0$ the flow cone diameter ($d_0$ = 10 cm). Some researchers [206] proposed to use this parameter to determine the minimum water demand to initiate flow (MWD) and relative water demand to increase fluidity (RWD) in mortars. With the objective to calculate MWD and RWD, a linear regression analysis between $\Gamma$ and $w/c$ is performed, where the intercept of the linear fit represents the MWD, and the slope of the linear fit represents the RWD [207].

This study proposes to use the relative slump flow to compare and contrast the influence of LPP with that of HPP on the fluidity of mortars by introducing two parameters: (1) minimum VMA demand to stop flow (MVD), and (2) relative VMA demand to decrease fluidity (RVD). With the objective to calculate MVD and RVD, a graph of the dosage of paper pulp axis and the relative slump axis is made. Then, a linear regression analysis is performed, in which the intercept of the linear regression equation represents minimum VMA demand to stop flow (MVD), and the absolute slope of the linear regression equation represents relative VMA demand to decrease fluidity (RVD). Fig. 5.22 displays these parameters along with the flow characteristics of the standard mortars having LPP and HPP. Incorporating HPP in mortars lowers the value of MVD by 35% and reduces the value of

RVD by 31% in comparison to LPP. In other words, HPP more efficiently controls the fluidity of mortars by increasing viscosity.
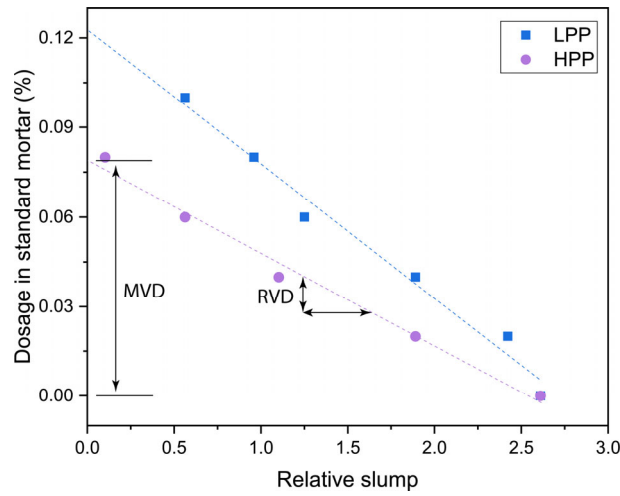


**Figure 5.22:** Flow characteristics of the standard mortars having LPP and HPP, using the relative slump parameter, calculated based on the mini-slump flow test.

The small dosages of HPP and LPP needed for viscosity-modifying effect, have an insignificant effect on the hydration kinetics of cement grouts and flexural strength of mortars. However, they affect the compressive strength of mortars. Because of the differences in the variances of the compressive strength of mortars, Welch's ANOVA is used. Games-Howell grouping trend of compressive strengths of mortars at 95% confidence at different ages are shown in Fig. 5.23. VMAs that are not in an enclosed area are significantly different. The mean strength of HPP and LPP mortars are significantly different from that of the reference at one and seven days. The difference between LPP and the reference fades after 28 days as the grouping becomes broader and less variant. However, ultrafine milled paper pulp (HPP) continues to have significantly different compressive strength at 28 days.

The higher strength at early-age in mixtures containing HPP and LPP are in line with the findings on the compressive strength development in cement composites containing low dosages of cellulose filaments [208] and can stem from the bridging effect thanks to the developed bond between paper pulp filaments and cement hydration products. On the other hand, the lower early-age strength in mixtures containing diutan gum is in line with the findings on the low compressive strength of mixtures containing diutan gum [192] as a result of low charge density of diutan gum and its tendency to adsorb out of mixing water and onto cement hydration products [193]. However, at later ages, as more hydration products

are developed in the mixtures, the influence of these characteristics in paper pulp and diutan gum diminishes, and the obvious difference in compressive strength after one day fades away after twenty-eight days.
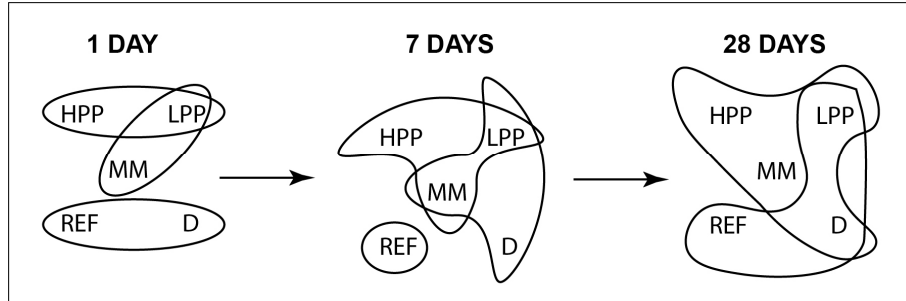


**Figure 5.23:** Games-Howell grouping trend of compressive strengths of mortars at 95% confidence at different ages. VMAs that are not in an enclosed area are significantly different.

In light of the fact that the main aim of this investigation is shedding more light on the versatility and the value that the milling process adds to paper pulp as a viscosity modifying admixture, various characteristics of cement composites containing HPP and LPP are tested in the first month after casting. Further research may investigate the durability of paper pulp in cement composites.

## 5.5 Conclusions

In the present research, the effects of fineness of milled paper pulp (LPP and HPP), obtained from different levels of industrial mechanical milling of the same source of paper pulp, on the fresh and hardened properties of cement grouts are investigated. Two commercially available viscosity modifying admixtures, namely diutan gum and MasterMatrix, are used for comparison analysis. Based on the properties assessed and the results obtained, the following conclusions can be drawn:

- Milled paper pulp, made by both mechanical milling procedures, modifies the rheology of cement grouts and can be categorized as a sustainable VMA. The viscosity-modifying mechanism of action of paper pulp in cement grouts is a combination of bridging flocculation and swelling.

- High-energy milled paper pulp (HPP) consists mostly of the ultrafine fibers of the hierarchical structure of paper pulp and enhances both the plastic Bingham viscosity and dynamic yield stress of cement grouts more significantly than low-energy milled paper pulp (LPP).

- The range of the rheological effect of HPP on cement grouts is analogous to that of diutan gum at similar dosages. However, the ratio of the plastic viscosity to the yield stress in HPP is more significant than that of diutan gum grouts.

- The influence of the low-energy milled paper pulp (LPP) on the rheological behavior of cement grouts differs from that of the high-molecular-weight synthetic copolymer (MM) in that while the LPP mainly increases the plastic viscosity, the synthetic copolymer primarily changes the yield stress.

- The c-parameter of a second-order modified Bingham model is proposed to take the differences in the nonlinearity of grouts into account. While LPP and the high-molecular-weight synthetic copolymer (MM) do not influence the c-parameter of the cement grout, both HPP and diutan gum affect it significantly. Contrary to diutan gum that increases the c-parameter, HPP decreases it and makes its value negative. This change in sign of the c-parameter is an indicator of the fact that the true dynamic yield stress of the HPP grouts is lower than what obtained from the Bingham model.

- Both LPP and HPP do not affect the hydration kinetics and thermal indicators of setting time. Besides, they both show good stability in a highly alkaline environment.

- Welch's ANOVA confirms a significant difference in average compressive strength of mortars with paper pulp with that of the reference. Games-Howel post hoc test shows that both LPP and HPP increase the 1-day and 7-day compressive strength of the mortars, compared to the reference. After 28 days the significance of the difference between the compressive strength of reference mortars with that of LPP mortars fades but HPP mixtures continue to have higher compressive strength. A similar analysis shows that milled paper pulp does not affect the flexural strength of mortars, at the dosages used for flow adjustment.

# Waste baby diapers to modify rheological behavior

*Waste baby diapers constitute a significant part of hygiene waste and currently are primarily landfilled or incinerated. The present chapter explores the applicability of shredded waste diapers (SWDs) as an innovative viscosity modifying admixture for cement grouts and concrete. A model was proposed which formulates the chemicals that SWDs add to concrete. The model was combined with the building and environmental standards to present the legal framework about using SWDs in different types of concrete. Cement grouts and self-consolidating concrete were designed to validate the viscosity modifying properties of SWDs. A Bingham viscosity model and flow tests were used to evaluate the viscosity modifying performance of SWDs. The present results show that the SWDs are a sustainable route to manufacture highly-effective viscosity-modifying admixtures for concrete.*

## 6.1 Introduction

Waste baby diapers have received much attention in recent years because of their high volume and complicated recycling process. Baby diapers accounted for more than 74% of the 7.1 billion USD global superabsorbent polymers (SAPs) market with a production rate of 2.119 million tons in 2014 [62]. Currently, waste baby diapers account for 2% to 7% of municipal solid waste [63]. Despite their high volume and excellent water absorption, waste baby diapers have been mostly landfilled [63] or incinerated [64]. In Europe, 68% of waste baby diapers are landfilled and 32% incinerated, while for the USA, the numbers are 80% and 20%, respectively [65]. Landfilling causes serious environmental problems such as methane emissions, water pollution, land use, and odor [66,67]. Furthermore, some studies have shown that the biodegradation of baby diapers in landfills is unlikely to happen due to both low biological activity in landfills and the fact that consumers tend to throw waste baby

diapers away by wrapping them in plastic [68,69]. Therefore, there is an urgent need to introduce new measures to deal with waste baby diapers. It should also be noted that waste baby diapers, as a bio-degradable waste, were subsumed under EU landfill directive 1999/31/EC [209], which had requested to reduce bio-degradable waste in 2016 to 35% of its amount in 1995.

A few attempts to valorize waste baby diapers by separating and reusing their valuable components have been reported [210,211]. US patent 5558745A [212] introduced a process that comprises a few steps to wash, bleach, disinfect, divide, and recover streams of plastic and absorbent materials in waste baby diapers. Another similar methodology has recently been developed in the UK to collect superabsorbent hygiene products after sterilizing and recycling waste diapers [213]. A combination of an autoclave and a sorting machine was also proposed to recycle waste baby diapers [63]. However, these methods are costly and produce wastewater that adds up necessary sterilization and wastewater treatment to the total cost of the entire system [214,215]. Composting is another method to deal with waste baby diapers [68,69,216,217]. Although studies show that pathogens can be destroyed in a composting process [218], polymer degradation time is very long [216,219–221]. Microbial biodegradation by different polymer-degrading microorganisms [222–224] and fungus cultivation [225–227] are other proposed approaches to recycle waste baby diapers. Further details on the recent technologies for treatment and recycling of waste baby diapers are provided in a recent review by [228]. Nevertheless, none of these valorization techniques use waste baby diapers as received without further processing.

The SAP market is estimated to be over US$ 9 billion at a volume of 2.892 million tons in 2020 [62]. Such a significant demand and production rate not only highlights the massive volume of resulting waste but also signifies the importance of valorizing waste baby diapers. A successful valorization method for waste baby diapers should be able to effectively address waste diapers' three main characteristics, in terms of high volume, pathogens, and high water-absorption capacity. Concrete is the most widely used human-made material on earth [167,168] and relies on water for rheological properties [229]. Such prominent market and water-dependent rheological properties can be used to form a hypothesis that concrete could be the up-and-coming candidate for valorizing waste baby diapers as a product to modify the rheological behavior of concrete. The admixtures that are used for this purpose are called viscosity modifying admixtures (VMAs). If waste diapers were valorized as a VMA at the dosage of 1% of cement content in just 1% of the concrete manufactured worldwide (annual global production 25 billion tons [167]), several hundred thousand tons of waste diapers

would be recycled annually. Most importantly, concrete has a highly alkaline environment with a pH of around 13 [230] that kills bacteria, viruses, and pathogens [231–234], making this hypothesis more applicable.

This study hypothesizes that implementing waste baby diapers, wetted by urine, in cement composites would introduce a straightforward route to valorize them as sustainable VMAs. VMAs have a variety of applications in the concrete industry. They can be used in self-consolidating concrete (SCC) to reduce the risk of segregation and bleeding [75]. They have been used in underwater concrete to reduce washout [172]. They can also be used as pumping aids in shotcreting [177]. Some studies show that VMAs can help concrete to maintain passing ability and stability at lower levels of cementitious materials [16]. VMAs have also been used in various types of cement composites such as lightweight expanded polystyrene (EPS) concrete [235], 3D printing concrete [180], shotcretes [178], and oil well concrete [179]. Unfortunately, currently-available VMAs are mostly costly, which increases the overall concrete production cost. Hence, introducing new routes to obtain cheaper VMAs is of crucial importance.

To the best of the authors' knowledge, because of the hazardous compounds inside urine, which deteriorate concrete, there has been no study on the application of shredded waste diapers (SWDs) in concrete. Urine has urea [236], which is an organic compound that potentially affects hydration [237]. It also contains chloride [236], which at high dosages destroys the passivity of concrete [3] and speeds up the corrosion of steel rebars [238]. That is why both EN 1008 [239] and ASTM C 1602 [240] specify limits for the chloride ion concentration in combined mixing water of different concrete types. Besides, urine incorporates sulfates [236] that theoretically lead to different types of sulfate attack in concrete [241–243]. Accordingly, both EN 1008 [239] and ASTM C 1602 [240] require limiting this chemical in combined mixing water of concrete as well. The destructive action of these harmful substances depends on the applied dosage of the waste diaper in concrete, and there may exist dosages at which the concentration is lower than the destruction threshold. However, these applicable dosages remain unreported.

The current chapter aims at filling this scientific gap by a systematic study that begins with presenting a computational model. The model quantifies the concentration of chemicals in combined mixing water of a cement composite following the incorporation of shredded waste diapers (SWDs). Next, it applies the model and compares the average concentration of harmful chemicals to concrete in combined mixing water with the requirements of the relevant standards. Subsequently, this study not only confirms the applicability of SWDs but

also provides a legal framework to obtain permitted dosages in different types of concrete. Then, it uses the framework and chooses two SWD dosages to validate the idea of using SWDs as a VMA in cement composites. A Bingham viscosity model and flow tests are applied to evaluate the viscosity-modifying properties of the SWDs.

## 6.2 Experimental

### 6.2.1 Materials

The current investigation involved shredded waste diaper (SWD) manufacture and application as a VMA in cement grouts and self-consolidating concrete. An artificial waste baby diaper was produced by adding an aqueous solution of sodium chloride to fresh diapers. Since urine is a dilute solution of salts in which sodium chloride is the most concentrated, sodium chloride solution has been adopted by both European Disposable and Nonwovens Association (EDANA) and International Organization for Standardization (ISO) for characterizing the urine absorbency of diaper in the following conditions: (1) Free swell capacity (ISO 17190-5:2001 and EDANA NWSP 240.0.R2 (15)); (2) Fluid retentions (ISO 17190-6:2001 and EDANA NWSP 241.0.R2 (15)); (3) Fluid absorption under pressure (ISO 17190-7:2001 and EDANA NWSP 242.0.R2 (15)) [244–249]. The aim of this study was to characterize the applicability of shredded waste baby diaper as a viscosity-modifying admixture in cement composites, and since this property is a combination of swelling and fluid retention under pressure, similar to the standards mentioned above, sodium chloride was utilized for artificial waste baby diaper preparation.

The concentration of salt (NaCl) was three weight percent of ambient dry diapers. Then, in order to reduce the size of dried artificial waste baby diapers, various types of comminution techniques were investigated. As baby diapers are soft, conventional crushers or grinders could not be employed, and the other comminution methods involving knives and rotors seemed to be more suitable. Finally, a Fritsch Pulverisette 15 cutting mill was utilized for SWD manufacturing. It was able to shred waste baby diapers based on the cutting principle of scissors in which the rotation and airflow do not let the baby diapers settle anywhere. The resulting SWDs are shown in Fig. 6.1. Baby diapers are made up of superabsorbent polymers (SAPs), cellulose, and plastic film. The fibrous morphology of shredded waste diapers under an optical microscope is exhibited in Fig. 6.2.

The cement CEM I 52.5 R, provided by ENCI (the Netherlands), was utilized to study the effect of SWDs on the rheological and mechanical properties of cement grouts. The CEM

I 52.5 R is an ordinary Portland cement with Blaine specific surface area of ca. 527 m$^2$/kg. It gains most of its compressive strength after one day [104], which makes it suitable for grouting or shotcreting applications.

The cement CEM III/A 52.5 N, provided by ENCI (the Netherlands), was applied to investigate the influence of SWDs on the flowability and compressive strength of SCCs. The CEM III/A 52.5 N is a binary blend of Portland cement clinker and blast furnace slag that develops strength more smoothly within the first 28 days after casting [250]. It produces less hydration heat and is considered as a sustainable choice for producing mass self-consolidating concrete (SCC).



**Figure 6.1:** Shredded artificial waste diapers produced for experimental investigations.
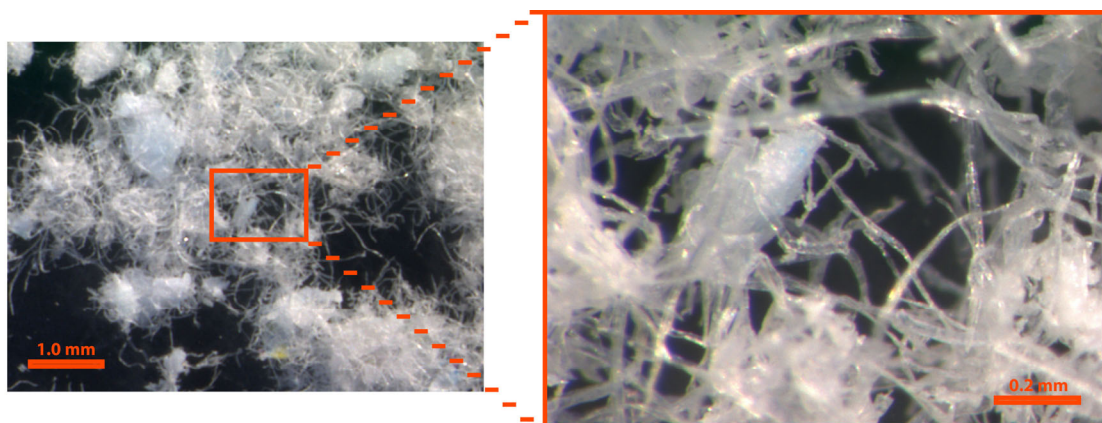


**Figure 6.2:** Morphology of shredded waste diapers under an optical microscope.
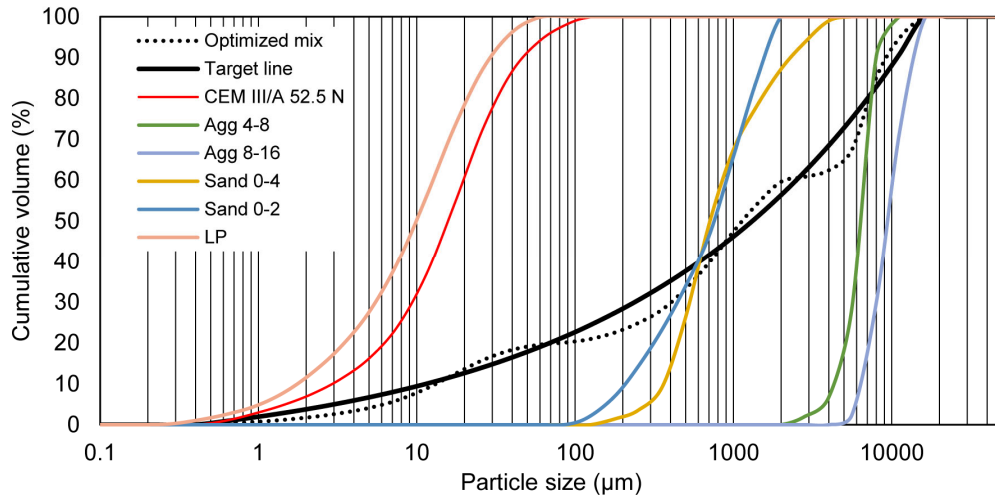
**Figure 6.3:** Particle-size distribution of different ingredients of the self-consolidating concrete. The target line was computed by the modified Andreasen and Andersen model at the distribution modulus of 0.25. The optimized mix is the best fit of the ingredients for the target line.

A polycarboxylic ether-based superplasticizer (SP) with solid content of 35% was used to adjust the flow properties of cement grouts and SCCs. The dosage of the SP refers to the solid as a percentage of the weight of cement. Limestone powder (LP), two types of sand (0-2 mm and 0-4 mm), and two types of gravel (4-8 mm and 8-16 mm) with specific gravities of 2.71, 2.65, 2.63, respectively, were used in proportioning the self-consolidating concrete. The particle size distribution (PSD) of the powders was measured employing a Malvern Mastersizer 2000 while sieve analysis was used to measure the PSD of the aggregates.

Three cement grouts with the water to cement ratio of 0.35 were prepared. Neat cement grout, proportioned without SWDs, was used as the reference. The cement grouts with SWD dosages of 0.5% and 1% by weight of cement were prepared to compare their fresh and hardened properties with those of the reference. These dosages were selected based on the applicability study, elucidated in Sections 6.2.2 and 6.3.1 of this chapter.

The modified Andreasen and Andersen model was used to design SCCs [79,93]. The particle-size distribution (PSD) of the solid ingredients of the SCCs is illustrated in Fig. 6.3 A distribution modulus of 0.25 was used in the computation.

Fig. 6.4 lists the recipes of three self-consolidating concretes. The SCC, having no SWDs, was used as the reference. SWDs were incorporated at the dosages of 0.5% and 1% by mass of cement into the two other mixtures. As mentioned earlier, these dosages were selected

based on the applicability study, elucidated in Sections 6.2.2 and 6.3.1 of this study. The other ingredients were kept the same in all three mixtures.
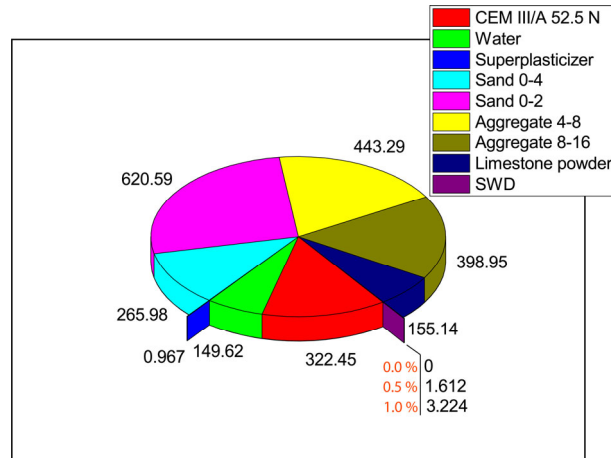


**Figure 6.4:** Recipe of self-consolidating concretes (SCC) incorporating SWDs (kg/m3). SWDs were used at 0.5% and 1% of cement content. The SCC without SWD was used as the reference.

## 6.2.2   Methods

*Applicability study*

Before performing an experimental program to evaluate viscosity modifying capability of SWDs, the applicability of SWDs in cement composites was studied. The applicability study involved four steps: (1) Presenting a computational model; (2) introducing the legal framework; (3) comparing the results of step 1 and step 2; (4) choosing two dosages to perform experiments. The description of the steps is as follows.

First, a computational model was introduced that formulates the concentration of chemicals in combined mixing water of cement composites in the wake of incorporating shredded waste diapers. An average dry diaper weight of 41 g [251] and an average urine output of 161 g per diaper [220] were used in the computations. The average concentration of hazardous chemicals in urine was extracted from [236]. Average concentration of 5135 mg/l for chloride and 2945 mg/l for sulfate were used.

Next, the European and the American standards (EN 1008 [239] and ASTM C 1602 [240]) were utilized to report the requirements about the maximum allowable concentration of chemicals in combined mixing water of different types of concrete.

Then, the average concentrations of hazardous substances, computed in the first step, were compared with the requirements of the relevant standards of the second step to acquire the legal framework about the permitted dosages of SWD in different types of concrete.

Finally, two dosages within the legal framework of almost all concrete types were picked to assess the performance of SWDs as a VMA.

*Fresh and hardened properties of cement grouts*

The grout mixtures were prepared using a high shear mixing protocol beginning with mixing SWDs and cement in the dry state at 800 rpm for 90 s at 25°C. Next, almost 75% of water was added to the mixture and mixed at 2000 rpm for 1 min. Then, the mixer was stopped and scraped for 30 s. Subsequently, the remaining part of the solution of water and SP was added to the mixture and mixed at 2000 rpm for 1 min. Eight minutes succeeding the cement and water contact, the mixtures were placed in a Schleibinger Viskomat XL viscometer, equipped with a fishbone-shaped probe, at 25 °C to study the rheological behavior.

A speed sweep protocol was performed that consisted of five one-minute steps of 10, 20, 40, 60, and 80 rpm, respectively. The torques reached a quasi-steady state at the end of each speed and were recorded. A procedure similar to [252,253] was used to determine flow parameters, using the Bigham equation [252,253]

$$T = G + H \cdot N \tag{6.1}$$

where $T$ is the torque measured on the viscometer [N·mm], $N$ the speed of rotation [rps], $G$ is the yield parameter [N·mm], and $H$ the plastic viscosity parameter [N·mm·s].

Finally, the cement grouts were cast into twelve plastic prism molds, $40 \times 40 \times 160$ mm³, and compacted on a vibration table. A plastic film was used to cover the samples and prevent moisture loss from the molds. All the samples were unmolded approximately 24 h after casting and then submerged in water at about 20 °C for curing. The compressive strength tests were performed, according to EN 196-1 [121], at the curing ages of 1, 3, 7, and 28 days, respectively.

*Fresh and hardened properties of self-consolidating concrete (SCC)*

A standard pan mixer with planetary motion blades was used for the SCC production. SCCs usually demand higher mixing time than normal concrete [254]. Therefore, in order to take the effect of powder content, water-powder ratio, and particle size distribution (PSD) of SCCs [5,254] on the mixing time of the SCC into account, the following procedure was followed. First, all powder ingredients, sand, and SWDs were blended in a dry state for one minute. Then, about 75% of the mixing water was added while further mixing for 90 s. Afterwards, a solution of the superplasticizer and the remaining water was added and mixed for one minute. Finally, the coarse aggregates were added and mixed for another two minutes. Previous studies show that the mixing sequence of superplasticizer with the mixture is an important factor in the flowability of cement composites [255]. Superplasticizer was added at the end of the mixing sequence in order to prevent possible competing of superplasticizer molecules with calcium sulfate present in the cement to combine with $C_3A$ and keep all the superplasticizer molecules ready to make concrete more flowable [106].

Slump flow, v-funnel, and flow time ($T_{500}$) tests were used to analyze the fresh properties of SCCs according to EN 12350-8 [256] and EN 12350-9 [257]. After mixing, SCCs were cast into six cube molds ($150 \times 150 \times 150$ mm$^3$) and covered by a plastic film to prevent moisture loss. All the samples were unmolded approximately 24 h after casting and then submerged in water at about 20 °C for curing. The compressive strength tests were performed after 7 and 28 curing days, according to EN 12390-3 [107].

## 6.3    Results analysis

### 6.3.1    Applicability of waste baby diapers in cement composites

In order to determine the applicability of waste baby diapers in cement composites, the average increased concentration of chemicals in the wake of incorporating SWDs should be formulated. The theoretical basis for this formulation is as follows. Consider a baby diaper with the dry mass $n$ is wetted by urine having the volume $u$ containing a hazardous chemical at the concentration $Q$. The hazardous chemical content $a$ shown as the weight of the chemical substance to the weight of a dried diaper is

$$a = \frac{u \cdot Q}{n} \tag{6.2}$$

Where *a* is the hazardous chemical content per diaper [μg/g], *u* the urine output per diaper [ml], *Q* the concentration of a hazardous chemical in urine [mg/1], and *n* the mass of a diaper [g].

Assume that the urine-wetted diaper is dried, shredded, and added at the dosage d, percent by weight of cement, to a cement composite having a water-cement ratio *w/c*. The increased content of the detrimental chemicals in combined mixing water can be formulated as follows

$$ b = a \left(\frac{d}{100}\right)\left(\frac{w}{c}\right)^{-1} = \left(\frac{u \cdot Q \cdot d}{100 \; n}\right)\left(\frac{w}{c}\right)^{-1} \tag{6.3} $$

Where *b* is the concentration of a hazardous chemical in combined mixing water of a cement composite in the wake of incorporating shredded waste diapers (ppm in water), *d* the diaper dosage (percent by weight of cement), *w/c* the water-to-cement ratio, *a, u, Q*, and *n* as used previously.

In order to utilize Eq. (6.3) to illustrate the applicability of shredded waste diapers, it is convenient to employ it to create contour plots of the average concentration of hazardous chemicals in combined mixing water, $b_{avg}$, as a function of *d* and *w/c*. The legal framework of application is then presented as various sets of *d* and *w/c*, residing in an area confined by the isolines (i.e., lines of constant value) obtained from relevant standards. An average dry diaper weight of 41 g [251] and an average urine output of 161 g per diaper [220] are used in the computations. The average concentration of hazardous chemicals in urine is extracted from [236].

Fig. 6.5 presents the contour plot of $b_{avg}$ for chloride, in ppm, by color gradients and isolines for diaper dosages *d*, up to 5% in cement composites with water-cement ratios *w/c*, between 0.2 and 0.6. The *w/c* is represented on the horizontal axis and *d* on the vertical axis. The average chloride content rises exponentially by lowering the water-cement ratio while it peaks up linearly when increasing the diaper dosage.
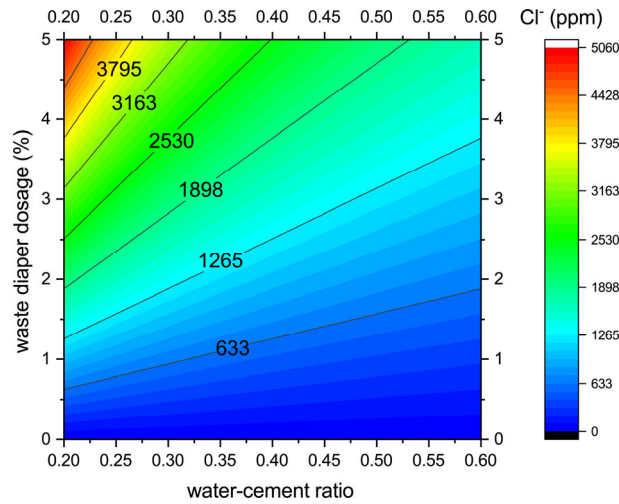
**Figure 6.5:** Average concentration of chloride as Cl⁻ in combined mixing water in the wake of incorporating shredded waste diapers into a cement composite. Equation 6.3 was used in the computation.
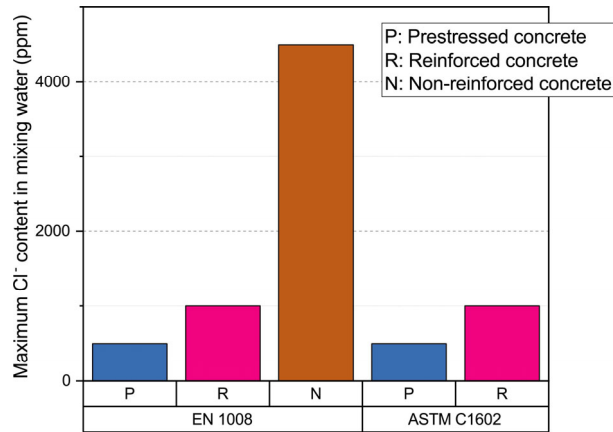


**Figure 6.6:** Maximum limits for the concentration of chloride as Cl⁻ in combined mixing water of three types of concrete, namely prestressed concrete, reinforced concrete, and non-reinforced concrete, according to EN 1008 and ASTM C1602 [239,240].

Fig. 6.6 illustrates the requirements about the maximum allowable chloride concentration, as Cl⁻, in combined mixing water of different concrete types, according to the EN 1008 [239] and the ASTM C 1602 [240]. Both standards limit the maximum concentration of chloride in prestressed and reinforced concrete to 500 ppm and 1000 ppm in water, respectively. However, EN 1008 requires to maintain chloride level below 4500 ppm in non-reinforced concrete, while the ASTM C 1602 has no requirement in this regard.

Replacing the isolines of Fig. 6.5 with the requirements of Fig. 6.6 leads to Fig. 6.7, which presents the legal framework of waste diaper application in concrete concerning chloride concentration. For example, waste diaper dosages of up to 4% at water-cement ratios of

higher than 0.25 may fulfill the requirements of the EN 1008 for chloride content in non-reinforced concrete. On the other hand, while diaper dosage of 3% at $w/c$ of 0.6 may justify the requirements for reinforced concrete, the dosage should be lowered to around 1.5% at $w/c$ of 0.3. It is also worth noting that the isolines of Fig. 6.5 represent the average content of chloride inside a concrete and are well below the legal limits established by the soil quality decree for making unmolded building materials [258].
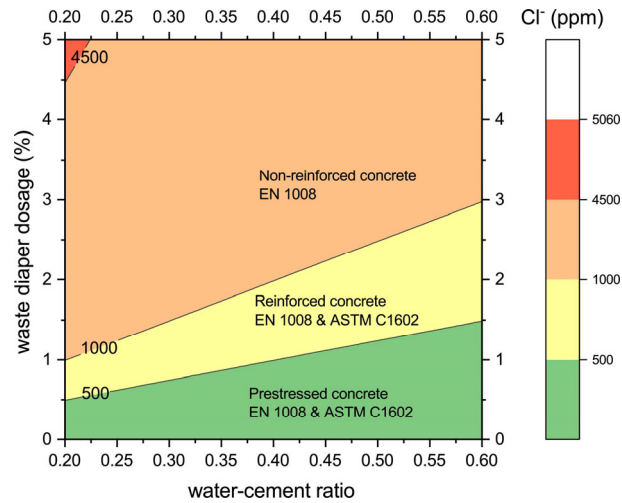


**Figure 6.7:** Legal framework of waste diaper application in concrete concerning chloride concentration.
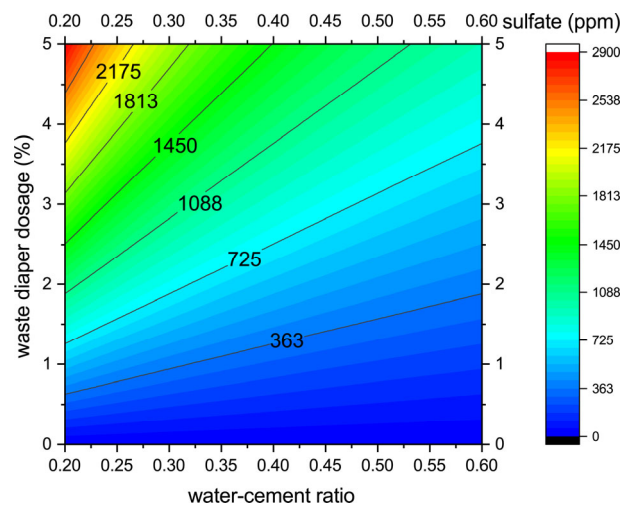


**Figure 6.8:** Average concentration of sulfate in combined mixing water in the wake of incorporating shredded waste diapers into a cement composite. Equation 6.3 was used in the computation.

Fig. 6.8 demonstrates the contour plot of $b_{avg}$ for sulfate, in ppm, by color gradients and isolines for diaper dosages $d$, up to 5% in cement composites with water-cement ratio $w/c$, between 0.2 and 0.6. The maximum limits for the concentration of sulfate in concrete are

summarized in Fig. 6.9. The EN 1008 limits the maximum concentration of sulfate in combined mixing water to 2000 ppm, while the ASTM C 1602 specifies 3000 ppm as compulsory.

In consequence, while diaper dosages of up to 5% at water-cement ratios as low as 0.2 are still within the ASTM C 1602 limits, the diaper dosage may be lowered to 3.5% at similar $w/c$ to comply with the EN 1008. Fig. 6.8 and Fig. 6.9 can also be used to present the legal framework of waste diaper application in concrete concerning sulfate concentration, as used previously in Fig. 6.7. It is also worth highlighting that these quantities are far lower than the allowable limits of the soil quality decree for making unmolded building materials [258].
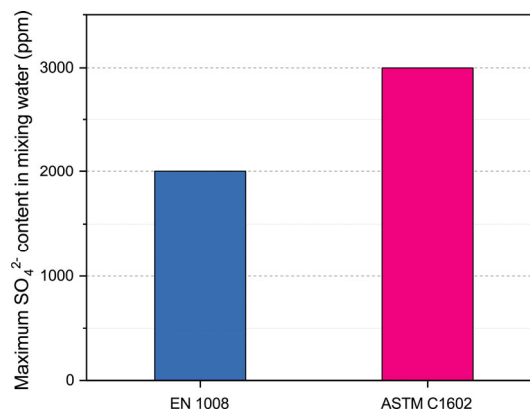


**Figure 6.9:** Maximum limits for the concentration of sulfate, as SO4, in combined mixing water of concrete, according to EN 1008 and ASTM C1602 [239,240].

Urine is a dilute solution of other organic and inorganic compounds, as well [236]. Equation 6.3 can be likewise used to compute their average concentration in the wake of waste diaper incorporation into cement composites. However, as their concentrations are either negligible or non-effective on concrete, they are not studied here. For instance, the $h_{avg}$ of calcium at $w/c = 0.4$ and $d = 1\%$ is as low as 21 ppm.

### 6.3.2    Fresh and hardened properties of cement grouts

As outlined in the Introduction section, cement grouts were one of the two cement composites employed in this study to confirm the viscosity modifying properties of SWDs. Fig. 6.10 compares and contrasts data on the differences in the rheological properties of cement grouts incorporating SWDs. Bingham flow parameters, namely the yield parameter and the Bingham viscosity parameter are shown on the primary and secondary y-axis, respectively. VMAs increase both the yield stress value and the plastic viscosity value of

concrete [171,196]. In general, adding SWDs enhances both the yield and viscosity parameters. More specifically, the rise in the viscosity is significantly higher than that in the yield parameter. For instance, while the viscosity parameter is just under the yield parameter in the reference grout, the value of viscosity rises to more than 2.55 and 2.75 times the yield parameter when adding 0.5% and 1% SWD to cement grouts, respectively.
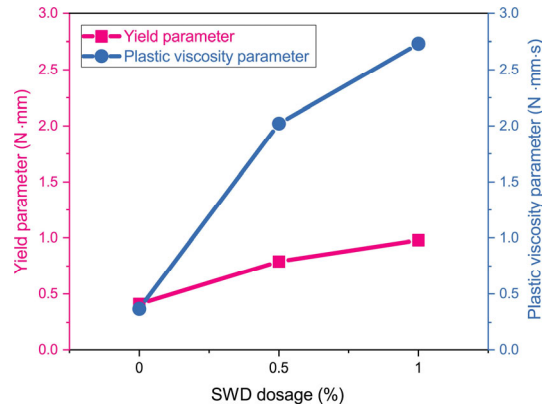


**Figure 6.10:** Influence of SWDs on the rheological properties of cement grouts.
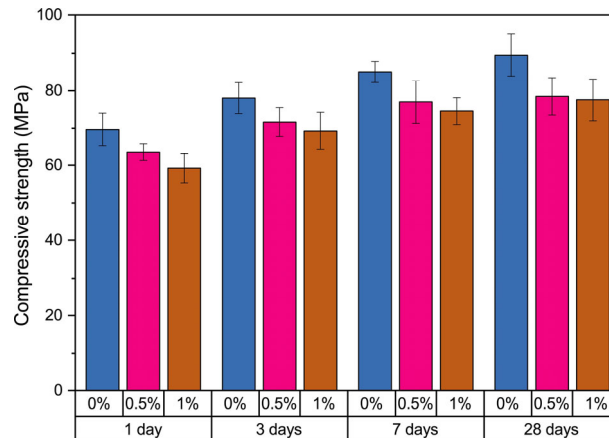


**Figure 6.11:** Influence of SWD content on the average compressive strength of cement grouts. Error bars show the standard deviation.

Fig. 6.11 compares and contrasts data on the average compressive strength of cement pastes incorporating SWDs. Error bars show the standard deviation (SD). In general, adding SWDs slightly decreases the average compressive strength of cement grouts. More specifically, the mean compressive strength of the cement grout with 1% SWD is approximately 12% less than that of the reference at all ages. As the main constituent of diapers is superabsorbent polymer (SAP), the slight decrease in the compressive strength of grouts incorporating SWDs may be attributed to the presence of SAPs in the matrix. These results are consistent

with that obtained in the previous studies on the application of SAPs at the dosage of 0.4 wt.% of cement in cement pastes, reporting a reduction of the early-age and later-age strength of cement pastes by 20% and 10% by adding SAPs, respectively [259]. This trend can be attributed to the fact that the SAP gels are initially filled with water, but as hydration goes on, cement particles absorb the water inside SAP gels, leaving a porous structure similar to that in cement composites having air-entraining agents [260,261].
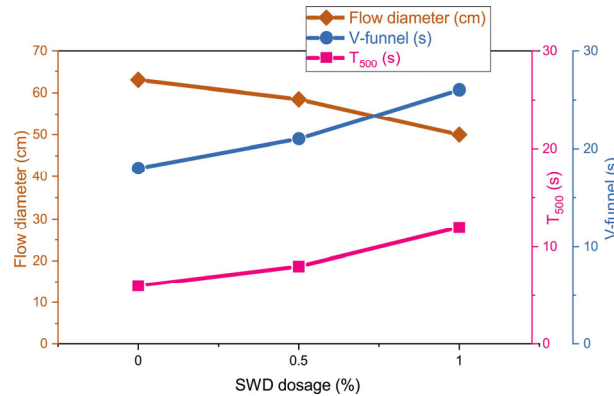


**Figure 6.12:** Effect of SWD on the flow parameters of SCC.

### 6.3.3 Fresh and hardened properties of Self-consolidating concretes (SCCs)

As mentioned previously, in addition to cement grouts, SCCs were utilized to assess the viscosity-modifying performance of SWDs. Fig. 6.12 illustrates the effect of SWDs on three rheological parameters of SCCs, namely flow diameter, V-funnel time, and T500 time. In all cases, adding SWDs increases the flow time (V-funnel or $T_{500}$) and decreases the spread (flow diameter) of the SCCs. The change in the flow parameters of SCCs is similar to what was observed for cement grouts with SWDs in Fig. 6.10

More specifically, as can be seen in Fig. 6.12, the addition of SWDs modifies the slump flow diameters of SCCs. SCCs are classified into three classes of SF1, SF2, and SF3, based on their slump flow, and each class is suitable for a specific category of applications [262]. Hence, adding SWDs can be regarded as a sustainable method to change the application of SCCs. Besides, Fig. 6.12 confirms that SWDs modify both the v-funnel time and T500 of SCCs. Both of these tests are used to appraise the filling ability [263] and assess the viscosity of SCCs indirectly [262]. The adjustments in the viscosity and the yield stress of SCCs are in agreement with the rheological properties of cement grouts shown in Fig. 6.10 where the SWDs modify viscosity more significantly than the yield parameter. For instance, while

incorporating 1% SWD to SCC increases V-funnel and $T_{500}$ time 100% and 44%, respectively, it only reduces flow time 20%. These characteristics confirm a viscosity modifying effect, validating the applicability of SWDs as viscosity modifying admixture for self-consolidating concretes.

The average compressive strength of self-consolidating concretes (SCCs) proportioned with SWDs at 7 and 28 days is shown in Fig. 6.13. The error bars show the standard deviation (SD). The results show that SWDs do not influence the compressive strength of SCCs at the dosages used in this study. This effect may be attributed to the two contradicting influences of SAPs inside the SWDs. On the one hand, they absorb the free water inside SCCs, provide internal curing, and reduce the relative water to cement ratio, leading to a higher value of compressive strength. On the other hand, they produce small water reservoirs that are converted to small cavities inside the matrix after hydration, resulting in a lower value of strength [264].
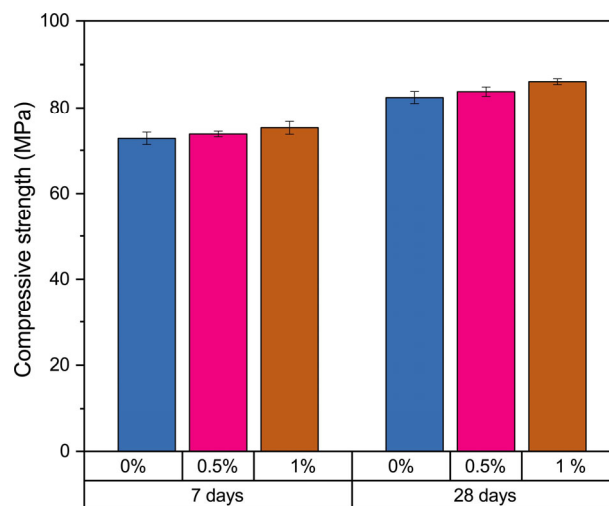


**Figure 6.13:** Influence of SWD dosage on the average compressive strength of SCCs. Error bars show the standard deviation.

## 6.4    Discussion

The results indicate that shredded waste diapers (SWDs) modify the rheological properties of cement pastes and self-consolidating concrete. The category of additives that increase yield stress value, plastic viscosity and apparent viscosity of cement composites are referred to as viscosity modifying admixtures (VMAs) [196], viscosity enhancing admixtures (VEAs) [171], or rheology modifiers [265].

The main challenge in recycling and valorization of waste baby diapers is the cost of the process. From an economical point of view, a recycling process usually consists of five steps: (1) collection; (2) shredding; (3) sterilization; (4) sophisticated separation technology; (5) secondary waste treatment. Valorization of the shredded waste diapers in concrete only involves the first two steps of collection and shredding and eliminates the need for the other three more expensive steps, resulting in higher added value. On the other hand, the technological gap between developing and developed countries has resulted in the implementation of recycling technologies only in developed countries [228]. Developing countries only rely on landfilling or incineration for waste diaper disposal. The higher added value can be used to create jobs in developing societies in sectors related to the collection and shredding of diapers for valorization in concrete. From an environmental point of view, waste baby diapers require over half a millennium for full degradation in landfills, and incineration would produce hazardous ashes containing heavy metals and dioxin [228,266]. Valorization of SWDs in concrete may alleviate these environmental problems.

The main ingredients of concrete are water, binder (e.g., Portland cement), and filler (i.e. aggregates). A large number of waste materials that contain large quantities of silicon and calcium have already been valorized as supplementary cementitious materials (SCMs) in concrete [267,268]. These include industrial by-products and wastes (e.g., silica fume, fly ash, waste glass, and slag) and agricultural waste (e.g., wood waste ash, bagasse ash, bamboo leaf ash, rice husk ash, and corn cob ash) and water treatment sludge [269]. Besides, a vast number of materials that have reasonable strength or can be used to make aggregates and are stable in cement environments such as plastic waste [270], dimensional stone waste [271], steel slag [272], and water treatment sludge [269] have already been valorized as aggregates in concrete. Valorization of waste diaper in concrete differs from these waste valorization methods in that it does not target binder and filler, but it aims at the available water for mixing inside concrete.

When SAPs are used as internal curing admixtures, the swelling capacity predicts the internal water for curing after setting. The swelling capacity can be determined from the filtration test. However, because the situation inside the mixture is different than the test, the swelling capacity has to be modified to keep the consistency of a mixture constant. For example, in the study by De Meyst et al. [273], the added water had to be 1.5 times the swelling capacity in cement filtrate to keep the consistency of the mortar mixtures constant.

Baby diapers consist of SAPs, fluff pulp, and nonwoven fabric. As SAPs are the main absorbing constituent of baby diapers and the main driver of the 44% baby diaper weight reduction in recent years [274], the working mechanism of a diaper is mainly dominated by the swelling action of SAPs. Consequently, part of the rheology modifying performance of SWDs is thanks to swollen SAPs while another part is thanks to the fluff pulp and nonwoven fabric. The fluff pulp modifies rheological properties by water absorption and bridging flocculation. The physical presence and size of shredded nonwoven fabric modify the rheological parameters, too. It is also worth noting that the percentage of SAP, fluff pulp, and nonwoven fabric in diapers differs from one manufacturer to another. Furthermore, some manufacturers use superabsorbent fibers in their products. These variabilities in the ingredients of SWDs make the filtration test less suitable for accurate prediction of the change in the rheology of the mixtures incorporating SWDs.

VMAs increase both the yield stress value and the plastic viscosity value of concrete [171,196]. As shown in Fig. 6.10, the rise in the viscosity is significantly higher than that in the yield parameter. For instance, while the viscosity parameter is just under the reference grout's yield parameter, the viscosity value rises to more than 2.55 and 2.75 times the yield parameter when adding 0.5% and 1% SWD to cement grouts, respectively. A similar trend is evident in Fig. 6.12 in the flow parameters of SCCs. The adjustments in the viscosity and the yield stress of SCCs are in agreement with the rheological properties of cement grouts shown in Fig. 6.10 where the SWDs modify viscosity more significantly than the yield parameter. For instance, while incorporating 1% SWD into SCC increases V-funnel and $T_{500}$ time 100% and 44%, respectively, it only reduces flow time 20%.

Fig. 6.14 illustrates the morphology of the macropores developed by SWDs inside polished samples of hardened cement grouts, performed by a FEI quanta 600 environmental scanning electron microscope (ESEM). Micrographs were recorded by both secondary and backscattering electron detectors (MIX mode) at 5 kV with a spot of 3.0. During the mixing, superabsorbent polymers inside SWDs absorb water and swell. After setting, the swelling of SWDs results in local macropores containing water inside hardened cement grouts that provide internal water reservoirs for cement hydration. Later, these water reservoirs are dried and form small cavities inside the matrix after hydration.
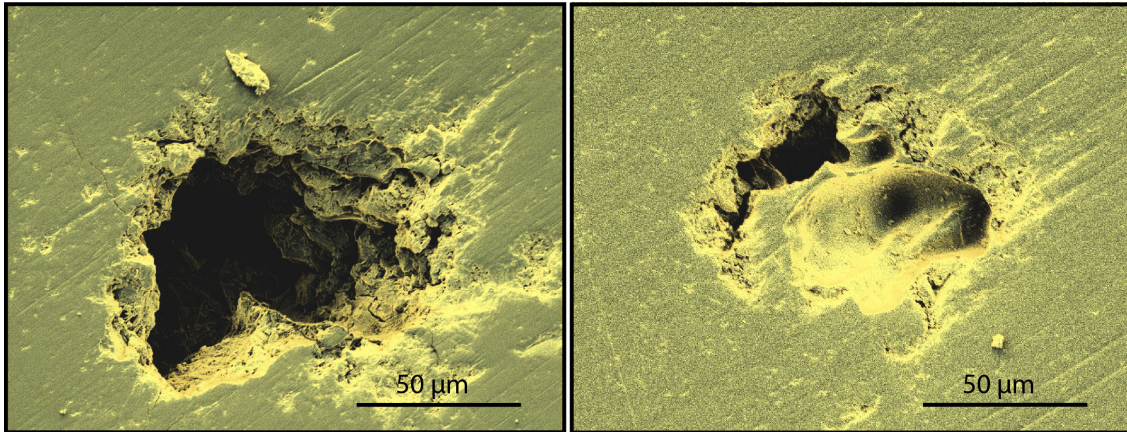
**Figure 6.14:** Morphology of the macropores developed by SWDs inside hardened cement grouts.

As mentioned before, baby diapers consist of SAPs, fluff pulp, and nonwoven fabric. In order to assess the possible influence of these constituents on the pore structure of the cement grouts, mercury intrusion porosimetry (MIP) was performed. It is worth noting that MIP does not measure the macropores that are typically formed by the SAPs and other techniques such as air void analysis (AVA) are more appropriate for that purpose. Fig. 6.15 presents the pore size distribution of cement grouts containing different dosages of SWDs, performed by an AutoPore IV mercury porosimeter. The samples had a particle size of 2-4 mm. Before testing, samples were dried in the oven at 60°C for 48 h. The tests were performed at the pressure range of 0.7 mPa to 227.5 MPa. The contact angle and surface tension of mercury were 130° and 485 mN/m, respectively. The graph confirms that the influence of SWD on porosity of the matrix is local and it does not influence the pore structure of the surrounding matrix significantly.

The applicability study in Sec. 6.3.1, presents a computational model and applies it to formulate the average content of destructive ions in cement composites with different water-cement ratios and diaper dosages. In view of the fact that the main focus of this research is the change in the rheological behavior of cement composites thanks to the water uptake by baby diapers, SWDs are used at the maximum dosage of 1% of cement weight. This dosage is appropriate for reinforced concrete. On the other hand, the applicability study paves the way to apply SWDs at higher dosages by presenting appropriate dosages in the other types of concrete. Given the fact that SAPs, which are the main absorbing constituent of SWDs, have been employed to manufacture air-entrained concrete [260], frost-resistant concrete [261], or fire-resistant concrete [275], further work may be performed to develop new types of concrete with SWDs.
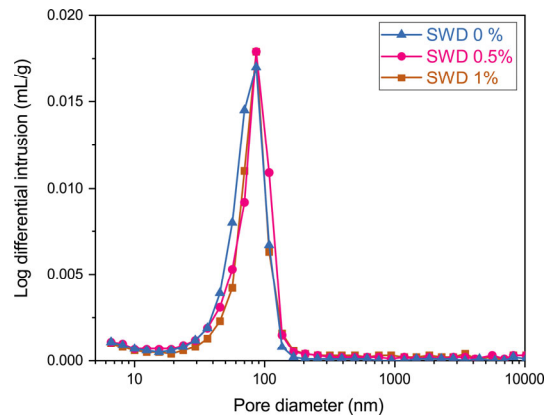
**Figure 6.14:** Pore size distribution of cement grouts containing different dosages of SWD, measured by MIP.

As mentioned previously in Section 6.2.1, urine is a dilute solution of salts in which sodium chloride is the most concentrated. Consequently, sodium chloride solution has been adopted by standards organizations such as ISO and EDANA for characterizing the urine absorbency under pressure, fluid retention, and free swell capacity. As the aim of this study was characterizing the applicability of SWDs as a VMA in cement composites, and since this property is a combination of swelling and fluid retention under pressure, similar to the above-mentioned standards, sodium chloride was utilized in the study. However, it is arguable that the dilute salts inside urine may act differently than the adopted model. Further studies may include other salts and organic compounds to analyze their influence.

The computational model only considers diapers wetted by urine and does not include diapers containing feces. Furthermore, urine contains bacteria, viruses, and pathogens. These harmful microorganisms may be one of the main concerns about incorporating SWDs into cement composites. Although studies showed that the high pH of cement composites kills dangerous microbes [231–234], further research may include urine in SWDs to assess the level of disinfection.

## 6.5    Conclusions

This chapter introduces an innovative mindset towards waste baby diapers. They are not only not detrimental to cement composites but also useful in terms of modifying the viscosity of cement grout and concrete. The article develops a systematic study by proposing a computational model, applying the model, and validating the idea by two cement composite systems. Based on the obtained results, the following conclusions have been reached:

- A model is proposed that computes the average concentration of chemicals in combined mixing water of a cement composite in the wake of incorporating shredded waste diaper. The model is combined with the relevant standards to present a legal framework about the applicability of waste diapers in different types of concrete.

- The appropriate dosages of the waste diaper in concrete depend on the type of concrete, water-cement ratio, and the waste diaper dosage. Waste diaper dosages as high as 5% in non-reinforced concrete at water-cement ratios ranging from 0.25 to 0.6 and as high as 2% in reinforced concrete at water-cement ratios ranging from 0.4 to 0.6 can be used.

- Shredded waste diapers (SWDs) modify the rheological behavior of cement grouts and concrete by enhancing the yield stress and viscosity and can be classified as a sustainable source for producing highly effective VMAs in the concrete industry. A maximum SWD dosage of 1% showed an excellent rheological effect on self-consolidating concrete (SCC) with no effect on its compressive strength.

- Shredded waste diapers (SWDs) affect the pore structure locally by producing water reservoirs but do not affect the pore structure of the surrounding matrix significantly.

# Conclusions and recommendations

This dissertation has provided a deeper insight into the design and use of innovative admixtures for tackling shortcomings of cement composites in terms of volume change and rheological behavior. The insights gained from this dissertation are summarized below.

## 7.1 Conclusions

### 7.1.1 Mixture design method for pumpable low shrinkage flowing concrete

The first step in enhancing the rheological behavior and volume change of cement composites is to start with a well-founded mix design method. The findings of Chapter 2 reveals that the modified A&A model optimizes the particle size distribution of concrete to produce pumpable concrete according to the ACI 211.9R-18 [70]. The findings also show that the modified A&A model at a distribution modulus of 0.35 is the boundary limit for ideal pumpability. A distribution modulus smaller than 0.35 results in ideal-for-pumping mixtures. The well-grounded theoretical background of the modified A&A model makes it possible to optimize pumpability for each application. The choice of distribution modulus depends on the application for which the concrete mixture is designed: (1) between 0.35 and 0.27 is suitable for flowing concrete, (2) between 0.30 and 0.25 is suitable for self-consolidating concrete, and (3) lower than 0.25 is suitable for ultra-high-performance concrete. A greater distribution modulus of the modified A&A model results in a greater coarse-to-fine aggregate ratio in the mixture. It also reduces the shrinkage of the mixture.

### 7.1.2 Rapidly expansive magnesia to modify volume change

Research on the application of magnesia in concrete has been mostly restricted to the use of slow-hydrating magnesia for compensating cooling shrinkage of concrete. The experimental investigation in Chapter 3 reveals that the rapidly expansive magnesia has small average crystallite size (i.e. 8.1 nm) and negligible concentration of sintering oxides such as $Fe_2O_3$, $SiO_2$, and $Al_2O_3$. The small crystallite sizes and non-sintered morphology of rapidly expansive magnesia causes a large pore volume contained in uniform small pore sizes with high surface area. The physisorption isotherm of this magnesia is of Type-IV and has high surface energy. The shrinkage after seven days of water curing in concrete samples containing rapidly expansive magnesia can be well captured with a logarithmic model. The slope of the fitted model in concretes samples containing rapidly expansive magnesia proportioned with CEM I and CEM III is in the same range (-200±10). On the contrary, the cooling shrinkage magnesia has greater average crystallite size (21.1 nm) and concentration of sintering oxides. It does not produce expansion at the early age in cement composites.

### 7.1.3 Homogeneity and thermal history of light-burnt magnesia by surface properties

Thermal history and homogeneity of light-burnt magnesia must be reliably detected before application. The combination of surface properties and experimental investigation in Chapter 4 leads to a new technique for accelerated thermal history analysis of light-burnt magnesia. The method provides an equation for computing the weighted mesopore probability distribution of LBM and analyzing the peaks present in the distribution to examine homogeneity and thermal history. The properties of each peak are calculated by deconvoluting the distribution by Lorentz peak functions and reiterating peak deconvolution using the Levenberg Marquardt algorithm. This approach is able to identify and quantify thermal history of light-burnt magnesia. It gives the number of fractions of a heterogeneous sample of magnesia from the number of peaks, the calcination temperature of each fraction from the center the Lorentz fit of that fraction, and the percentage of each fraction from the area of their Lorentz fit in the weighted mesopore probability distribution.

### 7.1.4 Milled paper pulp to modify rheological behavior

A combination of hydrophilic properties and the hierarchical structure of paper pulp are used to introduce an innovative viscosity modifying admixture (VMA) for cement composites in Chapter 5. Two different levels of fineness are obtained by mechanical milling of the same source of paper pulp. The experimental investigation reveals that the milled paper pulp, made by both mechanical milling procedures, modifies the rheology of cement grouts and can be categorized as a sustainable VMA. The viscosity-modifying mechanism of action of paper pulp in cement grouts is a combination of bridging flocculation and swelling. High-energy milled paper pulp (HPP) consists mostly of the ultrafine fibers of the hierarchical structure of paper pulp and enhances both the plastic Bingham viscosity and dynamic yield stress of cement grouts more significantly than low-energy milled paper pulp (LPP). The range of the rheological effect of HPP on cement grouts is analogous to that of diutan gum at similar dosages. However, the ratio of the plastic viscosity to the yield stress in HPP is more significant than that of diutan gum grouts.

The influence of the low-energy milled paper pulp (LPP) on the rheological behavior of cement grouts differs from that of the high-molecular-weight synthetic copolymer (MM) in that while the LPP mainly increases the plastic viscosity, the synthetic copolymer primarily changes the yield stress. The c-parameter of a second-order modified Bingham model is proposed to take the differences in the nonlinearity of grouts into account. While LPP and the high-molecular-weight synthetic copolymer (MM) do not influence the c-parameter of the cement grout, both HPP and diutan gum affect it significantly. Contrary to diutan gum that increases the c-parameter, HPP decreases it and makes its value negative. This change in sign of the c-parameter is an indicator that the true dynamic yield stress of the HPP grouts is lower than what obtained from the Bingham model. Both LPP and HPP do not affect the hydration kinetics and setting time. Besides, they both show good stability in a highly alkaline environment.

Welch's ANOVA confirms a significant difference in average compressive strength of mortars with paper pulp with that of the reference. Games-Howel post hoc test shows that both LPP and HPP increase the 1-day and 7-day compressive strength of the mortars, compared to the reference. After 28 days the significance of the difference between the compressive strength of reference mortars with that of LPP mortars fades but HPP mixtures continue to have higher compressive strength. A similar analysis shows that milled paper pulp does not affect the flexural strength of mortars, at the dosages used for flow adjustment.

**7.1.5    Waste baby diapers to modify rheological behavior**

Chapter 6 introduces an innovative mindset towards waste baby diapers. They are not only not detrimental to cement composites but also useful in terms of modifying the viscosity of cement grout and concrete. A model is proposed that computes the average concentration of chemicals in combined mixing water of a cement composite in the wake of incorporating shredded waste diaper. The model is combined with the relevant standards to present a legal framework about the applicability of waste diapers in different types of concrete.

The appropriate dosages of the waste diaper in concrete depend on the type of concrete, water-cement ratio, and the waste diaper dosage. Waste diaper dosages as high as 5% in non-reinforced concrete at water-cement ratios ranging from 0.25 to 0.6 and as high as 2% in reinforced concrete at water-cement ratios ranging from 0.4 to 0.6 can be used. Shredded waste diapers (SWDs) modify the rheological behavior of cement grouts and concrete by enhancing the yield stress and viscosity and can be classified as a sustainable source for producing highly effective VMAs in the concrete industry. A maximum SWD dosage of 1% showed an excellent rheological effect on self-consolidating concrete (SCC) with no negative effect on its compressive strength. Shredded waste diapers (SWDs) affect the pore structure locally by producing water reservoirs but do not affect the pore structure of the surrounding matrix significantly.

## 7.2    Recommendations

This dissertation systematically investigated two strategies to modify viscosity and volume change of cement composites: (1) mix design method, and (2) admixtures. The mix design strategy confirmed that the modified A&A model designs low-shrinkage flowing concretes and proposed proper parameters for pumpability. The admixtures strategy resulted in the successful introduction of three innovative admixtures for compensating shrinkage and modifying viscosity. However, some open questions require future research:

- The modified A&A model maximizes particle packing and enhances flowability. Further research is needed to identify the influence of the deviation from the target line on particle packing and flowability. Similarly, despite the promising results regarding the pumpability of the modified A&A model, questions remain about the influence of the deviation from the target line on the pumpability.

- The rapidly expansive magnesia produces expansion at early age and compensates shrinkage. There is room for further progress in determining the influence of curing

128

temperature on its performance. In addition, in further research, the durability of the concrete incorporating rapidly expansive magnesia should be investigated.

- The weighted mesopore probability distribution by Lorentz peak functions is a cost-effective detection tool that avoids cracking in concrete structures by detecting inhomogeneities in light-burnt magnesia. As the pseudomorphous structure of calcined magnesia provides the foundation of this method, the proposed method can be applied to a wide range of pseudomorphous materials to detect inhomogeneities, as well. However, some questions remain unanswered at present. This study only analyzed the light-burnt magnesia produced by calcining magnesite. The magnesia produced by calcining other magnesium compounds such as brucite has a different pore structure [38]. Furthermore, the presence of some gases, such as water vapor, may significantly influence the structure of calcination products [44]. In addition, the presence of impurities in the parent solid may promote sintering [20]. Further research may therefore include the influence of parent solid, impurities in the parent solid, and the calcination atmosphere to provide calibration curves for the method presented here.

- Milled paper pulp modifies the rheology of cement composites and can be used as a viscosity modifying admixture. When milled paper pulp is used at low dosages as a rheology modifier, its durability in highly alkaline environments may not be important. There is abundant room for further progress in determining the durability of milled paper pulp in cement composites as it can promote its application to higher dosages and as a bio-reinforcement in cement composites.

- Waste baby diapers are used at low dosages as a rheology modifier. The model introduced in this thesis paves the way to apply shredded waste diapers at higher dosages. Given the fact that SAPs, which are the main absorbing constituent of waste diapers, have been employed to manufacture air-entrained concrete [260], frost-resistant concrete [261], or fire-resistant concrete [275], further work may be performed to develop new types of concrete with SWDs. The computational model only considers diapers wetted by urine and does not include diapers containing feces. Furthermore, urine contains bacteria, viruses, and pathogens. These harmful microorganisms may be one of the main concerns about incorporating SWDs into cement composites. Although studies showed that the high pH of cement composites kills dangerous microbes [231–234], further research may include urine in SWDs to assess the level of disinfection.

# Bibliography

[1]     K. Sobolev, M. Ferrada Gutiérrez, T.A.C. Society, How Nanotechnology Can Change the Concrete World, in: Prog. Nanotechnol., John Wiley & Sons, Inc., Hoboken, NJ, USA, 2014: pp. 113–116. https://doi.org/10.1002/9780470588260.ch16.

[2]     F. Sanchez, K. Sobolev, Nanotechnology in concrete - A review, Constr. Build. Mater. 24 (2010) 2060–2071. https://doi.org/10.1016/j.conbuildmat.2010.03.014.

[3]     A.M. Neville, J.J. Brooks, Concrete technology, Prentice Hall, 2010.

[4]     A.M. Neville, Properties of concrete, Pearson, 2011.

[5]     F. de Larrard, Concrete mixture proportioning: A scientific approach, E & FN Spon, London, 1999.

[6]     P. Goltermann, L. Palbøl, V. Johansen, Packing of Aggregates: An Alternative Tool to Determine the Optimal Aggregate Mix, ACI Mater. J. 94 (1998). https://doi.org/10.14359/328.

[7]     M.R. Jones, L. Zheng, M.D. Newlands, Comparison of particle packing models for proportioning concrete constitutents for minimum voids ratio, Mater. Struct. 2002 355. 35 (2002) 301–309. https://doi.org/10.1007/BF02482136.

[8]     B.R. Carpenter, J.B. Bloys, L.D. Johnson, Cement composition, Cem. Concr. Compos. 22 (2000) 311. https://doi.org/10.1016/S0958-9465(00)80010-4.

[9]     G. Gelardi, S. Mantellato, D. Marchon, M. Palacios, A.B. Eberhardt, R.J. Flatt, Chemistry of chemical admixtures, in: Sci. Technol. Concr. Admixtures, Elsevier, 2015: pp. 149–218. https://doi.org/10.1016/B978-0-08-100693-1.00009-6.

[10]    J. Schulze, H. Baumgartl, Shrinkage-reducing agent for cement, 1988.

[11]    N.S. Berke, M.P. Dallaire, Drying shrinkage cement admixture, US5622558 A, 1995. https://www.google.ch/patents/US5622558.

[12]    F. Wombacher, T.A. Bürge, U. Mäder, Method of reducing the shrinkage of hydraulic binders, EP1024120 B1, 2012.

[13]    T. Goto, T. Sato, K. Sakai, M. Ii, Cement shrinkage reducing agent and cement composition, US4547223 A, 1985.

[14]    S. Akimoto, S. Honda, T. Yasukohchi, Additives for cement, US4946904 A, 1990. https://www.google.com/patents/US4946904.

[15]    ACI Committee 223, ACI 223R-10 Guide for the Use of Shrinkage-Compensating Concrete, American Concrete Institute, Farmington Hills, 2010.

[16] ACI Committee 212, ACI 212.3R-16 Report on Chemical Admixtures for concrete, American Concrete Institute, Farmington Hills, 2016.

[17] N.P. Mailvaganam, Miscellaneous Admixtures, in: Concr. Admixtures Handb., Elsevier, 1996: pp. 939–1024. https://doi.org/10.1016/B978-081551373-5.50019-2.

[18] O.M. Jensen, P.F. Hansen, Water-entrained cement-based materials: II. Experimental observations, Cem. Concr. Res. 32 (2002) 973–978. https://doi.org/10.1016/S0008-8846(02)00737-8.

[19] O.M. Jensen, P.F. Hansen, Water-entrained cement-based materials - I. Principles and theoretical background, Cem. Concr. Res. 31 (2001) 647–654. https://doi.org/10.1016/S0008-8846(01)00463-X.

[20] M. Collepardi, R. Troli, M. Bressan, F. Liberatore, G. Sforza, Crack-free concrete for outside industrial floors in the absence of wet curing and contraction joints, Cem. Concr. Compos. 30 (2008) 887–891. https://doi.org/10.1016/j.cemconcomp.2008.07.002.

[21] ACI, CT-18 ACI Concrete Terminology, American Concrete Institute, Farmington Hills, 2018. www.concrete.org.

[22] ASTM subcommittee C09.23, ASTM C1017 / C1017M - 13e1 Standard Specification for Chemical Admixtures for Use in Producing Flowing Concrete, (2013) 9. https://doi.org/10.1520/C1017_C1017M-13E01.

[23] L. Mo, M. Deng, M. Tang, Effects of calcination condition on expansion property of MgO-type expansive agent used in cement-based materials, Cem. Concr. Res. 40 (2010) 437–446. https://doi.org/10.1016/j.cemconres.2009.09.025.

[24] W.R. Eubank, Calcination Studies of Magnesium Oxides, J. Am. Ceram. Soc. 34 (1951) 225–229. https://doi.org/10.1111/j.1151-2916.1951.tb11644.x.

[25] DL/T 5296-2013, Technical Specification of Magnesium Oxide Expansive for Use in Hydraulic Concrete, 2013.

[26] L. Mo, J. Fang, W. Hou, X. Ji, J. Yang, T. Fan, H. Wang, Synergetic effects of curing temperature and hydration reactivity of MgO expansive agents on their hydration and expansion behaviours in cement pastes, Constr. Build. Mater. 207 (2019) 206–217. https://doi.org/10.1016/j.conbuildmat.2019.02.150.

[27] X. Chen, H.Q. Yang, W.W. Li, Factors analysis on autogenous volume deformation of MgO concrete and early thermal cracking evaluation, Constr. Build. Mater. 118 (2016) 276–285. https://doi.org/10.1016/j.conbuildmat.2016.02.093.

[28] S.A. Walling, J.L. Provis, Magnesia-Based Cements: A Journey of 150 Years, and Cements for the Future?, Chem. Rev. 116 (2016) 4170–4204. https://doi.org/10.1021/acs.chemrev.5b00463.

[29] M.A. Shand, The Chemistry and Technology of Magnesia, John Wiley & Sons, Inc., Hoboken, NJ, USA, 2006. https://doi.org/10.1002/0471980579.

[30] B. Matković, S. Popovic, V. Rogić, T. Žunić, J.F. Young, Reaction Products in Magnesium Oxychloride Cement Pastes. System $MgO-MgCl_2-H_2O$, J. Am. Ceram. Soc. 60 (1977) 504–507. https://doi.org/10.1111/J.1151-2916.1977.TB14093.X.

[31] F.C. Harper, Effect of calcination temperature on the properties of magnesium

oxides for use in magnesium oxychloride cements, J. Appl. Chem. 17 (1967) 5–10. https://doi.org/10.1002/jctb.5010170102.

[32]   S. Alegret, M. Blanco, R. Subirats, Potentiometric Study of the Reactivity of Calcined Magnesites for Use in Magnesium Oxychloride Cements, J. Am. Ceram. Soc. 67 (1984) 579–582. https://doi.org/10.1111/j.1151-2916.1984.tb19597.x.

[33]   K. Hirota, N. Okabayashi, K. Toyoda, O. Yamaguchi, Characterization and sintering of reactive MgO, Mater. Res. Bull. 27 (1992) 319–326. https://doi.org/10.1016/0025-5408(92)90061-4.

[34]   M.G. Kim, U. Dahmen, A.W. Searcy, Structural Transformations in the Decomposition of $Mg(OH)_2$ and $MgCO_3$, J. Am. Ceram. Soc. 70 (1987) 146–154. https://doi.org/10.1111/j.1151-2916.1987.tb04949.x.

[35]   J. Zhu, N. Ye, J. Liu, J. Yang, Evaluation on hydration reactivity of reactive magnesium oxide prepared by calcining magnesite at lower temperatures, Ind. Eng. Chem. Res. 52 (2013) 6430–6437. https://doi.org/10.1021/ie303361u.

[36]   C.K. Chau, Z. Li, Accelerated reactivity assessment of light burnt magnesium oxide, J. Am. Ceram. Soc. 91 (2008) 1640–1645. https://doi.org/10.1111/j.1551-2916.2008.02330.x.

[37]   A. Blanco, C. Negro, C. Monte, E. Fuente, J. Tijero, The Challenges of Sustainable Papermaking, Environ. Sci. Technol. 38 (2004) 414A-420A. https://doi.org/10.1021/es040654y.

[38]   P. Berg, O. Lingqvist, Pulp, Paper, and packaging in the next decade: Transformational change, McKinsey Co. Pap. For. Prod. (2017) 1–18.

[39]   P. Bajpai, Uses of Recovered Paper Other than Papermaking, Recycl. Deinking Recover. Pap. (2014) 283–295. https://doi.org/10.1016/B978-0-12-416998-2.00016-7.

[40]   D. Gavrilescu, Energy from biomass in pulp and paper mills, Environ. Eng. Manag. J. 7 (2008) 537–546.

[41]   C. Correia, S. Francisco, R. Soares, H. Savastano, Nanofibrillated cellulose and cellulosic pulp for reinforcement of the extruded cement based materials, Constr. Build. Mater. 160 (2018) 376–384. https://doi.org/10.1016/j.conbuildmat.2017.11.066.

[42]   E.F. Campello, M. V. Pereira, F.A. Darwish, K. Ghavami, On the Fatigue Behavior of Bamboo Pulp Reinforced Cementitious Composites, Procedia Struct. Integr. 2 (2016) 2929–2935. https://doi.org/10.1016/j.prostr.2016.06.366.

[43]   C. De Souza Rodrigues, K. Ghavami, P. Stroeven, Porosity and water permeability of rice husk ash-blended cement composites reinforced with bamboo pulp, in: J. Mater. Sci., Kluwer Academic Publishers-Plenum Publishers, 2006: pp. 6925–6937. https://doi.org/10.1007/s10853-006-0217-2.

[44]   R.S.P. Coutts, Y. Ni, B.C. Tobias, Air-cured bamboo pulp reinforced cement, J. Mater. Sci. Lett. 13 (1994) 283–285. https://doi.org/10.1007/BF00571777.

[45]   M. Khorami, E. Ganjian, A. Srivastav, Feasibility Study on Production of Fiber Cement Board Using Waste Kraft Pulp in Corporation with Polypropylene and Acrylic Fibers, Mater. Today Proc. 3 (2016) 376–380.

https://doi.org/10.1016/j.matpr.2016.01.023.

[46]	G.H.D. Tonoli, R.F. Mendes, G. Siqueira, J. Bras, M.N. Belgacem, H. Savastano, Isocyanate-treated cellulose pulp and its effect on the alkali resistance and performance of fiber cement composites, Holzforschung. 67 (2013) 853–861. https://doi.org/10.1515/hf-2012-0195.

[47]	M. Khorami, E. Ganjian, The effect of limestone powder, silica fume and fibre content on flexural behaviour of cement composite reinforced by waste Kraft pulp, Constr. Build. Mater. 46 (2013) 142–149. https://doi.org/10.1016/j.conbuildmat.2013.03.099.

[48]	B.J. Mohr, J.J. Biernacki, K.E. Kurtis, Supplementary cementitious materials for mitigating degradation of kraft pulp fiber-cement composites, Cem. Concr. Res. 37 (2007) 1531–1543. https://doi.org/10.1016/j.cemconres.2007.08.001.

[49]	N.H. El-Ashkar, H. Nanko, K.E. Kurtis, Effect of Moisture State on Mechanical Behavior and Microstructure of Pulp Fiber-Cement Mortars, J. Mater. Civ. Eng. 19 (2007) 691–699. https://doi.org/10.1061/(ASCE)0899-1561(2007)19:8(691).

[50]	B.J. Mohr, J.J. Biernacki, K.E. Kurtis, Microstructural and chemical effects of wet/dry cycling on pulp fiber–cement composites, Cem. Concr. Res. 36 (2006) 1240–1251. https://doi.org/10.1016/j.cemconres.2006.03.020.

[51]	M.M. Shokrieh, A. Mahmoudi, H.R. Shadkam, Hybrid polyvinyl alcohol and cellulose fiber pulp instead of asbestos fibers in cement-based composites, Mech. Compos. Mater. 51 (2015) 231–238. https://doi.org/10.1007/s11029-015-9494-7.

[52]	J. Claramunt, M. Ardanuy, L.J. Fernandez-Carrasco, Wet/Dry Cycling Durability of Cement Mortar Composites Reinforced with Micro- and Nanoscale Cellulose Pulps, BioResources. 10 (2015) 2681–2685. https://doi.org/10.1021/bi00834a066.

[53]	J.E.M. Ballesteros, S.F. Santos, G. Mármol, H. Savastano, J. Fiorelli, Evaluation of cellulosic pulps treated by hornification as reinforcement of cementitious composites, Constr. Build. Mater. 100 (2015) 83–90. https://doi.org/10.1016/j.conbuildmat.2015.09.044.

[54]	G.H. Denzin Tonoli, A.E.F. De Souza Almeida, M.A. Pereira-Da-Silva, A. Bassa, D. Oyakawa, H. Savastano, Surface properties of eucalyptus pulp fibres as reinforcement of cement-based composites, Holzforschung. 64 (2010) 595–601. https://doi.org/10.1515/HF.2010.073.

[55]	G.H.D. Tonoli, H. Savastano, E. Fuente, C. Negro, A. Blanco, F.A. Rocco Lahr, Eucalyptus pulp fibres as alternative reinforcement to engineered cement-based composites, Ind. Crops Prod. 31 (2010) 225–232. https://doi.org/10.1016/j.indcrop.2009.10.009.

[56]	G. Mármol, S.F. Santos, H. Savastano, M.V. Borrachero, J. Monzó, J. Payá, Mechanical and physical performance of low alkalinity cementitious composites reinforced with recycled cellulosic fibres pulp from cement kraft bags, Ind. Crops Prod. 49 (2013) 422–427. https://doi.org/10.1016/j.indcrop.2013.04.051.

[57]	G.H.D. Tonoli, A.P. Joaquim, M.A. Arsne, K. Bilba, H. Savastano, Performance and durability of cement based composites reinforced with refined sisal pulp, Mater. Manuf. Process. 22 (2007) 149–156. https://doi.org/10.1080/10426910601062065.

[58] H. Savastano, P.G. Warden, R.S.P. Coutts, Mechanically pulped sisal as reinforcement in cementitious matrices, Cem. Concr. Compos. 25 (2003) 311–319. https://doi.org/10.1016/S0958-9465(02)00055-0.

[59] R. Hosseinpourpia, P. Hosseini, S.R. Mofidian, R. Hosseinpourpia, A. Varshoee, Influence of Nanosilica on Properties of Green Cementitious Composites Filled with Waste Sulfite Pulp Fiber and Aminosilane, Arab. J. Sci. Eng. 39 (2014) 2631–2640. https://doi.org/10.1007/s13369-013-0935-0.

[60] P. Jongvisuttisun, C. Negrello, K.E. Kurtis, Effect of processing variables on efficiency of eucalyptus pulps for internal curing, Cem. Concr. Compos. 37 (2013) 126–135. https://doi.org/10.1016/j.cemconcomp.2012.11.006.

[61] A. Mezencevova, V. Garas, H. Nanko, K.E. Kurtis, Influence of Thermomechanical Pulp Fiber Compositions on Internal Curing of Cementitious Materials, J. Mater. Civ. Eng. 24 (2012) 970–975. https://doi.org/10.1061/(ASCE)MT.1943-5533.0000446.

[62] R&R Market Research, Global and China Superabsorbent Polymers (SAP) Industry Report, 2014-2018, (2015) 92. http://www.rnrmarketresearch.com/global-and-china-superabsorbent-polymers-sap-industry-report-2014-2018-market-report.html.

[63] U. Arena, F. Ardolino, F. Di Gregorio, Technological, environmental and social aspects of a recycling process of post-consumer absorbent hygiene products, J. Clean. Prod. 127 (2016) 289–301. https://doi.org/10.1016/j.jclepro.2016.03.164.

[64] M. Cordella, I. Bauer, A. Lehmann, M. Schulz, O. Wolf, Evolution of disposable baby diapers in Europe: Life cycle assessment of environmental impacts and identification of key areas of improvement, J. Clean. Prod. 95 (2015) 322–331. https://doi.org/10.1016/j.jclepro.2015.02.040.

[65] A. V. Weisbrod, G. Van Hoof, LCA-measured environmental improvements in Pampers diapers, Int. J. Life Cycle Assess. 17 (2012) 145–153. https://doi.org/10.1007/s11367-011-0343-1.

[66] A. Smith, K. Brown, S. Ogilvie, K. Rushton, J. Bates, Waste management options and climate change: Final report, European Communities, Luxembourg:, 2001. https://doi.org/10.1016/S1352-2310(01)00532-5.

[67] Q. Aguilar-Virgen, P. Taboada-González, S. Ojeda-Benítez, Analysis of the feasibility of the recovery of landfill gas: A case study of Mexico, J. Clean. Prod. 79 (2014) 53–60. https://doi.org/10.1016/j.jclepro.2014.05.025.

[68] R.M. Espinosa-Valdemar, S. Turpin-Marion, I. Delfín-Alcalá, A. Vázquez-Morillas, E.-V.R. María, T.-M. Sylvie, D.-A. Irma, V.-M. Alethia, Disposable diapers biodegradation by the fungus Pleurotus ostreatus, Waste Manag. 31 (2011) 1683–1688. https://doi.org/10.1016/j.wasman.2011.03.007.

[69] R.M. Espinosa-Valdemar, P.X. Sotelo-Navarro, X. Quecholac-Piña, M. Beltrán-Villavicencio, S. Ojeda-Benítez, A. Vázquez-Morillas, Biological recycling of used baby diapers in a small-scale composting system, Resour. Conserv. Recycl. 87 (2014) 153–157. https://doi.org/10.1016/j.resconrec.2014.03.015.

[70] ACI Committee 211, 211.9R-18: Guide to Selecting Proportions for Pumpable Concrete, American Concrete Institute, Farmington Hills, 2018.

[71] P.K. Mehta, P.J.M. Monteiro, Concrete : microstructure, properties, and materials.,

McGraw-Hill, 2006.

[72] R.J. Kosmatka, S.H.; Kerkhoff, B.; Hooton, R. D.; McGrath, Design and control of concrete mixtures - The guide to application, methods, and materials., Portland Cement Association, Washington, D.C., 2011.

[73] ACI Committee 211, ACI 211.1 Standard practice for selecting proportions for normal, heavyweight, and mass concrete, American Concrete Institute, Farmington Hills, 2017.

[74] ACI Committee 309, ACI 309R-05 Guide for consolidation of concrete, American Concrete Institute, Farmington Hills, 2005.

[75] ACI Committee 237, ACI 237R-07 Self-Consolidating Concrete, American Concrete Institute, Farmington Hills, 2007.

[76] K. Khayat, G. De Schutter, eds., Mechanical Properties of Self-Compacting Concrete, Springer International Publishing, 2014. https://doi.org/10.1007/978-3-319-03245-0.

[77] K.H. Khayat, D. Feys, eds., Design, Production and Placement of Self-Consolidating Concrete, Springer, Dordrecht, 2010. https://doi.org/https://doi.org/10.1007/978-90-481-9664-7.

[78] A. Yahia, P.C. Aïtcin, Self-consolidating concrete, in: Sci. Technol. Concr. Admixtures, 2015: pp. 491–502. https://doi.org/10.1016/B978-0-08-100693-1.00026-6.

[79] H.J.H. Brouwers, H.J. Radix, Self-compacting concrete: Theoretical and experimental study, Cem. Concr. Res. 35 (2005) 2116–2136. https://doi.org/10.1016/j.cemconres.2005.06.002.

[80] H.J.H. Brouwers, H.J. Radix, Self-compacting concrete: the role of the particle size distribution, in: SCC'2005-China - 1st Int. Symp. Des. Perform. Use Self-Consolidating Concr., Changsha, Hunan, China, 2005: pp. 109–118. https://doi.org/10.1617/2912143624.01.

[81] W. Schmidt, H.J.H. Brouwers, H.-C. Kühne, B. Meng, The Working Mechanism of Starch and Diutan Gum in Cementitious and Limestone Dispersions in Presence of Polycarboxylate Ether Superplasticizers, Appl. Rheol. 23 (2013). https://doi.org/10.3933/ApplRheol-23-52903.

[82] The Concrete Society, TR34 4th Edition - Concrete industrial ground floors, a guide to design and construction, 2013.

[83] BSI Committee B/502/6, BS EN 12350-5:2010 Testing fresh concrete Flow table test, 2009.

[84] BSI Committee B/517/1, BS EN 206:2013+A1:2016 Concrete. Specification, performance, production and conformity, BSI, 2016.

[85] M.G. Alexander, S. Mindess, Aggregates in concrete, Taylor & Francis, 2008.

[86] N. Roussel, Understanding the Rheology of Concrete, Woodhead Publishing, 2012.

[87] G. Hüsken, A multifunctional design approach for sustainable concrete : with application to concrete mass products (PhD thesis), Eindhoven University of Technology, 2010. https://doi.org/10.6100/IR693348.

[88]     G. Hendrix, D. Trejo, New Mixture Proportioning Method for Flowing Concrete Mixtures, ACI Mater. J. 114 (n.d.). https://doi.org/10.14359/51689894.

[89]     N. Su, B. Miao, A new method for the mix design of medium strength flowing concrete with low cement content, Cem. Concr. Compos. 25 (2003) 215–222. https://doi.org/10.1016/S0958-9465(02)00013-6.

[90]     S. Fataei, E. Secrieru, V. Mechtcherine, N. Roussel, A first-order physical model for the prediction of shear-induced particle migration and lubricating layer formation during concrete pumping, Cem. Concr. Res. 147 (2021) 106530. https://doi.org/10.1016/j.cemconres.2021.106530.

[91]     M. Choi, N. Roussel, Y. Kim, J. Kim, Lubrication layer properties during concrete pumping, Cem. Concr. Res. 45 (2013) 69–78. https://doi.org/10.1016/j.cemconres.2012.11.001.

[92]     M. Hunger, An integral design concept for ecological self-compacting concrete (PhD thesis), Eindhoven University of Technology, 2010.

[93]     G. Hüsken, H.J.H. Brouwers, A new mix design concept for earth-moist concrete: A theoretical and experimental study, Cem. Concr. Res. 38 (2008) 1246–1259. https://doi.org/10.1016/j.cemconres.2008.04.002.

[94]     R. Yu, P. Spiesz, H.J.H. Brouwers, Development of an eco-friendly Ultra-High Performance Concrete (UHPC) with efficient cement and mineral admixtures uses, Cem. Concr. Compos. 55 (2015) 383–394. https://doi.org/10.1016/j.cemconcomp.2014.09.024.

[95]     K. Khayat, I. Mehdipour, Design and Performance of Crack-Free Environmentally Friendly Concrete "Crack-Free Eco-Crete," No. NUTC R322 . (2014) 145.

[96]     K. Khayat, N. Libre, Roller Compacted Concrete: Field Evaluation and Mixture Optimization, NUTC R363. (2014) 118.

[97]     W. Meng, M. Valipour, K.H. Khayat, Optimization and performance of cost-effective ultra-high performance concrete, Mater. Struct. 2016 501. 50 (2016) 1–16. https://doi.org/10.1617/S11527-016-0896-3.

[98]     I. Mehdipour, K.H. Khayat, Understanding the role of particle packing characteristics in rheo-physical properties of cementitious suspensions: A literature review, Constr. Build. Mater. 161 (2018) 340–353. https://doi.org/10.1016/j.conbuildmat.2017.11.147.

[99]     I. Mehdipour, K.H. Khayat, Effect of particle-size distribution and specific surface area of different binder systems on packing density and flow characteristics of cement paste, Cem. Concr. Compos. 78 (2017) 120–131. https://doi.org/10.1016/j.cemconcomp.2017.01.005.

[100]   F. V. Mueller, O.H. Wallevik, K.H. Khayat, Linking solid particle packing of Eco-SCC to material performance, Cem. Concr. Compos. 54 (2014) 117–125. https://doi.org/10.1016/j.cemconcomp.2014.04.001.

[101]   X. Wang, K. Wang, P. Taylor, G. Morcous, Assessing particle packing based self-consolidating concrete mix design method, Constr. Build. Mater. 70 (2014) 439–452. https://doi.org/10.1016/j.conbuildmat.2014.08.002.

[102]   R. Yu, P. Spiesz, H.J.H. Brouwers, Mix design and properties assessment of Ultra-

High Performance Fibre Reinforced Concrete (UHPFRC), Cem. Concr. Res. 56 (2014) 29–39. https://doi.org/10.1016/J.CEMCONRES.2013.11.002.

[103] Q.L. Yu, P. Spiesz, H.J.H. Brouwers, Development of cement-based lightweight composites – Part 1: Mix design methodology and hardened properties, Cem. Concr. Compos. 44 (2013) 17–29. https://doi.org/10.1016/j.cemconcomp.2013.03.030.

[104] ENCI, Portland Cement, CEM I 52,5 R, Technical Advice, 's-Hertogenbosch, 2017. www.enci.nl.

[105] ENCI, Portland Cement, CEM III/B 42,5 L-LH/SR, Technical Advice, 's-Hertogenbosch, 2020. www.enci.nl.

[106] P.-C. Aitcin, High Performance Concrete, E & FN Spon, New York, 1998.

[107] BSI Committee B/517/1, BS EN 12390-3:2009 Testing hardened concrete. Compressive strength of test specimens, 2009.

[108] P.-C. Aitcin, Demystifying Autogenous Shrinkage, Concr. Int. 21 (1999) 54–56.

[109] P.-C. Aitcin, The durability characteristics of high performance concrete: a review, Cem. Concr. Compos. 25 (2003) 409–420. https://doi.org/10.1016/S0958-9465(02)00081-1.

[110] G.E.P. Box, J.S. Hunter, W.G. Hunter, Statistics for Experimenters: Design, Innovation, and Discovery, Wiley, 2005.

[111] J. Yuan, W. Lindquist, D. Darwin, J.A. Browning, Effect of Slag Cement on Drying Shrinkage of Concrete, Mater. J. 112 (2015) 267–276. https://doi.org/10.14359/51687129.

[112] J. Newman, B. Sen Choo, Advanced concrete technology, Butterworth-Heinemann, 2003.

[113] The Concrete Society, TR-22 Non-structural cracks in concrete (Fourth edition), The Concrete Society, 2010.

[114] S. Nagataki, H. Gem, H. Gomi, Expansive admixtures (mainly ettringite), Elsevier, 1998. https://doi.org/10.1016/S0958-9465(97)00064-4.

[115] Z. Bofang, Thermal Stresses and Temperature Control of Mass Concrete, Elsevier, 2014. https://doi.org/10.1016/C2012-0-06038-3.

[116] P.K. Mehta, D. Pirtz, Magnesium oxide additive for producing selfstress in mass concrete, in: 7th Int. Congr. Chem. Cem. Vo. III, Paris, France, 1980: pp. 6–9.

[117] C. Du, A Review of Magnesium Oxide in Concrete, Concr. Int. 27 (2005) 45–50.

[118] L. Mo, M. Deng, A. Wang, Effects of MgO-based expansive additive on compensating the shrinkage of cement paste under non-wet curing conditions, Cem. Concr. Compos. 34 (2012) 377–383. https://doi.org/10.1016/j.cemconcomp.2011.11.018.

[119] L. Mo, M. Deng, M. Tang, A. Al-Tabbaa, MgO expansive cement and concrete in China: Past, present and future, Cem. Concr. Res. 57 (2014) 1–12. https://doi.org/10.1016/j.cemconres.2013.12.007.

[120] C. Du, Application of MgO Concrete in RCC Dams, Concr. Int. 41 (2019) 41–48.

[121] BSI Committee B/516/12, BS EN 196-1:2016 Methods of testing cement. Determination of strength, BSI, 2016.

[122] ASTM Subcommittee: C07.05, ASTM C25 - 17 Standard Test Methods for Chemical Analysis of Limestone, Quicklime, and Hydrated Lime, West Conshohocken, 2017. https://doi.org/10.1520/C0025-17.

[123] E.A. Payzant, Other Topics, in: Princ. Appl. Powder Diffr., John Wiley & Sons, Ltd, Chichester, UK, 2009: pp. 365–380. https://doi.org/10.1002/9781444305487.ch9.

[124] J. Rouquerol, F. Rouquerol, P. Llewellyn, G. Maurin, K.S.W. Sing, Adsorption by Powders and Porous Solids: Principles, Methodology and Applications: Second Edition, 2nd Editio, Academic Press, 2013. https://doi.org/10.1016/C2010-0-66232-8.

[125] P. Webb, C. Orr, Analytical Methods in Fine Particle Technology, Norcross, GA, 1997.

[126] M. Thommes, K. Kaneko, A. V Neimark, J.P. Olivier, F. Rodriguez-Reinoso, J. Rouquerol, K.S.W. Sing, Physisorption of gases, with special reference to the evaluation of surface area and pore size distribution (IUPAC Technical Report), Pure Appl. Chem. 87 (2015) 1051–1069. https://doi.org/10.1515/pac-2014-1117.

[127] K.S.W. Sing, Reporting physisorption data for gas/solid systems, Pure Appl. Chem. 54 (1982) 2201–2218. https://doi.org/10.1351/pac198254112201.

[128] U. Franz-Josef, J.M. Hamlin, R.J.-M. Pellenq, Mechanics and Physics of Creep, Shrinkage, and Durability of Concrete, Mech. Phys. Creep, Shrinkage, Durab. Concr. (2013). https://doi.org/10.1061/9780784413111.

[129] R. Gagné, Expansive agents, in: Sci. Technol. Concr. Admixtures, 2015: pp. 441–456. https://doi.org/10.1016/B978-0-08-100693-1.00022-9.

[130] M.E. Aissi, Étude de l'influence d'un agent d'expansion interne et d'un agent réducteur de retrait sur les variations volumiques libres et restreintes d'un béton (Master thesis), Université de Sherbrooke, 2015.

[131] U.S. Geological Survey, Mineral commodity summaries 2021: U.S. Geological Survey, 2021. https://doi.org/https://doi.org/10.3133/mcs2021.

[132] Future market insights, Magnesium Oxide Market. 2021 Analysis and Review: Magnesium Oxide Market by Application – Industrial, Refractories, and Agricultural for 2021-2031, 2021. https://www.futuremarketinsights.com/reports/magnesium-oxide-market.

[133] M.A.L. Braulio, G.G. Morbioli, L.R.M. Bittencourt, V.C. Pandolfelli, Novel Features of Nanoscaled Particles Addition to Alumina-Magnesia Refractory Castables, J. Am. Ceram. Soc. 93 (2010) 2606–2610. https://doi.org/10.1111/j.1551-2916.2010.03792.x.

[134] M.A.L. Braulio, V.C. Pandolfelli, Tailoring the Microstructure of Cement-Bonded Alumina-Magnesia Refractory Castables, J. Am. Ceram. Soc. 93 (2010) 2981–2985. https://doi.org/10.1111/j.1551-2916.2010.03956.x.

[135] Y. Dai, Y. Li, X. Xu, Q. Zhu, W. Yan, S. Jin, H. Harmuth, Fracture behaviour of magnesia refractory materials in tension with the Brazilian test, J. Eur. Ceram. Soc. 39 (2019) 5433–5441. https://doi.org/10.1016/j.jeurceramsoc.2019.07.026.

[136] Y. Dai, Y. Li, S. Jin, H. Harmuth, Y. Wen, X. Xu, Mechanical and fracture investigation of magnesia refractories with acoustic emission-based method, J. Eur. Ceram. Soc. 40 (2020) 181–191. https://doi.org/10.1016/j.jeurceramsoc.2019.09.010.

[137] E.A. Elkhalifa, H.B. Friedrich, Magnesium oxide as a catalyst for the dehydrogenation of n-octane, Arab. J. Chem. 11 (2018) 1154–1159. https://doi.org/10.1016/j.arabjc.2014.10.002.

[138] E.K. Lee, K.D. Jung, O.S. Joo, Y.G. Shul, Magnesium oxide as an effective catalyst in catalytic wet oxidation of H2S to sulfur, React. Kinet. Catal. Lett. 82 (2004) 241–246. https://doi.org/10.1023/b:reac.0000034833.97966.96.

[139] N. Cooray, Knowledge accumulation and technological advance. The case of synthetic rubber, Res. Policy. 14 (1985) 83–95. https://doi.org/10.1016/0048-7333(85)90016-2.

[140] L. Zhou, S. Zhang, Z. Li, X. Liang, Z. Zhang, R. Liu, J. Yun, Efficient degradation of phenol in aqueous solution by catalytic ozonation over MgO/AC, J. Water Process Eng. 36 (2020) 101168. https://doi.org/10.1016/j.jwpe.2020.101168.

[141] X. Yao, N. Jiang, J. Li, N. Lu, K. Shang, Y. Wu, An improved corona discharge ignited by oxide cathodes with high secondary electron emission for toluene degradation, Chem. Eng. J. 362 (2019) 339–348. https://doi.org/10.1016/j.cej.2018.12.151.

[142] H.T.S. Britton, S.J. Gregg, G.W. Winsor, The calcination of dolomite. Part I.—The kinetics of the thermal decomposition of calcite and of magnesite, Trans. Faraday Soc. 48 (1952) 63–69. https://doi.org/10.1039/TF9524800063.

[143] Z.S.H. Abu-Hamatteh, M.A. Alnawafleh, Evaluation of magnesia clinker extracted from dolomite rocks, Miner. Process. Extr. Metall. Rev. 30 (2009) 269–279. https://doi.org/10.1080/08827500802665508.

[144] G. Li, Z. Li, H. Ma, X. Jiang, W. Yao, Preparation of magnesia nanoballs from dolomite, Integr. Ferroelectr. 145 (2013) 170–177. https://doi.org/10.1080/10584587.2013.789301.

[145] N.P. Bansal, Sol-Gel Synthesis of Magnesium Oxide-Silicon Dioxide Glass Compositions, J. Am. Ceram. Soc. 71 (1988) 666–672. https://doi.org/10.1111/j.1151-2916.1988.tb06386.x.

[146] N.P. Bansal, NASA TM-89905 - Sol-gel synthesis of MgO-SiO2 glass compositions having stable liquid-liquid immiscibility, Pittsburg, Pennsylvania, 1987. https://ntrs.nasa.gov/archive/nasa/casi.ntrs.nasa.gov/19870014317.pdf.

[147] W. Wang, X. Qiao, J. Chen, The Role of Acetic Acid in Magnesium Oxide Preparation via Chemical Precipitation, J. Am. Ceram. Soc. 91 (2008) 1697–1699. https://doi.org/10.1111/j.1551-2916.2008.02326.x.

[148] J. Adánez, L.F. de Diego, F. García-Labiano, Calcination of calcium acetate and calcium magnesium acetate: effect of the reacting atmosphere, Fuel. 78 (1999) 583–592. https://doi.org/10.1016/S0016-2361(98)00186-0.

[149] I.F. Mironyuk, V.M. Gun'ko, M.O. Povazhnyak, V.I. Zarko, V.M. Chelyadin, R. Leboda, J. Skubiszewska-Zięba, W. Janusz, Magnesia formed on calcination of

Mg(OH)₂ prepared from natural bischofite, Appl. Surf. Sci. 252 (2006) 4071–4082. https://doi.org/10.1016/J.APSUSC.2005.06.020.

[150] V.R. Choudhary, M.Y. Pandit, Surface properties of magnesium oxide obtained from magnesium hydroxide: Influence on preparation and calcination conditions of magnesium hydroxide, Appl. Catal. 71 (1991) 265–274. https://doi.org/10.1016/0166-9834(91)85084-9.

[151] B. Liu, P.S. Thomas, A.S. Ray, J.P. Guerbois, A TG analysis of the effect of calcination conditions on the properties of reactive magnesia, J. Therm. Anal. Calorim. 88 (2007) 145–149. https://doi.org/10.1007/s10973-006-8106-0.

[152] X. Zhang, Y. Zheng, X. Feng, X. Han, Z. Bai, Z. Zhang, Calcination temperature-dependent surface structure and physicochemical properties of magnesium oxide, RSC Adv. 5 (2015) 86102–86112. https://doi.org/10.1039/C5RA17031A.

[153] F. Demir, B. Dönmez, H. Okur, F. Sevim, Calcination Kinetic of Magnesite from Thermogravimetric Data, Chem. Eng. Res. Des. 81 (2003) 618–622. https://doi.org/10.1205/026387603322150462.

[154] A.U. Daniels, R.C. Lowrie, R.L. Gibby, I.B. Cutler, Observations on Normal Grain Growth of Magnesia and Calcia, J. Am. Ceram. Soc. 45 (1962) 282–285. https://doi.org/10.1111/j.1151-2916.1962.tb11145.x.

[155] C.O. Hulse, S.M. Copley, J.A. Pask, Effect of Crystal Orientation on Plastic Deformation of Magnesium Oxide, J. Am. Ceram. Soc. 46 (1963) 317–323. https://doi.org/10.1111/j.1151-2916.1963.tb11738.x.

[156] A. Cimino, P. Porta, M. Valigi, Dependence of the Lattice Parameter of Magnesium Oxide on Crystallite Size, J. Am. Ceram. Soc. 49 (1966) 152–156. https://doi.org/10.1111/j.1151-2916.1966.tb15394.x.

[157] S.J. Gregg, R.K. Packer, The production of active solids by thermal decomposition. Part VI. The calcination of magnesium hydroxide, J. Chem. Soc. (1955) 51–55. https://doi.org/10.1039/jr9550000051.

[158] R.S. Mikhail, S. Nashed, A.M. Khalil, Heats of immersion of pure and doped magnesia in cyclohexane. Effects of micropores, Discuss. Faraday Soc. 52 (1971) 187–195. https://doi.org/10.1039/DF9715200187.

[159] J.P. Coulomb, T.S. Sullivan, O.E. Vilches, Adsorption of Kr, Xe, and Ar on highly uniform MgO smoke, Phys. Rev. B. 30 (1984) 4753–4760. https://doi.org/10.1103/PhysRevB.30.4753.

[160] M.R. Carrott, P. Carrott, M.B. De Carvalho, K.S.W. Sing, Ex-hydroxide magnesium oxide as a model adsorbent for investigation of micropore filling mechanisms, J. Chem. Soc. Faraday Trans. 87 (1991) 185–191. https://doi.org/10.1039/FT9918700185.

[161] J. Landers, G.Y. Gor, A. V. Neimark, Density functional theory methods for characterization of porous materials, Colloids Surfaces A Physicochem. Eng. Asp. 437 (2013) 3–32. https://doi.org/10.1016/j.colsurfa.2013.01.007.

[162] S.J. Gregg, K.S.W. Sing, Adsorption, surface area and porosity, 2 ed., Academic Press, London, 1982.

[163] M.R. Bhambhani, P.A. Cutting, K.S.W. Sing, D.H. Turk, Analysis of nitrogen

adsorption isotherms on porous and nonporous silicas by the BET and $\alpha_s$ methods, J. Colloid Interface Sci. 38 (1972) 109–117. https://doi.org/10.1016/0021-9797(72)90226-3.

[164] K. Meyer, P. Klobes, Comparison between different presentations of pore size distribution in porous materials, Fresenius. J. Anal. Chem. 363 (1999) 174–178. https://doi.org/10.1007/s002160051166.

[165] J.H. de Boer, B.G. Linsen, Physical and Chemical Aspects of Adsorbents and Catalysts, Zeitschrift Für Phys. Chemie. 80 (1972) 107–107. https://doi.org/10.1524/zpch.1972.80.1_2.107.

[166] D. Nicholson, Variation of surface area during the thermal decomposition of solids, Trans. Faraday Soc. 61 (1965) 990–998. https://doi.org/10.1039/tf9656100990.

[167] Statista, Cement Industry in the US (report), (2018) 47. www.statista.com.

[168] WBCSD, The Cement Sustainability Initiative, Recycling Concrete, WBCSD, 2009. www.wbcsdcement.org.

[169] Global Market Insights, Concrete Admixture Market Share - Industry Size Forecast Report 2024, 2018. www.gminsights.com.

[170] R.K. Johnson, A. Zink-Sharp, S.H. Renneckar, W.G. Glasser, A new bio-based nanocomposite: Fibrillated TEMPO-oxidized celluloses in hydroxypropylcellulose matrix, Cellulose. 16 (2009) 227–238. https://doi.org/10.1007/s10570-008-9269-6.

[171] K.H. Khayat, N. Mikanovic, Viscosity-enhancing admixtures and the rheology of concrete, in: Underst. Rheol. Concr., 2011: pp. 209–228. https://doi.org/10.1016/B978-0-85709-028-7.50008-X.

[172] K.H. Khayat, Effects of antiwashout admixtures on properties of hardened concrete, ACI Mater. J. 93 (1996) 134–146. https://doi.org/10.14359/1412.

[173] W. Li, Z. Huang, F. Cao, Z. Sun, S.P. Shah, Effects of nano-silica and nano-limestone on flowability and mechanical properties of ultra-high-performance concrete matrix, Constr. Build. Mater. 95 (2015) 366–374. https://doi.org/10.1016/j.conbuildmat.2015.05.137.

[174] W. Li, Z. Huang, T. Zu, C. Shi, W.H. Duan, S.P. Shah, Influence of nanolimestone on the hydration, mechanical strength, and autogenous shrinkage of ultrahigh-performance concrete, J. Mater. Civ. Eng. 28 (2016) 04015068. https://doi.org/10.1061/(ASCE)MT.1943-5533.0001327.

[175] W. Li, Z. Huang, G. Hu, W. Hui Duan, S.P. Shah, Early-age shrinkage development of ultra-high-performance concrete under heat curing treatment, Constr. Build. Mater. 131 (2017) 767–774. https://doi.org/10.1016/j.conbuildmat.2016.11.024.

[176] J. Ouyang, B. Han, Y. Cao, W. Zhou, W. Li, S.P. Shah, The role and interaction of superplasticizer and emulsifier in fresh cement asphalt emulsion paste through rheology study, Constr. Build. Mater. 125 (2016) 643–653. https://doi.org/10.1016/j.conbuildmat.2016.08.085.

[177] A. Leemann, F. Winnefeld, The effect of viscosity modifying agents on mortar and concrete, Cem. Concr. Compos. 29 (2007) 341–349. https://doi.org/10.1016/j.cemconcomp.2007.01.004.

[178] O.M. Jensen, Use of superabsorbent polymers in construction materials, in: 1st Int. Conf. Microstruct. Relat. Durab. Cem. Compos. 13-15 Oct., Nanjing, China, 2008: pp. 757–764.

[179] X. Sun, Q. Wu, J. Zhang, Y. Qing, Y. Wu, S. Lee, Rheology, curing temperature and mechanical performance of oil well cement: Combined effect of cellulose nanofibers and graphene nano-platelets, Mater. Des. 114 (2017) 92–101. https://doi.org/10.1016/j.matdes.2016.10.050.

[180] M. Chen, L. Li, Y. Zheng, P. Zhao, L. Lu, X. Cheng, Rheological and mechanical properties of admixtures modified 3D printing sulphoaluminate cementitious materials, Constr. Build. Mater. 189 (2018) 601–611. https://doi.org/10.1016/j.conbuildmat.2018.09.037.

[181] Technical Committee ISO/TC 6, ISO 16065-2:2014 - Pulps -- Determination of fibre length by automated optical analysis -- Part 2: Unpolarized light method, International Organization for Standardization, 2014.

[182] D. Han, R.D. Ferron, Influence of high mixing intensity on rheology, hydration, and microstructure of fresh state cement paste, Cem. Concr. Res. 84 (2016) 95–106. https://doi.org/10.1016/j.cemconres.2016.03.004.

[183] H. Karimi, Q.L. Yu, H.J.H. Brouwers, Evaluation of a novel cellulose-based viscosity modifying admixture in rheological properties of cementitious pastes, in: V. Bílek, H. Šimonová, Z. Keršner (Eds.), 6th Int. Conf. Non-Traditional Cem. Concr. June 19–22, NOVPRESS, Brno, 2017: pp. 172–179.

[184] X. Sun, Q. Wu, S. Lee, Y. Qing, Y. Wu, Cellulose Nanofibers as a Modifier for Rheology, Curing and Mechanical Performance of Oil Well Cement, Sci. Rep. 6 (2016) 31654. https://doi.org/10.1038/srep31654.

[185] A. Yahia, K.H. Khayat, Applicability of rheological models to high-performance grouts containing supplementary cementitious materials and viscosity enhancing admixture, Mater. Struct. 36 (2003) 402–412. https://doi.org/10.1007/BF02481066.

[186] ASTM Committee C09.48, ASTM C1679-14: Standard Practice for Measuring Hydration Kinetics of Hydraulic Cementitious Mixtures Using Isothermal Calorimetry, West Conshohocken, 2014. https://doi.org/10.1520/C1679-14.

[187] ASTM Committee C09.68, ASTM C1698 - 09(2014) Standard Test Method for Autogenous Strain of Cement Paste and Mortar, West Conshohocken, 2014. https://doi.org/10.1520/C1698-09R14.

[188] ASTM, ASTM C191 - 13 Standard Test Methods for Time of Setting of Hydraulic Cement by Vicat Needle, (n.d.). https://www.astm.org/Standards/C191.htm.

[189] P. Coussot, Introduction to the rheology of complex fluids, in: Underst. Rheol. Concr., Woodhead Publishing, 2011: pp. 3–22. https://doi.org/10.1016/B978-0-85709-028-7.50001-7.

[190] K. Bilba, M.A. Arsene, A. Ouensanga, Sugar cane bagasse fibre reinforced cement composites. Part I. Influence of the botanical components of bagasse on the setting of bagasse/cement composite, Cem. Concr. Compos. 25 (2003) 91–96. https://doi.org/10.1016/S0958-9465(02)00003-3.

[191] O. Onuaguluchi, N. Banthia, Plant-based natural fibre reinforced

cement composites: A review, Cem. Concr. Compos. 68 (2016) 96–108. https://doi.org/10.1016/j.cemconcomp.2016.02.014.

[192] C. Ciobanu, I. Lazau, C. Pacurariu, Investigation regarding the effect of viscosity modifying admixtures upon the Portland cement hydration using thermal analysis, (n.d.). https://doi.org/10.1007/s10973-012-2655-1.

[193] M. Sonebi, Rheological properties of grouts with viscosity modifying agents as diutan gum and welan gum incorporating pulverised fly ash, Cem. Concr. Res. 36 (2006) 1609–1618. https://doi.org/10.1016/j.cemconres.2006.05.016.

[194] Y. Nishiyama, P. Langan, H. Chanzy, Crystal structure and hydrogen-bonding system in cellulose Iβ from synchrotron X-ray and neutron fiber diffraction, J. Am. Chem. Soc. 124 (2002) 9074–9082. https://doi.org/10.1021/JA0257319/SUPPL_FILE/JA0257319_S1.CIF.

[195] B. Abderrahim, E. Abderrahman, A. Mohamed, T. Fatima, T. Abdesselam, O. Krim, Kinetic Thermal Degradation of Cellulose, Polybutylene Succinate and a Green Composite: Comparative Study, World J. Environ. Eng. Vol. 3, 2015, Pages 95-110. 3 (2015) 95–110. https://doi.org/10.12691/WJEE-3-4-1.

[196] M. Palacios, R.J. Flatt, Working mechanism of viscosity-modifying admixtures, in: Sci. Technol. Concr. Admixtures, 2015: pp. 415–432. https://doi.org/10.1016/B978-0-08-100693-1.00020-5.

[197] M.A. Bury, B.J. Christensen, Role of innovative chemical admixtures in producing self-consolidating concrete, First North Am. Conf. Des. Use Self- Consol. Concr. (2002) 137–141.

[198] K. Yoshioka, E.I. Tazawa, K. Kawai, T. Enohata, Adsorption characteristics of superplasticizers on cement component minerals, Cem. Concr. Res. 32 (2002) 1507–1513. https://doi.org/10.1016/S0008-8846(02)00782-2.

[199] M. Cyr, M. Mouret, Rheological Characterization of Superplasticized Cement Pastes Containing Mineral Admixtures: Consequences on Self-Compacting Concrete Design, in: Proc. Seventh CANMET/ACI Int. Conf. Superplast. Other Chem. Admixtures Concr., 2003: pp. 241–256.

[200] C.Z. Li, N.Q. Feng, Y. De Li, R.J. Chen, Effects of polyethlene oxide chains on the performance of polycarboxylate-type water-reducers, Cem. Concr. Res. 35 (2005) 867–873. https://doi.org/10.1016/j.cemconres.2004.04.031.

[201] S. Hanehara, K. Yamada, Interaction between cement and chemical admixture from the point of cement hydration, absorption behaviour of admixture, and paste rheology, Cem. Concr. Res. 29 (1999) 1159–1165. https://doi.org/10.1016/S0008-8846(99)00004-6.

[202] O. Blask, D. Honert, The Electrostatic Potential of Highly Filled Cement Suspension Containing Various Superplasticizers, in: Seventh CANMET/ACI Int. Symp. Superplast. Other Chem. Admixtures Concr. Malhotra, V.M, 2003: pp. 87–101. https://doi.org/10.14359/12907.

[203] A. Yahia, S. Mantellato, R.J. Flatt, Concrete rheology, in: Sci. Technol. Concr. Admixtures, Elsevier, 2016: pp. 97–127. https://doi.org/10.1016/B978-0-08-100693-1.00007-2.

[204] A. Yahia, K.. Khayat, Analytical models for estimating yield stress of high-performance pseudoplastic grout, Cem. Concr. Res. 31 (2001) 731–738. https://doi.org/10.1016/S0008-8846(01)00476-8.

[205] K.H. Khayat, A. Yahia, Effect of Welan Gum-High-Range Water Reducer Combinations on Rheology of Cement Grout, ACI Mater. J. 94 (1997) 365–372. https://doi.org/10.14359/321.

[206] H. Okamura, M. Ouchi, Self-Compacting Concrete, J. Adv. Concr. Technol. 1 (2003) 5–15.

[207] I. Mehdipour, Characterization and performance of eco and crack-free high-performance concrete for sustainable infrastructure (Doctoral dissertation), Missouri University of Science and Technology, 2017.

[208] O.A. Hisseine, N. Basic, A.F. Omran, A. Tagnit-Hamou, Feasibility of using cellulose filaments as a viscosity modifying agent in self-consolidating concrete, Cem. Concr. Compos. 94 (2018) 327–340. https://doi.org/10.1016/j.cemconcomp.2018.09.009.

[209] The Council of the European Union, Directive 1999/31/EC, of 26 April 1999 on the landfill of waste., 1999.

[210] K.S. Kim, H.S. Cho, Pilot trial on separation conditions for diaper recycling, Waste Manag. 67 (2017) 11–19. https://doi.org/10.1016/j.wasman.2017.04.027.

[211] M. Torrijos, P. Sousbie, M. Rouez, M. Lemunier, Y. Lessard, L. Galtier, A. Simao, J.P. Steyer, Treatment of the biodegradable fraction of used disposable diapers by co-digestion with waste activated sludge, Waste Manag. 34 (2014) 669–675. https://doi.org/10.1016/j.wasman.2013.11.009.

[212] M.E. Conway, F. Jooste, M.D. Smith, Treatment of absorbent sanitary paper products, USOO5558745A, 1996. https://doi.org/10.1016/S0959-6526(97)82420-1.

[213] J.-A. Cox, A. Druckman, D. Jesson, M. Mulheron, M. Smyth, H. Trew, Municipal solid waste as a resource: part 2 – case study in sustainable management, Proc. Inst. Civ. Eng. - Waste Resour. Manag. 168 (2015) 115–130. https://doi.org/10.1680/warm.14.00012.

[214] F. Girotto, Y. Matsufuji, A. Tanaka, Removal of ammonia using Ca-P (calcium polymer) from wastewaters produced in the recycling of disposable diapers, J. Mater. Cycles Waste Manag. 19 (2017) 570–576. https://doi.org/10.1007/s10163-015-0420-9.

[215] O. Maamari, L. Mouaffak, R. Kamel, C. Brandam, R. Lteif, D. Salameh, Comparison of steam sterilization conditions efficiency in the treatment of Infectious Health Care Waste, Waste Manag. 49 (2016) 462–468. https://doi.org/10.1016/j.wasman.2016.01.014.

[216] J.D. Cook, K.A. Strauss, Y.H. Caplan, C.P. LoDico, D.M. Bush, Urine pH: The effects of time and temperature after collection, J. Anal. Toxicol. 31 (2007) 486–496. https://doi.org/10.1093/jat/31.8.486.

[217] R.M. Espinosa, I. Delfin-Alcalá, S. Turpin, J.L. Contreras, Kinetic Study of Batch Biodegradation of Diapers, Int. J. Chem. React. Eng. 1 (2003). https://doi.org/10.2202/1542-6580.1082.

[218] C.P. Gerba, M.S. Huber, J. Naranjo, J.B. Rose, S. Bradford, Occurrence of enteric

pathogens in composted domestic solid waste containing disposable diapers, Waste Manag. Res. 13 (1995) 315–324. https://doi.org/10.1016/S0734-242X(95)90081-0.

[219] R. Stegmann, S. Lotter, L. King, W.D. Hopping, Fate of an absorbent gelling material for hygiene paper products in landfill and composting, Waste Manag. Res. 11 (1993) 155–170. https://doi.org/10.1177/0734242X9301100207.

[220] J. Colón, L. Ruggieri, A. Sánchez, A. González, I. Puig, Possibilities of composting disposable diapers with municipal solid wastes, Waste Manag. Res. 29 (2011) 249–259. https://doi.org/10.1177/0734242X10364684.

[221] J. Colón, M. Mestre-Montserrat, I. Puig-Ventosa, A. Sánchez, Performance of compostable baby used diapers in the composting process with the organic fraction of municipal solid waste, Waste Manag. 33 (2013) 1097–1103. https://doi.org/10.1016/j.wasman.2013.01.018.

[222] V.M. Pathak, Navneet, Review on the current status of polymer degradation: a microbial approach, Bioresour. Bioprocess. 4 (2017) 15. https://doi.org/10.1186/s40643-017-0145-9.

[223] A.A. Shah, F. Hasan, A. Hameed, S. Ahmed, Biological degradation of plastics: A comprehensive review, Biotechnol. Adv. 26 (2008) 246–265. https://doi.org/10.1016/j.biotechadv.2007.12.005.

[224] N. Lucas, C. Bienaime, C. Belloy, M. Queneudec, F. Silvestre, J.-E. Nava-Saucedo, Polymer biodegradation: Mechanisms and estimation techniques – A review, Chemosphere. 73 (2008) 429–442. https://doi.org/10.1016/j.chemosphere.2008.06.064.

[225] C. Sánchez, Lignocellulosic residues: Biodegradation and bioconversion by fungi, Biotechnol. Adv. 27 (2009) 185–194. https://doi.org/10.1016/j.biotechadv.2008.11.001.

[226] S.J.A. van Kuijk, A.S.M. Sonnenberg, J.J.P. Baars, W.H. Hendriks, J.W. Cone, Fungal treated lignocellulosic biomass as ruminant feed ingredient: A review, Biotechnol. Adv. 33 (2015) 191–202. https://doi.org/10.1016/j.biotechadv.2014.10.014.

[227] R.C.G. Corrêa, T. Brugnari, A. Bracht, R.M. Peralta, I.C.F.R. Ferreira, Biotechnological, nutritional and therapeutic uses of Pleurotus spp. (Oyster mushroom) related with its chemical composition: A review on the past decade findings, Trends Food Sci. Technol. 50 (2016) 103–117. https://doi.org/10.1016/j.tifs.2016.01.012.

[228] S.C. Khoo, X.Y. Phang, C.M. Ng, K.L. Lim, S.S. Lam, N.L. Ma, Recent technologies for treatment and recycling of used disposable baby diapers, Process Saf. Environ. Prot. 123 (2019) 116–129. https://doi.org/10.1016/j.psep.2018.12.016.

[229] P.C. Aïtcin, Water and its role on concrete performance, in: Sci. Technol. Concr. Admixtures, 2015: pp. 75–86. https://doi.org/10.1016/B978-0-08-100693-1.00005-9.

[230] A. Behnood, K. Van Tittelboom, N. De Belie, Methods for measuring pH in concrete: A review, Constr. Build. Mater. 105 (2016) 176–188. https://doi.org/10.1016/j.conbuildmat.2015.12.032.

[231] J. Farrell, J. Smith, S. Hathaway, R. Dean, Lime Stabilization of Primary Sludges,

Water Pollut. Control Fed. 46 (1974) 113–122.

[232] O.C. Pancorbo, G. Bitton, S.R. Farrah, G.E. Gifford, A.R. Overman, Poliovirus Retention in Soil Columns after Application of Chemical-and Polyelectrolyte-Conditioned Dewatered Sludges, Appl. Environ. Microbiol. 54 (1988) 118–123.

[233] L. Eriksen, P. Andreasen, B. Ilsøe, Inactivation of Ascaris suum eggs during storage in lime treated sewage sludge, Water Res. 30 (1996) 1026–1029. https://doi.org/10.1016/0043-1354(95)00258-8.

[234] D.G. Randall, M. Krähenbühl, I. Köpping, T.A. Larsen, K.M. Udert, A novel approach for stabilizing fresh urine by calcium hydroxide addition, Water Res. 95 (2016) 361–369. https://doi.org/10.1016/j.watres.2016.03.007.

[235] C. Li, L. Miao, Q. You, S. Hu, H. Fang, Effects of viscosity modifying admixture (VMA) on workability and compressive strength of structural EPS concrete, Constr. Build. Mater. 175 (2018) 342–350. https://doi.org/10.1016/j.conbuildmat.2018.04.176.

[236] D.F. Putnam, NASA CR-1802 Composition and concentrative properties of human urine, 1971.

[237] H.Y. Kim, Urea additives for reduction of hydration heat in cement composites, Constr. Build. Mater. 156 (2017) 790–798. https://doi.org/10.1016/j.conbuildmat.2017.09.042.

[238] E. Poulsen, L. Mejlbro, Diffusion of chloride in concrete: theory and application, Taylor & Francis, 2006.

[239] BSI Committee B/517/1, BS EN 1008:2002 Mixing water for concrete: Specification for sampling, testing and assessing the suitability of water, including water recovered from processes in the concrete industry, as mixing water for concrete., BSI, 2002.

[240] ASTM Subcommittee C09.40, ASTM C1602 / C1602M - 12 Standard Specification for Mixing Water Used in the Production of Hydraulic Cement Concrete, West Conshohocken, 2012. https://doi.org/10.1520/C1602_C1602M-12.

[241] ACI Committee 201, 201.2R-16 Guide to durable concrete, American Concrete Institute, Farmington Hills, 2017.

[242] J. Skalny, J. (Jacques) Marchand, I. Odler, Sulfate attack on concrete, Spon Press, London, 2002.

[243] H.F.W. Taylor, Cement chemistry, 2nd ed., Thomas Telford Publishing, London, 1997.

[244] EDANA (European disposables and nonwovens association), NWSP 240.0.R2 (15) Polyacrylate Superabsorbent Powders- Free Swell Capacity in Saline by Gravimetric Determination, European Disposable and Nonwovens Association, 2015.

[245] EDANA (European disposables and nonwovens association), NWSP 241.0.R2 (15) Polyacrylate Superabsorbent Powders- Gravimetric Determination of Fluid Retention Capacity in Saline Solution After Centrifugation, European Disposable and Nonwovens Association, 2015.

[246] EDANA (European disposables and nonwovens association), NWSP 242.0.R2 (15) Polyacrylate Superabsorbent Powders- Gravimetric Determination of Absorption

Against Pressure, European Disposable and Nonwovens Association, 2015.

[247] Technical Committee ISO/TC 173/SC 3, ISO 17190-5:2001 - Urine-absorbing aids for incontinence -- Test methods for characterizing polymer-based absorbent materials -- Part 5: Gravimetric determination of free swell capacity in saline solution, International Organization for Standardization, 2001.

[248] Technical Committee ISO/TC 173/SC 3, ISO 17190-6:2001 - Urine-absorbing aids for incontinence -- Test methods for characterizing polymer-based absorbent materials -- Part 6: Gravimetric determination of fluid retention capacity in saline solution after centrifugation, International Organization for Standardization, 2001.

[249] Technical Committee ISO/TC 173/SC 3, ISO 17190-7:2001 Urine-absorbing aids for incontinence — Test methods for characterizing polymer-based absorbent materials — Part 7: Gravimetric determination of absorption under pressure, International Organization for Standardization, 2001.

[250] ENCI, Portland Cement, CEM III/A 52,5 N, Technical Advice, 's-Hertogenbosch, 2006. www.enci.nl.

[251] EDANA (European disposables and nonwovens association), Sustainability Report 2007-2008; Absorbent Hygiene Products, Brussels, 2008. www.edana.org.

[252] P.F.G. Banfill, Rheology of Fresh Cement and Concrete, Rheol. Rev. (1991) 61–130. https://doi.org/10.4324/9780203473290.

[253] P.F.G. Banfill, The rheology of fresh mortar, Mag. Concr. Res. 42 (1990) 213–221. https://doi.org/10.1680/macr.1991.43.154.13.

[254] D. Chopin, F. De Larrard, B. Cazacliu, Why do HPC and SCC require a longer mixing time?, Cem. Concr. Res. 34 (2004) 2237–2243. https://doi.org/10.1016/j.cemconres.2004.02.012.

[255] J. Ouyang, B. Han, Y. Cao, W. Zhou, W. Li, S.P. Shah, The role and interaction of superplasticizer and emulsifier in fresh cement asphalt emulsion paste through rheology study, Constr. Build. Mater. 125 (2016) 643–653. https://doi.org/10.1016/j.conbuildmat.2016.08.085.

[256] BSI Committee B/517/1, BS EN 12350-8:2010 Testing fresh concrete. Self-compacting concrete. Slump-flow test, BSI, 2010.

[257] BSI Committee B/517/1, BS EN 12350-9:2010 Testing fresh concrete. Self-compacting concrete. V-funnel test, BSI, 2010.

[258] The State Secretary for Housing Planning and the Environment, The Soil Quality Decree (Dutch Standards), 2007. https://rwsenvironment.eu/publish/pages/126568/soilqualitydecree_24_275037.pdf.

[259] P. Lura, F. Durand, A. Loukili, K. Kovler, O.M. Jensen, Compressive Strength of Cement Pastes and Mortars With Superabsorbent Polymers, in: Int. RILEM Conf. Vol. Chang. Hardening Concr. Test. Mitig., Lyngby, Denmark, 2006.

[260] S. Riyazi, J.T. Kevern, M. Mulheron, Super absorbent polymers (SAPs) as physical air entrainment in cement mortars, Constr. Build. Mater. 147 (2017) 669–676. https://doi.org/10.1016/j.conbuildmat.2017.05.001.

[261] S. Laustsen, M.T. Hasholt, O.M. Jensen, Void structure of concrete with superabsorbent polymers and its relation to frost resistance of concrete, Mater. Struct. Constr. 48 (2015) 357–368. https://doi.org/10.1617/s11527-013-0188-0.

[262] EFNARC, The European Guidelines for Self-Compacting Concrete; Specification, Production and Use, The European Federation of Specialist Construction Chemicals and Concrete Systems., 2005. www.efnarc.org.

[263] ACI Committee 238, 238.1R-08 Report on Measurements of Workability and Rheology of Fresh Concrete, American Concrete Institute, Farmington Hills, 2007.

[264] A. Assmann, Physical properties of concrete modified with superabsorbent polymers (PhD thesis), University of Stuttgart, 2013.

[265] D.B. Braun, M.R. Rosen, Rheology Modifiers Handbook: Practical Use and Application, William Andrew Pub, 2000. https://doi.org/10.1017/S0017383509990313.

[266] X. Sun, X. Zhao, B. Zhu, G. Zhang, A Review on the Management of Municipal Solid Waste Fly Ash in American, Procedia Environ. Sci. 31 (2016) 535–540. https://doi.org/10.1016/j.proenv.2016.02.079.

[267] E. Aprianti S, A huge number of artificial waste material can be supplementary cementitious material (SCM) for concrete production – a review part II, J. Clean. Prod. 142 (2017) 4178–4194. https://doi.org/10.1016/j.jclepro.2015.12.115.

[268] L.M. Federico, S.E. Chidiac, Waste glass as a supplementary cementitious material in concrete – Critical review of treatment methods, Cem. Concr. Compos. 31 (2009) 606–610. https://doi.org/10.1016/j.cemconcomp.2009.02.001.

[269] S. De Carvalho Gomes, J.L. Zhou, W. Li, G. Long, Progress in manufacture and properties of construction materials incorporating water treatment sludge: A review, Resour. Conserv. Recycl. 145 (2019) 148–159. https://doi.org/10.1016/j.resconrec.2019.02.032.

[270] N. Saikia, J. de Brito, Use of plastic waste as aggregate in cement mortar and concrete preparation: A review, Constr. Build. Mater. 34 (2012) 385–401. https://doi.org/10.1016/j.conbuildmat.2012.02.066.

[271] A. Rana, P. Kalla, H.K. Verma, J.K. Mohnot, Recycling of dimensional stone waste in concrete: A review, J. Clean. Prod. 135 (2016) 312–331. https://doi.org/10.1016/j.jclepro.2016.06.126.

[272] I.N. Grubeša, I. Barišić, A. Fucic, S.S. Bansode, Characteristics and uses of steel slag in building construction, Woodhead Publishing, 2016. https://doi.org/https://doi.org/10.1016/C2014-0-03994-9.

[273] L. De Meyst, E. Mannekens, M. Araújo, D. Snoeck, K. Van Tittelboom, S. Van Vlierberghe, N. De Belie, Parameter Study of Superabsorbent Polymers (SAPs) for Use in Durable Concrete Structures, Mater. 2019, Vol. 12, Page 1541. 12 (2019) 1541. https://doi.org/10.3390/MA12091541.

[274] EDANA (European disposables and nonwovens association), Sustainability Report, 4th ed., Brussels, 2015. www.edana.org.

[275] Y. Asako, T. Otaka, Y. Yamaguchi, Fire resistance characteristics of materials with polymer gels which absorb aqueous solution of calcium chloride, Numer. Heat

Transf. Part A Appl. 45 (2004) 49–66. https://doi.org/10.1080/1040778049026738.

# List of Nomenclatures

| | | |
|---|---|---|
| $a$ | hazardous chemical content per diaper, [µg/g] | Chapter 6 |
| $a_{\propto S}$ | calculated surface area of the test material from the $\alpha_S$ curve, [m²] | Chapter 4 |
| $a_{BET}^{ref}$ | BET surface area of the standard data, [m²] | Chapter 4 |
| $a_{BET}$ | BET surface area, [m²] | Chapters 3 & 4 |
| $A$ | area of the Lorentz peak function | Chapter 4 |
| $A_{Fraction\ i}^{cumulative}$ | area of the ith Lorentz fit in the cumulative fit | Chapter 4 |
| $A_{Fraction\ i}^{pure}$ | area of the ith Lorentz fit in its pure form | Chapter 4 |
| $c$ | curvature parameter of the modified Bingham model, [Pa·s²] | Chapter 5 |
| $C$ | BET constant | Chapter 4 |
| $C(w)$ | cumulative mesopore size distribution, [cm³·g⁻¹] | Chapter 4 |
| $d$ | particle size, [µm] | Chapter 2 |
| $d_{max}$ | the maximum particle size, [µm] | Chapter 2 |
| $d_{min}$ | the minimum particle size, [µm] | Chapter 2 |
| $F(d_j)$ | Cumulative volume of interstitial particle fractions | Chapter 2 |
| $G$ | yield parameter [N·mm] | Chapter 6 |
| $h$ | the concentration of a hazardous chemical in combined mixing water of a cement composite in the wake of incorporating shredded waste diapers [ppm in water] | Chapter 6 |
| $H$ | plastic viscosity parameter, [N·mm·s] | Chapter 6 |
| $I(w)$ | the incremental mesopore size distribution, [cm³·g⁻¹] | Chapter 4 |
| $K$ | consistency factor of the Herschel-Bulkley model | Chapter 5 |

| | | |
|---|---|---|
| $L$ | Avogadro constant | Chapter 4 |
| $L(w)$ | weighted mesopore probability distribution | Chapter 4 |
| $m^s$ | mass of adsorbing solid sample, [g] | Chapters 3 & 4 |
| $n$ | flow index of the Herschel-Bulkley model | Chapter 5 |
| $N$ | speed of rotation [rps] | Chapter 6 |
| $N_{exp}\left(\dfrac{p}{p^0}\right)$ | measured number of adsorbed molecules | Chapter 4 |
| $N_{theo}$ | kernel of theoretical isotherms in model pores | Chapter 4 |
| $p$ | actual adsorbing gas pressure, [mmHg] | Chapters 3 & 4 |
| $p^0$ | the saturation pressure of the adsorbing gas, [mmHg] | Chapters 3 & 4 |
| $P(d)$ | the cumulative fraction of the total solids being smaller than size $d$, [µm] | |
| $P(w)$ | mesopore probability distribution (probability density function), [nm$^{-1}$] | Chapter 4 |
| $q$ | distribution modulus | Chapter 2 |
| $Q$ | the concentration of a hazardous chemical in urine [mg/l] | Chapter 6 |
| $r_K$ | Kelvin radius, [nm] | Chapter 3 |
| $R$ | gas constant, [JK$^{-1}$mol$^{-1}$] | Chapter 3 |
| $s_{ref}$ | slope of the $\alpha_s$ plot of the standard data | Chapter 4 |
| $s_{test}$ | slope of the $\alpha_s$ plot of the test material | Chapter 4 |
| $t$ | thickness of multimolecular layer [nm] (Chapter 4) | Chapter 3 |
| $T$ | torque measured on the viscometer [N·m] | Chapter 6 |
| $v^l$ | molar volume of the liquid (i.e. the condensed adsorptive) | Chapter 3 |
| $V^a$ | amount of adsorbate (cm³/g STP) | Chapters 3 & 4 |
| $V_{ref}^a$ | amount of adsorbate in the standard data | Chapter 4 |
| $V_{ref}^{0.4}$ | amount of adsorbate at the pre-selected relative pressure of 0.4 in the standard data | Chapter 4 |
| $V_0$ | gas molar volume (22414 cm³) | Chapter 4 |

# List of Abbreviations

| | |
|---|---|
| ACI | American Concrete Institute |
| ASTM | American Society for Testing and Materials |
| BET | Brunauer–Emmett–Teller |
| BFS | Blast Furnace Slag |
| BJH | Barrett-Joyner-Halenda |
| BM | Bingham Model |
| CEN | the European Committee for Standardization |
| CF | Cellulose Fiber |
| CMF | Cellulose Microfiber |
| CNF | Cellulose Nanofiber |
| CVC | Conventional Vibrated Concrete |
| ESEM | Environmental Scanning Electron Microscopy |
| FC | Flowing Concrete |
| FWHM | Full Width at Half Maximum |
| HB | Herschel-Bulkley |
| HBM | Herschel-Bulkley Model |
| HPP | High-energy milled Paper Pulp |
| LPP | Low-energy milled Paper Pulp |
| IUPAC | International Union of Pure and Applied Chemistry |
| LBM | Light-burnt Magnesia |
| LOI | Loss on Ignition |
| MB | Modified Bingham |
| MBM | Modified Bingham Model |
| MM | MasterMatrix DSC 100 |

| MVD | Minimum VMA Demand (to stop flow) |
| MWD | Minimum Water Demand (to initiate flow) |
| NLDFT | Nonlocal Density Functional Theory |
| OPC | Ordinary Portland Cement |
| PCE | Polycarboxylic Ether |
| PDF | Probability Density Function |
| PP | Paper Pulp |
| PSD | Particle Size Distribution |
| PVA | Polyvinyl Alcohol |
| REF | Reference |
| RVD | Relative VMA Demand (to decrease fluidity) |
| RWD | Relative Water Demand (to increase fluidity) |
| SCA | Shrinkage Compensating Admixture |
| SCC | Self-Consolidating Concrete |
| SP | Superplasticizer |
| SWD | Shredded Waste Diaper |
| VMA | Viscosity Modifying Admixture |
| UHPC | Ultra-High-Performance Concrete |
| XRF | X-Ray Fluorescence |
| XRD | X-Ray Diffraction |

# List of Publications

**Peer-Reviewed Journal Publications**

1.  Khaloo, A.R., Karimi, H., Asadollahi, S., & Dehestani, M. (2017). A New Mixture Design Method for Ultra-High-Strength Concrete. ACI Materials Journal, 114, 215-224.

2.  Karimi, H., Yu, Q.L., Brouwers, & H.J.H. (2020). Valorization of waste baby diapers in concrete. Resources, Conservation and Recycling, 153, 104548.

3.  Karimi, H., Gauvin, F., Brouwers, H.J.H., Cardinaels, R., & Yu, Q.L. (2020). On the versatility of paper pulp as a viscosity modifying admixture for cement composites. Construction and Building Materials, 265, 120660.

4.  Karimi, H., & Brouwers, H.J.H. (2021). Mixture design method for pumpable low shrinkage flowing concrete: A particle packing approach. *Submitted.*

5.  Karimi, H., & Brouwers, H.J.H. (2021). Rapidly expansive magnesia in mortar and concrete: the role of magnesia structure and curing conditions. *Submitted.*

6.  Karimi, H., & Brouwers, H.J.H. (2021). Accelerated thermal history analysis of light burnt magnesium oxide by surface properties. *Submitted.*

7.  Karimi, H., Schollbach, K., van der Laan, S., & Brouwers, H.J.H. (2021). Composition of highly amorphous blended cements: Quantitative determination by a combination of SEM and EDS. *Submitted.*

**Conference Proceedings**

1.  Karimi, H., Yu, Q.L., & Brouwers, H.J.H. Evaluation of a novel cellulose-based viscosity modifying admixture in rheological properties of cementitious pastes, The 6th International Conference of Non-Traditional Cement and Concrete, 19-22 July 2017, Brno, Czech Republic.

2.  Karimi, H., Yu, Q.L., & Brouwers, H.J.H. Evaluation of a novel cellulose-based viscosity modifying admixture in rheological properties of cementitious pastes. The 9th International Symposium of Cement and Concrete, 31 October- 3 November 2017, Wuhan, China.

3.  Karimi, H., Yu, Q.L., & Brouwers, H.J.H. On the effect of the physical structure of cement on shrinkage of cementitious materials, 5th International Conference on

Concrete Repair, Rehabilitation, and Retrofitting (ICCRRR 2018), 19 November- 21 November 2018, Cape Town, South Africa.

**Patents**

1. Karimi, H., Yu, Q.L., & Brouwers, H.J.H. (2020). Magnesia Powder. NL 83087 29/09/2020.

2. Khaloo A.R., & Karimi, H. (2009). Active Thermal Control of Ultra-High Strength Mass Concrete. I.R.I. Patent No. 56856. 20/01/2009.

3. Khaloo A.R., & Karimi, H. (2009). Grout-Based Microsilica Structural Concrete Mixture Design. I.R.I. Patent No. 56848. 27/01/2009.

# Curriculum Vitae

Hossein Karimi was born in Tehran, Iran. His educational background includes a BSc in Civil Engineering and an MSc in Structural Engineering. During his master's studies at Sharif University of Technology (SUT), he worked on ultra-high strength concretes and registered two patents. His master thesis was rewarded with the best thesis award. He was also selected as an Elite National Talent (Top Inventor) by National Elites Foundation, the only honor society in Iran. Then, he started working as a project engineer and was promoted to senior project manager in massive projects such as Azad University's multilevel parking and bus station project in Tehran, Iran. In 2016, he joined the Building Materials research group at Eindhoven University of Technology (TU/e), Eindhoven, Netherlands. In 2017, he started a Ph.D. project in the same group under the supervision of prof.dr.ir. H.J.H. Brouwers and dr. Q.L. Yu, of which the results are presented in this dissertation.

Inferior viscosity and volume change deteriorate concrete and reduce durability. This dissertation aims to tackle these shortcomings by implementing two sustainable strategies. The first strategy is using a mix design method to enhance pumpability and reduce shrinkage. The second strategy is to develop concrete admixtures. Where possible, the link between the first and second strategy is made, and a hybrid strategy comprising an optimum mix design method and a concrete admixture is introduced.

The first strategy is discussed in Chapter 2. It investigates the relationship between the modified A&A concrete mix design model and the pumpability and shrinkage of flowing concrete. The outcome of this modified model is compared to ACI 211.9R-18 recommendations and the technical literature.

The second strategy is discussed in chapters three to six. It starts with reporting the characteristics of the rapidly expansive light-burnt magnesia (Chapter 3). Next, the surface science is used to introduce an accelerated technique for assessing the thermal history of this type of magnesia (Chapter 4). Then, the performance of paper pulp as an innovative viscosity modifying admixture for cement composites is evaluated (Chapter 5). Finally, an innovative mindset towards recycled superabsorbent polymers is introduced (Chapter 6). In this setting, shredded waste baby diapers are used to modify the viscosity of concrete.

DEPARTMENT OF THE BUILT ENVIRONMENT

**TU/e**

**EINDHOVEN UNIVERSITY OF TECHNOLOGY**